A Novel Methodology for Simulating Contact-Line Behavior in Capillary-Driven Flows

Thesis by

Gerry Della Rocca

In Partial Fulfillment of the Requirements

for the Degree of

Doctor of Philosophy

California Institute of Technology

Pasadena, California

2014

(Defended May 20, 2014)

For my parents.

Acknowledgments

An investment in knowledge pays the best interest.

— Benjamin Franklin

I would first like to thank my doctorate advisers. My official adviser, Professor G. Blanquart, had a critical guiding role in this work despite (or perhaps because of) all our friction and email storms. I really grew as an individual and as a researcher working with him. While most people are limited to a single adviser, I had the privilege of two additional unofficial advisers. I worked with Professor S. M. Troian for approximately a year in the middle of my doctorate and while none of that research appears in the present work, my experience with her was invaluable. It may have arguably been *the* turning point in my graduate school career. Professor T. Colonius has been a great counselor; I could always count on blunt, honest, and fair criticism even if I didn't want to hear it.

Graduate school is undoubtedly a stressful experience and I wouldn't have made it through without many people, too many to name. First year at Caltech was mentally and emotionally taxing; I am indebted to the classmates with whom I went through it. In later years, my lab mates (Sid, Jason, Phares, Yuan) and pseudo-lab mates (Vedran, Jomela) were always willing to empathize, give feedback, and share a laugh. Finally, I have been very fortunate to have had an awesome group of friends, e.g., Tom / Caroline / Dex / Max / Archie, Nick / Andreas, Jay / Anu, Ding / Bilin, Francesco, Alex, Nick, Dylan. I would like to single out Tom and Serena (Tomerena) who were the first people I met at Caltech and were steady, insistent proponents of a work-life balance.

My elder brother, Joe, has had a dynamic impact on my life. I cannot claim to have been a good younger brother; I certainly didn't look up to him growing up and saying a loathed him wouldn't be far from the truth. I pushed myself to beat him in every way. This competition created the person I am today. Surprisingly, I realized a few years ago that, regardless of our differences, I'm really proud to call him my brother. These are words I never thought I'd write.

Lastly, I could not have gotten where I am without my parents. My parents (Vin and Pam) have always emphasized education's importance. I learned at an early age that, while they would never buy me video games, they would buy me any book I wanted. Additionally, they sacrificed much to get me through an expensive high school and college. I hope I can be worthy of this exceptional investment and support.

This material is based upon work supported by the National Science Foundation Graduate Research Fellowship under Grant No. DGE-1144469.

Abstract

Despite the wide swath of applications where multiphase fluid contact lines exist, there is still no consensus on an accurate and general simulation methodology. Most prior numerical work has imposed one of the many dynamic contact-angle theories at solid walls. Such approaches are inherently limited by the theory accuracy. In fact, when inertial effects are important, the contact angle may be history dependent and, thus, any single mathematical function is inappropriate. Given these limitations, the present work has two primary goals: 1) create a numerical framework that allows the contact angle to evolve naturally with appropriate contact-line physics and 2) develop equations and numerical methods such that contact-line simulations may be performed on coarse computational meshes.

Fluid flows affected by contact lines are dominated by capillary stresses and require accurate curvature calculations. The level set method was chosen to track the fluid interfaces because it is easy to calculate interface curvature accurately. Unfortunately, the level set reinitialization suffers from an ill-posed mathematical problem at contact lines: a "blind spot" exists. Standard techniques to handle this deficiency are shown to introduce parasitic velocity currents that artificially deform freely floating (non-prescribed) contact angles. As an alternative, a new relaxation equation reinitialization is proposed to remove these spurious velocity currents and its concept is further explored with level-set extension velocities.

To capture contact-line physics, two classical boundary conditions, the Navier-slip velocity boundary condition and a fixed contact angle, are implemented in direct numerical simulations (DNS). DNS are found to converge only if the slip length λ is well resolved by the computational mesh. Unfortunately, since λ is often very small compared to fluid structures, these simulations are not computationally feasible for large systems. To address the second goal, a new methodology is proposed which relies on the volumetric-filtered Navier-Stokes equations. Two unclosed terms, an average curvature $\bar{\kappa}$ and a viscous shear VS, are proposed to represent the missing microscale physics on a coarse mesh.

All of these components are then combined into a single framework and tested for a water droplet impacting a partially-wetting substrate. Very good agreement is found for the evolution of the contact diameter in time between the experimental measurements and the numerical simulation. Such comparison would not be possible with prior methods, since the Reynolds number Re and capillary number Ca are large. Furthermore, the experimentally approximated slip length ratio ϵ is well outside of the range currently achievable by DNS. This framework is a promising first step towards simulating complex physics in capillary-dominated flows at a reasonable computational expense.

Contents

List of Figures

List of Tables

Nomenclature

AMG Algebraic multigrid.

AMR Adaptive mesh refinement.

BiCGStab Bi-conjugate gradient-stabilized.

CFL Courant-Friedrichs-Lewy number. This value specifies whether a numerical discretization is stable for a given grid spacing Δx and time step Δt.

CSF Continuum surface force.

DNS Direct numerical simulation. In this type of simulation, node grid-spacing is smaller than all relevant length scales.

FMM Fast Marching Method.

GFM Ghost fluid method.

HCR2 Modified reinitialization routine proposed by Hartmann et al. [59].

LHS Left hand side of the equation.

LSQ A least-square polynomial fit to the local level set field to approximate derivatives, interface normals, and curvature.

MAC Marker-and-cell.

MD Molecular dynamics.

NGA Next Generation ARTS [33].

QUICK Quadratic upstream interpolation for convective kinematics [86]. This numerical scheme is an Eulerian approach to the advection equation.

SMG Streaming multigrid.

VOF Volume of fluid.

VS Viscous shear term (Eq. 5.7).

WENO Weighted essentially non-oscillatory.

YVHH Short-hand notation for Yokoi et al. [166].

$A(\theta)$ Leading coefficient in the power-law approximation for shear factors F and G.

$B(\theta)$ Exponent in the power-law approximation for shear factors F and G.

Ba Signed band number.

Bo Bond number $= \Delta\rho g H^2/\sigma$ for an appropriate length scale H.

$\mathbf{Bo}_W$ Bond number using length scale W.

C Color function in the VOF and phase-field methods.

Ca Capillary number $= \mu U/\sigma$ for an appropriate velocity U.

D Droplet diameter.

D_C Droplet contact (splat) diameter during the droplet impact and spreading process.

D_{extrap} Extrapolated value of the distance function into a wall.

D_{ghost} Approximate distance function calculated from a ghost interface.

D_ω Tangential derivative along a wall.

E_D Maximum spurious velocity magnitude throughout the entire domain.

E_p Integrated error for the interface profile given by Eq. 3.1.

E_W Maximum spurious velocity magnitude along the solid wall.

F In Chap. 2, the forcing function for the HCR2 scheme (Eq. 2.22). In Chap. 5 and 6, the integral of f expressed by Eq. 5.21.

F_{Young} Unbalanced Young's force (Eq. 1.2).

G Integral of g expressed by Eq. 5.22.

H Height of a computational domain in the y-direction.

I Identity matrix.

L Computational domain length in the x-direction.

L_M Large length scale.

La Laplace number $= \sigma\rho H/\mu^2$ for an appropriate length scale H.

$M(C)$ Mobility parameter in the phase-field method.

N A positive integer.

Oh Ohnesorge number $= \mu/\sqrt{\rho\sigma H}$ for an appropriate length scale H.

R Geometric radius of a circular interface.

Re Reynolds number $= \rho U H/\mu$ for an appropriate length scale H and velocity U.

S Box filter surface.

T Absolute fluid temperature.

U Constant advection speed used in the wedge and circular arc test cases.

U_{CL} Contact line velocity. In Sec. 5.3, it is also the mean inlet velocity.

U_i Initial droplet velocity.

W Width of the 3D Cartesian domain in Chap. 3. In Chap. 4, it is the droplet contact width.

We Weber number= $\rho U^2 H/\sigma$ for an appropriate length scale H and velocity U.

X_S Starting location of initial condition in Chap. 5. Initial droplet height in Chap. 6.

Zitterbewegung Trembling motion, from German.

$\mathfrak{A}$ Normalized, sheared droplet cross-sectional area. The area is normalized by W^2.

$\mathfrak{D}$ Deviatoric stress tensor.

$\mathfrak{H}$ Heaviside function.

$\mathfrak{V}$ Volume of grid cell.

∇_s Surface gradient operator along the wall.

∇_s^2 Surface Laplacian operator along the wall.

Δt Simulation time step.

Δx Grid cell size in the x-direction.

$\Delta\phi$ Change in the level set ϕ.

Φ Obtuse side indicator (Eq. 3.2).

a_1 Constant number.

a_2 Constant number.

c Positive constant.

d Approximate distance to the interface.

$f(\bar{x}, \boldsymbol{Ca}, \epsilon, \theta_S)$ Function representing the microscopic velocity curve $\bar{u}_S$ for the fluid with contact angle θ_S.

$g(\bar{x}, \boldsymbol{Ca}, \epsilon, 180^o - \theta_S)$ Function representing the microscopic velocity curve $\bar{u}_S$ for the fluid with contact angle $180^o - \theta_S$.

g Magnitude of the gravity vector. In Eq. 1.5, g is the known function from Cox [28].

$\vec{g}$ Gravitational acceleration vector.

$h(x)$ Dimensional height profile of the drop as a function of the spatial x-coordinate.

$\bar{h}$ Dimensionless height profile of the drop as a function of the spatial x-coordinate.

k Number of level set bands.

k_a Material-related advancing parameter in model I (Eq. 6.1) from Yokoi et al. [166].

k_b Boltzmann constant, $1.38 \cdot 10^{-23}\ m^2\ kg\ s^{-2}\ K^{-1}$.

k_r Material-related receding parameter in model I (Eq. 6.1) from Yokoi et al. [166].

$m(a, b)$ Function which returns the input argument with the smaller absolute value.

n Coordinate in the outward normal direction to a wall.

$\hat{n}$ Direction vector normal to the level set isocontours.

$\vec{n}$ Direction vector normal to a solid surface.

p Local fluid pressure.

r Radial cylindrical coordinate.

sgn -1/+1 depending on the orientation of the wall.

t Simulation time variable.

t_{end} End simulation time.

$\hat{t}_1$ First vector tangential to the fluid interface.

$\hat{t}_2$ Second vector tangential to the fluid interface.

u x-component of the velocity vector $\vec{u}$.

u_B Macroscopic velocity component.

u_n Extension velocity and normal component of the velocity vector $\vec{u}$ to the level set interface.

u_S Microscopic velocity component.

u_{tan} Wall tangential velocity component of the extension velocity u_n.

$\bar{u}_S$ Non-dimensional fluid velocity, $\bar{u}_S = u_S/(U_{CL} - U_B)$.

$\hat{u}$ General velocity vector.

$\vec{u}$ Local fluid velocity vector.

v y-component of the velocity vector $\vec{u}$.

w z-component of the velocity vector $\vec{u}$.

x Cartesian coordinate.This coordinate is often tangential to the solid walls in the present work.

x_{int} x-coordinate for the interface in Chap. 3 and 4.

x_0 Constant in the surface evolution equation that is related to the droplet volume.

$\bar{x}$ Non-dimensional x-coordinate centered at a, $\bar{x} = (x - a)/\lambda$.

$\bar{x}_0$ Dimensionless constant in the surface evolution equation that is related to the drop volume.

$\hat{x}$ Non-dimensional x-coordinate, $\hat{x} = x/\lambda$.

$\tilde{x}$ Closest point on the interface to a grid node.

$\vec{x}$ Spatial location vector for a target point.

$\vec{x}_1$ Spatial location vector for an accepted neighbor point in the FMM.

y Cartesian coordinate. This coordinate is often normal to the solid walls in the present work.

z Axial cylindrical coordinate or the third Cartesian coordinate.

α Angle of the circular arc initial condition.

β Shear factor (Eq. 6.2).

β_a Shear factor β for advancing contact lines.

β_r Shear factor β for receding contact lines.

γ Ratio of shear rate factors at different capillary number Ca.

δ Dirac delta function. In Eq. (2.22), it is a small parameter.

ϵ Ratio of a small and large length scale. The small length scale is usually the slip length λ and the large length scale either H or R.

ϵ_C Width of the fluid-fluid interface for the phase-field method.

η Fluid density ratio ρ_2/ρ_1.

θ Isocontour angle. For the zero isocontour, it is the contact angle.

θ_{app} Macroscale apparent contact angle.

θ_D Microscale dynamic contact angle.

θ_m Microscale contact angle.

θ_{max} Maximum contact angle θ allowed as a target angle in the relaxation equation (Eq. 3.5). Throughout this study, it is 170^o.

θ_{mda} Maximum advancing contact angle in model I (Eq. 6.1) from Yokoi et al. [166].

θ_{mdr} Minimum receding contact angle in model I (Eq. 6.1)from Yokoi et al. [166].

θ_{min} Minimum contact angle θ allowed as a target angle in the relaxation equation (Eq. 3.5). Throughout this study, it is 10^o.

θ_o Contact angle prior to reinitialization.

θ_S Static (equilibrium) contact angle.

θ_{sa} Static advancing contact angle.

θ_{sr} Static receding contact angle.

$\tilde{\theta}$ Propagated value of the isocontour angle θ in the blind spot.

$\tilde{\theta}_{max}$ Maximum value of the propagated angle $\tilde{\theta}$ allowed.

$\tilde{\theta}_{min}$ Minimum value of the propagated angle $\tilde{\theta}$ allowed.

κ Interface curvature.

κ_{app} Curvature applied in the GFM at the contact line.

κ_0 Frequency of molecular displacements.

κ_1 First mean curvature component, the standard 2D Cartesian coordinate curvature.

κ_2 Second mean curvature component, the curvature associated with the cylindrical surface.

$\bar{\kappa}$ Average curvature.

λ Slip length in the Navier-slip boundary condition.

μ Dynamic fluid viscosity.

μ_C Rate of change of free energy in the phase-field method.

μ_{eff} Effective dynamic viscosity at a contact line.

ξ Fluid viscosity ratio μ_2/μ_1.

ρ Fluid density.

σ Coefficient of surface tension.

σ_{s1} Free energy between the solid surface and fluid 1 in Young's equation (Eq. 1.1).

σ_{s2} Free energy between the solid surface and fluid 2 in Young's equation (Eq. 1.1).

τ Pseudo-time variable for iterating the reinitialization equation.

τ_{Ca} Capillary time scale, $\mu H/\sigma$.

τ_{We} Inertial-capillary time scale, $\sqrt{\rho H^3/\sigma}$.

υ Average displacement distance in molecular kinetic theory.

ϕ Level set variable. In this work, it is a signed distance function.

ϕ_{temp} Temporary value of the level set ϕ.

ϕ_0 Value of the level set ϕ prior to reinitialization.

ψ In Chap. 1, the bulk energy density in the Cahn-Hilliard equation (Eq. 1.7). In Chap. 2, the height fraction of fluid 1.

ω Wall tangential direction coordinates.

Chapter 1

Introduction

> *... not even Herakles could sink a solid if the physical model were entirely valid ...*
>
> — Huh and Scriven [67]

1.1 Motivation

Contact lines, the intersection of three immiscible material phases, are ubiquitous throughout nature and industrial applications. A contact line in 2D is a point and in 3D is a contour. Usually, in fluid mechanics, the contact-line phenomenon refers to the location where two fluids meet on a solid wall at a contact angle θ (Fig. 1.1). In capillary-driven fluid flows (large surface tension σ, small characteristic length scale), the contact-line behavior can control the flow. This thesis aims to develop a numerical framework where flows affected by contact lines can be studied and optimized efficiently. Interest in contact lines can be broken into three classes, namely understanding nature, industrial applications, and fundamental science.

Understanding nature:

Many optimal surface structures already exist in nature; by studying these biological surfaces, improved products can be designed. For example, lotus flowers and other plants (Fig. 1.2a) have superhydrophobic surfaces that shed water droplets using a combination of chemistry and microstructures [8, 104]. Analogous self-cleaning surfaces can be used for clothing, wind shields, or microfabrication

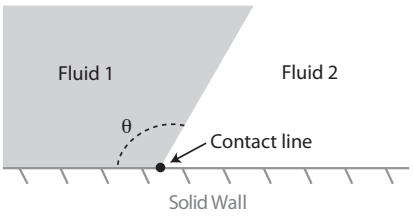

Figure 1.1: Contact line in 2D between fluid 1 and fluid 2. θ is the contact angle.

Figure 1.2: a) Lotus leaf [17]. b) Namibian beetle [106]. Images reproduced with permission from the Nature Publishing Group under licenses 3374961113213 and 3374931001319.

tools. Indeed, artificial surfaces have already been inspired by these leaves [17]. While lotus leaves repel water, other organisms such as beetles in the Namib Desert (Fig. 1.2b) have surfaces that collect water [55]. The beetle's wings have alternating hydrophobic and hydrophilic patches where water is gathered from the surrounding desert air [106]. This structure would be useful in fresh water condensers.

Industrial applications:

There are three broad geometries for most industrial contact-line applications: a single flat wall, surrounding flat walls, or porous media. For a single wall, the upper surface of the fluid is comparatively free. Applications of this type are inkjet printing [136], free-form manufacturing [101], airfoils [95], and ship hydrodynamics [144]. When a surrounding surface is present, the fluid is constrained on multiple sides by contact lines. Examples are pipe flows [7, 68, 84], microfluidic devices [139], and "low-g coffee cups" [161]. Lastly, porous media applications are the ultimate goal. Understanding flow in this geometry is important for optimizing reservoir oil and water recovery [74], water removal

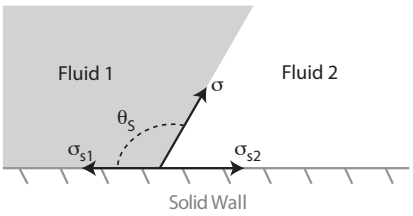

Figure 1.3: Diagram of the interfacial surface tensions for Young's equation (Eq. 1.1). θ_S is the equilibrium contact angle.

in polymer-electrolyte-membrane fuel cells [76, 150], and reaction control in microreactors [75]. With energy demands expected to rise by a third in the next 25 years [5], it is critical to maximize energy resource usage. While porous media are the ideal target, the first two cases should be developed beforehand due to their relative simplicity. These simpler cases will be used in the present work.

Fundamental science:

Despite their omnipresence and importance, understanding of contact lines is limited. Young [167] proposed the traditional formulation for the static contact angle θ_S at equilibrium which is now referred to as Young's equation (Fig. 1.3):

$$\sigma_{s2} + \sigma cos(\theta_S) = \sigma_{s1} \tag{1.1}$$

The free energies per unit area σ, σ_{s1}, and σ_{s2} are material properties and in thermodynamic equilibrium. Young's equation is only valid at equilibrium. Away from equilibrium, a new dynamic contact angle θ_D forms. This angle θ_D is sometimes represented by the unbalanced Young's force F_{Young},

$$F_{Young} = \sigma \left(cos(\theta_S) - cos(\theta_D)\right) \tag{1.2}$$

For a steady state flow, the contact angle can also be determined by, among other quantities, the amount of slip at the solid wall. While the standard no slip boundary condition has been widely accepted in fluid mechanics [10], this boundary condition has a complication at contact lines. If the

concept of no slip were indeed strictly valid, fluid 1 would never be able to replace fluid 2 along the solid and vice versa (Fig. 1.1). Examining Stokes flow in a liquid wedge at the contact line, Huh and Scriven [67] showed that the no slip boundary condition causes the shear stress to diverge as $1/r$, where r is the radial distance along the wall to the contact line. This non-integrable shear stress yields an infinite shear force which inspired the quote at the beginning of this chapter. The interface must be able to move with a contact line velocity U_{CL}. Contact lines challenge the postulates of fluid mechanics (namely the no slip condition) and must be handled differently both analytically and numerically. The following section describes the existing models for this region.

1.2 Prior contact-angle models

While contact lines have been studied extensively over the last 40 years, there is no universal theory. The physical definition of the dynamic contact angle is not even the same across different studies. The notation adopted here follows that of Sui et al. [140]: the contact angle observed at the macroscale is the apparent contact angle θ_{app} (Fig. 1.4a) while the angle observed on the microscale is the dynamic contact angle θ_D (Fig. 1.4b). These two angles are not equal in general. The existing models follow either a microscale (molecular kinetic) or macroscale (hydrodynamic) approach. From these scalings, molecular kinetic theory tends to approximate the dynamic contact angle θ_D while the hydrodynamic approach approximates the apparent contact angle θ_{app}. A brief overview for the molecular kinetic and hydrodynamics theories is presented in Secs. 1.2.1 and 1.2.2, respectively. A much larger variety of opinions exists in the literature describing potential models [14, 18, 29, 30, 114, 131, 135, 140, 162].

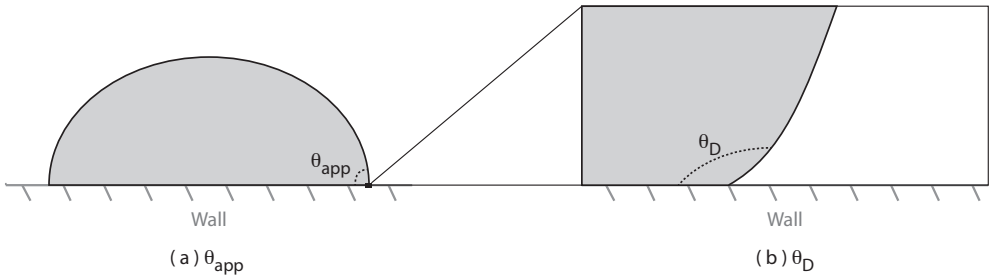

Figure 1.4: a) Apparent contact angle θ_{app} for a liquid droplet. b) Dynamic contact angle θ_D at the microscale.

1.2.1 Molecular kinetic theory

Yarnold and Mason [164] first proposed that the relationship between contact line velocity U_{CL} and the dynamic contact angle might be controlled by the molecular statistical dynamics. The driving force is the unbalanced Young's force (Eq. 1.2) and the contact-line motion occurs due to thermally-driven molecular response. The key parameters are the equilibrium frequency of random molecular displacements κ_0 and the average distance of displacement υ. Blake and Haynes [16] quantified the molecular kinetic theory as

$$U_{CL} = 2\kappa_0 \upsilon sinh\left[\frac{\sigma(cos\theta_S - cos\theta_D)\upsilon^2}{2k_B T}\right] \tag{1.3}$$

where k_b is the Boltzmann constant and T the absolute fluid temperature. Neither of the key parameters in this model can be easily measured and are typically fitted to experimental data.

1.2.2 Hydrodynamic theory

Unlike molecular kinetic theory which emphasizes the molecular energy dissipation, the hydrodynamic theories focus on the fluid viscous dissipation in the corner at the contact line (Fig. 1.1). There are two pieces to any hydrodynamics formulation: 1) a method to relieve the stress singularity inherent to the no slip boundary condition and 2) a macroscopic contact angle behavior that returns the contact angle θ to θ_S at equilibrium. Shikhmurzaev [130] gives an extensive overview of the different pieces used in literature.

A common choice to relieve the stress singularity is to use a Navier-slip boundary condition [98],

$$\frac{\partial u}{\partial n} = \frac{u}{\lambda} \tag{1.4}$$

where u is the velocity tangential to a solid wall, n is the direction normal to that wall, and λ is the slip length. The slip velocity is proportional to the shear rate which decays away from the contact line. This slip length λ is estimated to be on the order of nanometers [39, 92]; it is related to, but not equal to υ in the molecular kinetic theory.

Matched asymptotic, analytic solutions have been derived in the hydrodynamic framework as the ratio of the micro and macro length scales $\epsilon = L_m/L_M \rightarrow 0$ and the capillary number Ca $= \mu U_{CL}/\sigma \rightarrow 0$ where μ is the fluid dynamic viscosity. Cox [28] derived the apparent contact angle for a liquid-liquid system as

$$g(\theta_{app}) - g(\theta_m) = \text{Ca} \cdot \log(\frac{1}{\epsilon}) \tag{1.5}$$

where g is a known function. The microscale contact angle θ_m was set as the static contact angle θ_S in his analysis. He assumed a no slip boundary condition far away and stated that the slip condition at the contact line (whichever chosen) would only show up as an additional constant. Unfortunately, this relation cannot be used for finite Reynolds number flows (Re $= \rho U_{CL} L_M/\mu \neq 0$), nor when the capillary number Ca is large. Furthermore, it is unclear how the small or large length scales in the ratio ϵ should be defined. When typical length scales have been used, the resulting slip lengths can be unrealistically small [11, 92]. To fit more realistic slip lengths, other studies have combined molecular kinetic ideas and hydrodynamic models through the microscopic contact angle θ_m [20, 107, 128]. This approach, however, risks over-parameterizing the problem since there are now at least three parameters to fit experimental data.

1.2.3 Non-unique contact angles

In both the molecular kinetic theory and hydrodynamic models, the contact angle is assumed to be a unique function of material properties and standard parameters: however, there is experimental evidence that implies the contact angle may be multivalued for finite Reynolds number. Blake et al. [15] performed a series of curtain-coating experiments and found that the flow rate of the curtain fluid affected the contact angle. This result implies that the hydrodynamics far away from the contact line are important. For example, in curtain coating, the finite film thickness and its free fluid surface can affect the contact angle. A subsequent study by Clark and Stattersfield [27] found similar results where a recirculation region could form. In addition, a series of experiments and simulations by Ding and Spelt [36], Ding et al. [35], and Sui and Spelt [142] for rapidly spreading drops showed that the apparent contact angle is non-unique when inertial effects are important. Since a single equation cannot easily capture this multivalued function, a simulation framework is sought where the contact angle evolves naturally from all physical effects involved.

1.3 Numerical methods for multiphase flow and contact lines

From the existing model descriptions of the dynamic or apparent contact angles (Sec. 1.2), it is clear that the contact line phenomenon is a multiscale problem in most applications: the scale λ ($\sim nm$) is much smaller than the fluid structure dimension ($> mm$). Existing numerical techniques to handle these multiphase flows are discussed briefly below. They can be defined by the chosen length scale: atomistic (Sec. 1.3.1) or continuum (Sec. 1.3.2) approaches. The particular continuum, front-capturing approach used throughout this work is the level set method; it is discussed more extensively. Only the most common methods are mentioned here to contrast with the level set method; more complete numerical method reviews are available in Refs. [52, 99, 140, 162].

1.3.1 Atomistic methods

Atomistic approaches seek to model the interaction of molecular particles and subsequently capture the macroscale fluid behavior [72]. Molecular dynamics (MD) is the most well-known of these techniques. In MD, discrete atoms affect each other through interaction potentials such as the Lennard-Jones potential [85]. All results are subject to the validity of the chosen potential. The macroscale fluid properties such as the flow velocity are calculated from suitable particle averages. Examples of molecular dynamics studies for contact lines are Koplik et al. [79], Thompson and Robbins [151], Qian et al. [112], and Ren and E [115]. The advantages of MD are that it is a very fundamental approach and may capture physics more accurately (particularly on the nanoscale) than continuum methods. Furthermore, it does not require the solution of multidimensional, partial differential equations. The major disadvantage is MD's computational expense: computational effort increases linearly with the number of particles and simulation run-time. Historically, MD simulations have been limited to only small collections of molecules [72]. One of the largest simulations to date [51] has 7 orders of magnitude fewer particles than are necessary to simulate a cubic millimeter of water. While some hybrid atomistic-continuum simulation methods have been proposed [50, 53, 54], other authors argue that these two approaches are inherently incompatible and should not be coupled in this way [132]. While MD simulations are useful for probing scientific questions, their applicability to realistic problems is limited.

1.3.2 Continuum methods

While the atomistic methods target the length scale of molecular processes λ, continuum methods are more appropriate for focusing on the length scale of fluid structures. Front-tracking and front-capturing methods are described in Sec. 1.3.2.1 and 1.3.2.2, respectively.

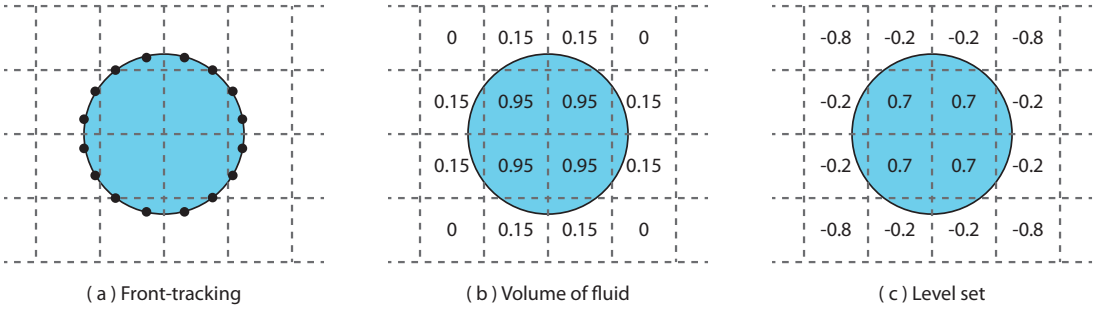

Figure 1.5: Diagrams for the different reinitialization schemes. (•) are the marker particles in a front-tracking method. Note: the values in (b) and (c) are for illustration only.

1.3.2.1 Front-tracking methods

These methods explicitly track the location of the fluid interface, usually using marker particles. A circular interface with marker particles (dots) is shown in Fig. 1.5a. These marker particles are transported with the local fluid velocity in a Lagrangian fashion and the new interface is identified by these points. One of the earliest front-tracking methods is the marker-and-cell (MAC) approach of Harlow and Welch [57] for free surface flows. In the MAC method, each liquid grid cell was seeded with marker particles. Any cell containing a marker particle after transport was identified as fluid. There is no connectivity between the particles in this formula and they are spread throughout the fluid volume. Unverdi and Tryggvason [154] proposed a front-tracking method using particles only on the interface with known connectivity. The advantages of this method are that it is easy to visualize and the exact location of the interface is known. However, while it is conceptually simple, its implementation is not. Special numerical rules are needed to remove / add marker particles as neighboring particles get too close / far apart. Front-tracking methods have particular difficulties handling merging surfaces; thin fluid filaments will persist unless a devoted routine removes them.

1.3.2.2 Front-capturing methods

Unlike front-tracking methods, front-capturing methods do not explicitly track the fluid interface; rather, each grid node is assigned a scalar value related to the interface. The exact interface location is unknown; however, an appropriate location can be reconstructed from the scalar values. One of

the major benefits of these methods over front-tracking methods is that they naturally handle merging interfaces and topological changes. This benefit comes at the loss of fine scale features on coarse meshes, features that front-tracking methods preserve. Capturing merging interfaces and fine fluid threads are nearly mutually exclusive conditions. Furthermore, whereas front-tracking methods may require special data constructs to store the interface information and connectivity, the scalar values of front-capturing methods are stored like any other scalar variable. These methods, therefore, are easily extended to 3D. Three types of front-capturing methods are volume of fluid, phase field, and level set methods.

Volume of fluid method:

The volume of fluid method (VOF) was first introduced by Hirt and Nichols [62]. VOF methods have been previously used by Renardy et al. [116], Afkhami et al. [3, 4], and Dupont and Legendre [37] to simulate contact line movement. In a VOF method, each grid cell is assigned a color function C (or volume fraction) that represents the amount of fluid 1 present in the cell. If the cell is entirely fluid 1, $C = 1$; if it is entirely fluid 2, $C = 0$. An example of volume fractions for a circular interface is shown in Fig. 1.5b. The color function C is transported using the advection equation,

$$\frac{\partial C}{\partial t} + \vec{u} \cdot \nabla C = 0 \tag{1.6}$$

where $\vec{u}$ is the local fluid velocity. The primary benefit of VOF methods for incompressible flows is that mass is exactly conserved if Eq. 1.6 is reformulated in its conservative form. The major disadvantage is the difficulty in reconstructing the fluid interface; the interface location is not obvious [121]. This disadvantage raises concerns when calculating interface normals and curvature. If the interface is sharp (an abrupt transition between $C = 0$ and 1), these quantities are poorly calculated. VOF methods, therefore, typically smear the fluid interface over several grid cells to facilitate easier calculations; all VOF methods have some level of numerical smearing [122]. This diffuse interface has other spurious effects for large fluid density and viscosity ratios, although the effects disappear

with shrinking grid dimensions. Since curvature must be accurate in surface-tension-dominated fluid flows, the VOF method is not appropriate for the present work.

Phase field method:

Like VOF methods, phase-field methods use a color function C to distinguish between fluids. A chemical transport equation, the Cahn-Hilliard equation

$$\frac{\partial C}{\partial t} + (\vec{u} \cdot \nabla) C = \nabla \cdot (M \nabla \mu_C) \ , \tag{1.7}$$

is used instead of Eq. 1.6 for VOF methods [162]. The interface is spread over several cells to indicate the transition layer between the two fluids. $M(C)$ is a diffusion parameter called the mobility. This chemical diffusion is one of the strengths of this approach; the contact line can diffuse along the surface and the contact-line stress singularity is relieved even for a no slip boundary condition. The rate of change of free energy is μ_C. This parameter contains the two drawbacks of the phase field method. μ_C is expressed as

$$\mu_C = \frac{\partial \psi}{\partial C} - \epsilon_C^2 \nabla^2 C \tag{1.8}$$

where ϵ_C is a width indicative of the fluid-fluid interface thickness and ψ is the bulk energy density. For realistic cases, ϵ_C may be very small, requiring high resolution simulations. Furthermore, when Eq. 1.8 is used in Eq. 1.7, the Cahn-Hilliard equation contains fourth-order derivatives of the color function C. These high-order derivatives require special treatment. Examples of studies using the phase field method for multiphase flows are Jacqmin [69, 70], Lowengrub and Truskinovsky [88], Yue et al. [169], and Carlson et al. [22].

Level set method:

In the level set method of Osher and Sethian [103], the fluid interface is embedded as the zero value of a scalar variable ϕ [102]. The choice of ϕ is arbitrary, but it is subject to two constraints: it must be smooth and continuous. These constraints allow accurate interpolation of the zero level set and

computation of isocontour normal vectors $\hat{n}$ and curvatures κ,

$$\hat{n} = \frac{\nabla\phi}{|\nabla\phi|}, \qquad \kappa = -\nabla \cdot \hat{n} \ . \tag{1.9}$$

The level set method is used in the present work for this reason; accurate curvature is important in capillary-dominated fluid flows. Two common choices of ϕ are a signed distance function (interface $\phi = 0$) [97, 26] and a conservative hyperbolic tangent distance function [100, 170, 34] (interface $\phi = 0.5$). Only the signed distance function, the more common choice in literature, is considered in this work. A signed distance function for a circular interface is shown in Fig. 1.5c. If $\phi > 0$, the cell center is in fluid 1; if $\phi < 0$, it is in fluid 2. The mathematical condition for a signed distance function is a unity gradient magnitude, $|\nabla\phi| = 1$.

The level set function ϕ is typically evolved in two steps: an advection step and a reinitialization step. First, to transport the interface, the level-set variable ϕ is advected with the local fluid velocity $\vec{u}$ to determine the new interface location using an advection equation

$$\frac{\partial\phi}{\partial t} + \vec{u} \cdot \nabla\phi = 0 \ . \tag{1.10}$$

Unfortunately, after transport, ϕ is in general no longer a distance function. While the simulation can proceed using a non-distance function ϕ, the constraints (namely, a smooth and continuous ϕ field) may no longer be satisfied after multiple iterations. If the gradients of ϕ become large or small, the benefit of accurate curvature is lost. This distortion of level set isocontours caused by fluid motion necessitates the second step, reinitialization [24, 145, 171].

The reinitialization step was first introduced by Chopp [26] to correct the "tent pole" phenomenon where level set isocontours became bunched. The fundamental idea of reinitialization is to return the level set ϕ to a signed distance function ($|\nabla\phi| = 1$), while preserving the location of the interface $\phi = 0$. The simplest approach is to track marker particles on the surface, similar to the

front-tracking method (Fig. 1.5a). A grid node's distance d to each marker is calculated and the smallest value d is set as the new level set magnitude. This direct method is very computationally expensive. In addition, its extension to 3D is non-trivial and requires constructing fluid interface panels [144].

The second approach is Fast Marching Method (FMM) [1, 124, 125]. The FMM solves the Eikonal equation,

$$|\nabla\phi|^2 = 1 \tag{1.11}$$

for the distance function and marches values out from the interface. This method is quite efficient computationally. However, this method is usually only first order accurate. Therefore, the curvature would be less accurate since it requires second-order derivatives of ϕ (Eq. 1.9). While second-order FMM methods do exist [124], they are more challenging to implement. Other authors have been unable to extend the FMM to even higher order accuracy; there are finite-difference stencil and stability issues [99].

The third reinitialization technique iterates a partial differential equation in pseudo-time τ until steady state. A standard equation is the Hamilton-Jacobi equation given by [145]

$$\frac{\partial\phi}{\partial\tau} + sign\left(\phi_0\right)\left(|\nabla\phi| - 1\right) = 0\ . \tag{1.12}$$

ϕ_0 is the value of ϕ prior to reinitialization. This equation is hyperbolic and its characteristics are normal to the interface $\phi = 0$ (Fig. 3.1). At steady state, $|\nabla\phi| = 1$, the condition for a signed distance function. This approach is used here because it is more efficient than the direct approach and can use high-order discretizations easily, unlike the FMM.

The main disadvantage of the level set method is poor mass conservation, particularly after reinitialization. Many approaches have been proposed to alleviate this loss. The simplest method

is to readjust the value of the level set ϕ after reinitialization such that the fluid volume before and after reinitialization are equal [137]. This approach may artificially move the fluid interface. Another strategy modifies Eq. 1.12. Russo and Smereka [117] proposed a different discretization with better mass conservation. Hartmann et al. [58, 59] added additional source terms to pin the location of the zero level set. In addition, there are several hybrid techniques that couple two techniques: level set and front-tracking [99, 133], level set and VOF [94, 146], and level set and particle methods [40, 61].

1.4 Thesis outline

The first goal of this work is **to create a numerical framework that allows the contact angle to evolve naturally with appropriate contact-line physics.** Unlike prior work, no dynamic or apparent contact-angle law is strictly applied. Such an approach is particularly useful for cases where the Reynolds number Re and capillary numbers Ca are large since there are no complete theories in these regimes at this time. Furthermore, the multivalued contact angle mentioned in Sec. 1.2.3 is not problematic since a contact-angle law is not prescribed. The framework will be derived with certain physical assumptions, but other physical mechanisms can be incorporated if necessary.

The second goal of this work is **to develop equations and numerical methods such that contact-line simulations may be run on coarse computational meshes.** Surface tension is usually treated explicitly due to the non-linearity of curvature with the level set variable ϕ (Eq. 1.9). The explicit stability condition for surface tension (Eq. 2.20) is particularly severe because highly refined grids are necessary for multiscale contact line problems. Therefore, it is useful to not resolve the smallest length scales such as the slip length λ. Normally, relevant contact-line physics are missed if this length scale is not resolved. By capturing the relevant contact-line physics on coarse meshes, simulations are feasible on moderate capability computer clusters.

The first goal is accomplished in Chap. 3–5. This goal focuses on reducing numerical errors of existing methods for floating (non-prescribed) contact angles and creating physical source terms. The second goal of computationally efficient simulations is attained in Chap. 5 and 6. Contact-line physics are not included in Chap. 3 and 4; the numerical methods alone are examined. The contact-line physics are reintroduced in Chap. 5.

Chapter 2 describes the governing equations for multiphase flow and credits the existing numerical methods that are employed throughout. This chapter may be skipped without loss of continuity.

Before the level set method is used at a contact line, the numerical methods for a freely floating contact angle must be checked to ensure that they do not introduce spurious effects. Chapter 3 resolves a subtle point about level set reinitialization. This has to do with the "blind spot" created near the contact line; this region has no characteristics from the Hamilton-Jacobi equation (Eq. 1.12). A relaxation equation is then proposed that minimizes the errors caused by this ill-posed problem.

Chapter 4 expands the concepts of Chap. 3 to level-set extension velocities and offers a solution to ensure correct contact angles in the relaxation equation. The reinitialization technique is completed by supplementing it with an angle propagation algorithm. This combined algorithm is referred to as the relaxation equation reinitialization.

The physics at a contact line are included in Chap. 5. Classical boundary conditions are used to derive the volumetric source terms that need to be considered when the mesh grid is much larger than the slip length λ. These terms, the average curvature and viscous shear force, are then approximated from DNS of contact lines.

In Chap. 6, all of the previously derived source terms and numerical methods are combined into a complete framework. Drop impacts are difficult to capture using existing contact angle relations because of the large fluid velocities (Re>1, Ca>1). A drop impact experiment and its simulated counterpart are compared. The slip length λ is adjusted to the experimental data and the value obtained is surprisingly realistic. Good agreement is shown: the methods created here are quite promising.

Chapter 7 presents a brief summary of this work and suggestions for future extension are discussed.

1.5 Contributions

This work makes the following contributions:

- A new relaxation equation is added to the level-set reinitialization which holds curvature constant in the blind spot. This technique introduces minimal numerical errors and is easily extended to 3D. (Chap. 3)
- The concept of fixed curvature is included in a new technique to create consistent level-set extension velocities along the solid boundary. (Chap. 4)
- The level-set relaxation equation is completed by including angle propagation. This surface propagation has not been previously seen in the literature. (Chap. 4)
- The former contributions create a framework where the contact angle can be left floating; it is determined by the physics. This approach is important for finite Reynolds number effects. (Chap. 3–4)
- A weak boundary condition forcing term is used to apply a constant angle in the direct numerical simulations. Prior approaches reinitialized at every time step to force a contact angle. The weak condition with the relaxation equation allows the reinitialization frequency to be reduced, greatly reducing the simulation computational cost. (Chap. 5)

- Two modeled terms, the average curvature and the viscous shear force, are determined as necessary for simulations where the mesh size is much larger than the slip length λ. These terms are analyzed for a Navier-slip boundary condition and fixed angle. The shear force has never been fully analyzed as a function of slip length and contact angle before with these boundary conditions. (Chap. 5)

- All the pieces are combined for a realistic experimental comparison. Only one parameter, the slip length, is determined empirically using the experimental data. The slip length predicted is outside of the current range of existing DNS and is surprisingly realistic. This is the first step towards simulations that are under-resolved and efficient, yet, still capture the contact-line physics. (Chap. 6)

Chapter 2

Numerical methods

Study the past, if you would divine the future.

— Confucius

2.1 Introduction

The purpose of this chapter is not to introduce any new techniques, but to credit the existing numerical methods used throughout this work. When appropriate, alternative methods and justification for the choices used here are discussed. Section 2.2 describes the equations governing fluid motion. The underlying numerical framework is the research code Next Generation ARTS (NGA) [33]. The fluid mechanics equations are solved at full time steps $N\Delta t$ and changes in the level set ϕ occur at half time steps $(2N+1)\Delta t/2$ where N is a positive integer. Sections 2.3 and 2.4 describe the methods used in these steps, respectively.

2.2 Governing equations

The two fluids are assumed to be immiscible, incompressible, and Newtonian. The equations of motion are the incompressible Navier-Stokes and continuity equations,

$$\frac{\partial \rho \vec{u}}{\partial t} + \nabla \cdot (\rho \vec{u} \otimes \vec{u}) = \nabla \cdot (-pI + \mathfrak{D}) + \rho \vec{g}, \tag{2.1}$$

$$\nabla \cdot \vec{u} = 0, \tag{2.2}$$

where t is the simulation time, $\vec{u}$ the velocity vector, p the fluid pressure, $\vec{g}$ the gravity vector, ρ the density, I the identity matrix, and $\mathfrak{D}$ the deviatoric stress tensor [10]. For a Newtonian fluid, the deviatoric stress tensor $\mathfrak{D}$ is

$$\mathfrak{D} = \mu \left(\nabla \vec{u} + \nabla \vec{u}^T - \frac{1}{3} (\nabla \cdot \vec{u}) I \right) = \mu \left(\nabla \vec{u} + \nabla \vec{u}^T \right) \tag{2.3}$$

where μ is the dynamic viscosity. The velocity boundary conditions at a solid surface with normal $\vec{n}$ are the no penetration,

$$\vec{u} \cdot \vec{n} = 0 \, , \tag{2.4}$$

and the Navier-slip boundary condition (Eq. 1.4).

At the fluid-fluid interface, in the absence of phase changes, the fluid velocity field is continuous,

$$[\vec{u}] = 0 \, , \tag{2.5}$$

where the square brackets represent a jump between fluid 1 and 2. There is no slip between the two fluids. The fluid-fluid interface moves with the fluid velocity $\vec{u}$ by advection. Let $\hat{t}_1$, $\hat{t}_2$, and $\hat{n}$ be the two tangential vectors and normal vector to the interface, respectively. Surface tension σ is assumed constant such that there are no Marangoni effects. The tangential stress at the interface is continuous,

$$\left[\hat{t}_1 \cdot (-pI + D) \cdot \hat{n} \right] = \left[\hat{t}_2 \cdot (-pI + D) \cdot \hat{n} \right] = 0 \, , \tag{2.6}$$

and the normal stress jump is given by the Laplace condition [82]

$$[p] = \sigma \kappa + 2 \, [\mu] \, \hat{n} \cdot \nabla \vec{v} \cdot \hat{n} \tag{2.7}$$

where κ is the interface curvature.

2.3 Fluid mechanics numerical methods

The numerical methods used in this work for the fluid mechanics can be broken into two categories. The first (Sec. 2.3.1) consists of methods that apply to general solutions of the Navier-Stokes equations, for both single and multiphase flow. The second (Sec. 2.3.2) consists of methods that are specific to multiphase flows. Section 2.3.3 discusses the numerical stability conditions associated with these methods.

2.3.1 Implementation of the Navier-Stokes equations

In the NGA framework [33], the scalar information (ϕ, ρ, μ, p) and the velocity variables (u,v,w) are staggered in space and time. The spatial staggering of variables is done in accordance with the MAC grid [57]. This framework employs second-order accurate finite-difference discretizations for Eqs. 2.1 and 2.2. The advection terms are always solved explicitly while the viscous terms can be solved either explicitly or implicitly using the approximate factorization techniques similar to one used by Choi and Moin [25]. The temporal integration is done using the second-order, semi-implicit Crank-Nicolson scheme of Pierce and Moin [108]. In order to apply the incompressibility condition (Eq. 2.2), a pressure projection method [45] is used and the velocity $\vec{u}$ is evaluated iteratively. The HYPRE implementation of the Boomer algebraic multigrid (AMG) [60] is used to solve Poisson's equation for pressure in Cartesian coordinates and the streaming multigrid (SMG) implementation in cylindrical coordinates. These solvers converge very rapidly and solve the linear algebra system very efficiently; however, they did not always converge in some simulations. When the multigrid solvers did not converge, a bi-conjugate gradient stabilized iterative solver (BiCGStab) [157] was used instead. While BiCGStab in practice may be more stable than multigrid methods, it often converges far more slowly [138].

2.3.2 Multiphase flow treatment

For multiphase fluid mechanics, additional numerical components are required: momentum source terms for the normal stress imbalance due to surface tension (Eq. 2.7) and mixture rules for density ρ and dynamic viscosity μ. There are two general classes: diffuse and sharp interface methods. For diffuse methods, the source terms and fluid property transitions are applied over several grid cells. The continuum surface force (CSF) model of Brackbill et al. [19] is often used to apply surface tension. In this model, the additional term

$$F = \sigma\kappa\delta\left(\phi\right) \tag{2.8}$$

is added to the right side of Eq. 2.1 where δ is a smeared representation of the Dirac delta function. Similarly for the fluid properties,

$$\rho\left(\phi\right) = \rho_2 + \left(\rho_2 - \rho_1\right)\mathfrak{H}\left(\phi\right) \tag{2.9}$$

$$\mu\left(\phi\right) = \mu_2 + \left(\mu_2 - \mu_1\right)\mathfrak{H}\left(\phi\right) \tag{2.10}$$

where $\mathfrak{H}$ is a smeared Heaviside function. Examples of smeared Heaviside and Dirac delta functions are

$$\mathfrak{H}\left(\phi\right) = \begin{cases} 0, & \phi < -\epsilon \\ \frac{1}{2} + \frac{\phi}{2\epsilon} + \frac{1}{2\pi}sin\left(\frac{\pi\phi}{\epsilon}\right), & -\epsilon \leq \phi \leq \epsilon \\ 1, & \epsilon < \phi \end{cases} \tag{2.11}$$

$$\delta\left(\phi\right) = \begin{cases} 0, & \phi < -\epsilon \\ \frac{1}{2\epsilon} + \frac{1}{2\epsilon}cos\left(\frac{\pi\phi}{\epsilon}\right), & -\epsilon \leq \phi \leq \epsilon \\ 0, & \epsilon < \phi \end{cases} \tag{2.12}$$

where ϵ is a multiple of the grid spacing, $N\Delta x,\ N > 1$ [145]. While the interface is sharp, these mixture rules for fluid properties are representative fluid properties at cell faces when the interface

divides a grid cell. Diffusive methods, however, are known to generate unphysical fluid velocities, "parasitic currents" [81]. These velocity currents are also known as spurious currents. Popinet and Zaleski [110] investigated the source of these currents for a 2D stationary fluid droplet of diameter D. They hypothesized that parasitic currents result from inconsistent modelling of the surface tension terms and the associated pressure jump. For cases where the Laplace number $\mathrm{La} = \sigma\rho D/\mu^2$ was large, they noted "spurious currents develop a kind of turbulence, shaking the droplet in a kind of *Zitterbewegung*". In the cases studied here where the surface tension is dominant, such interface deformations will make the solution inaccurate. Popinet and Zaleski concluded that sharp interface methods that capture the discontinuity may relieve these parasitic currents. One sharp interface method, the ghost fluid method (GFM), creates ghost values of each fluid in the other. The method was first developed for the inviscid Euler equations [43], but has been extended to incompressible fluid flows [73]. Kang et al. [73] further showed the benefits of the sharp interface methods over their diffuse counterparts. For both a 2D bubble and drop, the GFM had better area conservation as well as a reduction of parasitic velocity currents by a factor of 1,000. In addition, for instabilities, the CSF model was found to have a larger amount of numerical damping than the GFM. A further study by Francois et al. [48] compared continuous and sharp interface methods (not GFM) for stationary droplets with different fluid density ratios. Only the sharp interface method had machine-precision spurious currents and pressure errors when the curvature of the droplet was exactly specified. This work also studied rising bubbles with small Bond number, $\mathrm{Bo} = \rho g D^2/\sigma$. The sharp-interface bubble showed more deformation at the trailing bubble edges than the bubble with continuous pressure. This difference suggests the importance of accurately capturing the pressure jump in multiphase flow with large surface tension. While these results imply that the sharp interface methods are superior for surface tension dominated flows, Francois et al. did note that the sharp interface methods were more sensitive to curvature errors than their continuous formulation. Despite this potential sensitivity, the GFM from Kang et al. [73] is used in this work since the flows studied are dominated by surface tension.

There are some differences between the mixture rules used in this work and in Kang et al. [73]. Density is a linear combination of ρ_1 and ρ_2,

$$\rho = \rho_1\psi + \rho_2(1-\psi)\ , \tag{2.13}$$

and viscosity is a harmonic combination of μ_1 and μ_2,

$$\mu = \frac{\mu_1\mu_2}{\mu_1(1-\psi)+\mu_2\psi} \tag{2.14}$$

ψ is a height fraction : it is comparable to the amount of fluid 1 present in a VOF framework. For a staggered grid, the height fraction ψ at cell faces is,

$$\psi_{i+1/2,j} = \begin{cases} 1 & \phi_{i+1,j} \geq 0 \text{ and } \phi_{i,j} \geq 0 \\ 0 & \phi_{i+1,j} \leq 0 \text{ and } \phi_{i,j} \leq 0 \\ \frac{\phi^+_{i+1,j}+\phi^+_{i,j}}{|\phi_{i+1,j}|+|\phi_{i,j}|} & \text{otherwise} \end{cases} \tag{2.15}$$

and for cell vertices

$$\psi_{i+1/2,j+1/2} = \begin{cases} 1 & \phi_{i+1,j} \geq 0,\ \phi_{i,j} \geq 0,\ \phi_{i,j+1} \geq 0, \text{ and } \phi_{i+1,j+1} \geq 0 \\ 0 & \phi_{i+1,j} < 0,\ \phi_{i,j} < 0,\ \phi_{i,j+1} < 0, \text{ and } \phi_{i+1,j+1} < 0 \\ \frac{\phi^+_{i+1,j}+\phi^+_{i,j}+\phi^+_{i,j+1}+\phi^+_{i+1,j+1}}{|\phi_{i+1,j}|+|\phi_{i,j}|+|\phi_{i,j+1}|+|\phi_{i+1,j+1}|} & \text{otherwise} \end{cases} \tag{2.16}$$

The "+" superscript is a shorthand notation for $\phi^+ = max(\phi, 0)$. Unlike the formulation of Kang et al. [73], the viscous jump terms are not included. Excluding these terms results in a small amount of numerical smearing, but *a priori* knowledge of the property jumps is not required. Since the viscosity field is sharp but continuous, the Laplace condition (Eq. 2.7) is reduced to

$$[p] = \sigma\kappa\ . \tag{2.17}$$

and the tangential stress condition (Eq. 2.6) is automatically satisfied. The normal pressure jump

in Eq. 2.17 is applied as a source term in the pressure projection method.

2.3.3 Numerical stability

The simulation time step can be specified by either a fixed time step Δt or a suitable Courant-Friedrichs-Lewy (CFL) number for the explicit numerical discretizations. CFL numbers are a function of the time step Δt, the grid spacing Δx, and appropriate fluid parameters for a numerical discretization of a fluid mechanics term. As long as the CFL number is less than a fixed value, normally 1, the numerical methods should be stable although CFL values less than the limit can be used for higher temporal accuracy. There are three relevant CFL conditions in the NGA framework that correspond to different parts of the fluid mechanics: an advective CFL condition for the inertial terms of the Navier-Stokes equations, a viscous CFL condition for the deviatoric term, and a surface tension CFL condition for the normal stress jump condition. While some conditions depend on the direction (x, y, z), for simplicity only the x-direction conditions are shown below. The standard advective CFL condition [148],

$$CFL_a = \frac{u_{max}\Delta t}{\Delta x} \tag{2.18}$$

is not dominant for the flows considered here. The corresponding term in Eq. 2.1 are treated explicitly without stability concerns. The viscous CFL condition [153],

$$CFL_v = \frac{4\mu\Delta t}{\rho\Delta x^2} \tag{2.19}$$

is restrictive for Stokes flow (when Reynolds number $\mathrm{Re} < 1$) since the Navier-Stokes equations (Eq. 2.1) would become elliptic. Therefore, the viscous terms of Eq. 2.1 are often treated in an implicit manner in this work, thereby removing this restriction. The last CFL condition, associated with surface tension, gives rise to the most restrictive time constraint for surface tension dominated flows. The standard formulation is

$$CFL_\sigma = \Delta t\sqrt{\frac{\pi\sigma}{(\rho_1+\rho_2)\Delta x^3}}\,, \tag{2.20}$$

which is associated with the propagation of capillary waves [153]. This time restriction is particularly severe for grid-resolved solutions because the time step Δt scales like $\Delta x^{3/2}$. Kang et al. [73] proposed a less restrictive condition using the interface curvature κ,

$$CFL_\sigma = \Delta t \sqrt{\frac{\sigma|\kappa|}{min(\rho_1, \rho_2)\Delta x^2}} \tag{2.21}$$

which has the same scaling as Eq. 2.20 when the maximum grid-resolved curvature of $|\kappa| = 1/\Delta x$ occurs. In practice, the first condition (Eq. 2.20) is more common in literature and may be more robust than the second (Eq. 2.21). The time step is chosen such that all CFL conditions are satisfied.

2.4 Level set formulation

The level set formulation at half-time steps is composed of four components. These methods are specific to handling the fluid-fluid interface location. Sections 2.4.1 and 2.4.2 discuss the numerical methods for the advection and reinitialization of the level set ϕ, respectively. Computationally efficient narrow band methods are described in Sec. 2.4.3: this variant decreases the total simulation run-time. Finally, the interface curvature calculation for the normal stress jump condition (Eq. 2.17) is specified in Sec. 2.4.4. These techniques are the basis for fluid flows without contact lines and will be expanded upon in subsequent chapters.

2.4.1 Level set advection

Equation 1.10 is a scalar advection equation when fluid velocity $\vec{u}$ is used to transport the level set ϕ. A plethora of numerical techniques exist for equations of this form [41]. Broadly speaking, two categories are Eulerian and semi-Lagrangian (characteristic) techniques. Eulerian schemes use discretized approximations for $\nabla\phi$ and this form is directly substituted in Eq. 1.10. These approaches are easy to implement explicitly and the simulation error decreases with time step Δt. However, Eulerian schemes can have restrictive CFL conditions and high-order implementations

suffer from Runge's phenomenon at discontinuities. Neither of these disadvantages are a problem in this study since the advection CFL condition (Eq. 2.18) is not limiting the time step and the signed distance function should be smooth. Semi-Lagrangian schemes, on the other hand, back trace along characteristics to transport the level set. These techniques are popular for DNS of turbulent flows since they are more stable and allow much larger simulation time steps Δt than Eulerian techniques [93, 163]. The overall error for these methods, however, does not decrease monotonically with time step Δt [42, 159]. The time step Δt throughout this work has a very low advection CFL number; therefore, a semi-Lagrangian scheme is ill-suited for this work because the error from the advection equation can be large. Hence, an Eulerian method will be used.

A finite-difference form of the quadratic upstream interpolation for convective kinematics (QUICK) scheme [86] was used to discretize Eq. 1.10. Although the basic scheme uses third-order finite-difference approximations for the derivatives of ϕ, reduced-order finite-difference stencils are used along the walls to approximate the normal derivative in the advection equation (Eq. 1.10). This change excludes information stored in the wall cells (when applicable). Since wall normal velocities are small due to the no penetration boundary condition, these low-order stencils should not significantly affect the solution.

In Chap. 4, an alternative to the advection equation with fluid velocity $\vec{u}$ is shown. A discussion of this variant is left until that chapter.

2.4.2 Reinitialization

For reinitialization, the modified reinitialization equation (HCR2) proposed by Hartmann et al. [59] is used instead of Eq. 1.12,

$$\frac{\partial \phi}{\partial \tau} + \frac{\phi_0}{\sqrt{\phi_0^2 + \delta^2}} \left(|\nabla \phi| - 1 \right) = \frac{1}{2} F \ . \tag{2.22}$$

The coefficient $\phi_0/\sqrt{\phi_0^2+\delta^2}$ is an approximation for the sign function where δ is a small parameter (10^{-9}). The right hand term F is a forcing function that acts on the cells immediately next to the interface ($\phi = 0$) and is intended to pin the zero level set at a point in each cell. This form of the equation has been shown to have better mass conservation properties than the original Hamilton-Jacobi equation [59]. For all points adjacent to the wall, the forcing term F is set to zero and the reinitialization equation reduces to Eq. 1.12. While some of the other techniques discussed in Sec. 1.3.2.2 may have better mass conservation, this variant was chosen for its computational efficiency, ease of implementation, and simple extension to high-order discretizations. To have exact mass conservation, an additional reinitialization step could adjust the interface level set ϕ [137]. For example, the redefining the level set $\phi = -0.1$ as the interface would increase the amount of fluid 1. This approach, however, would artificially redistribute mass from areas smoothed during reinitialization (i.e., cusps) over the entire material surface. As such, the HCR2 scheme is used without additional modification.

The reinitialization equation (Eq. 2.22) is integrated in pseudo-time τ using a second-order Runge-Kutta scheme with a CFL number of 0.5. This medium-size CFL number ensures the stability of the integration as well as quick convergence to steady state. Unless otherwise noted, the gradient $\nabla\phi$ is discretized using the weighted essentially non-oscillatory (WENO) scheme of Jiang and Peng [71]. Third-order discretizations are used for the reinitialization equation because interface curvature requires the second spatial derivatives of the level set variable ϕ and, thus, high accuracy is desirable.

2.4.3 Narrow band methods

While it is possible to keep the level set variable ϕ in the entire domain, the exact values of ϕ are only necessary near the fluid interface; the remaining information is superfluous. To reduce the number of computational operations, Chopp [26] proposed only storing level set information in a

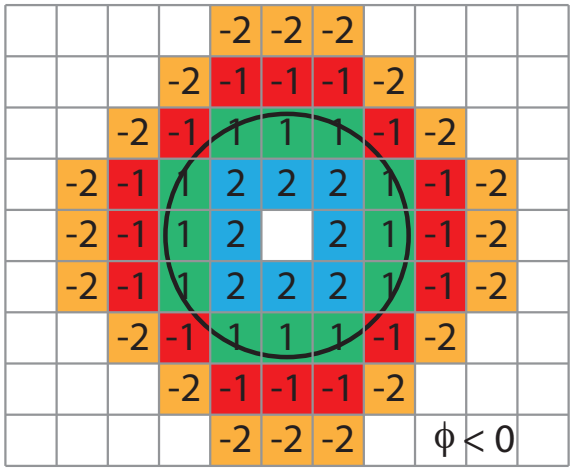

Figure 2.1: Diagram of a 2 cell thick shell around a circle. The numbers and colors represent different band numbers Ba.

narrow band, a "shell", around the interface. A banded shell of thickness 2 cells around a circle is shown in Fig. 2.1. The numbers at the cell centers, the band number Ba, have the same sign as the level set ϕ and indicate the number of cells to the interface in the cardinal directions. This additional variable is used to gauge the relative closeness of grid nodes to the interface. If a 2D domain has approximately N points in both directions, the number of operations scales as $\mathcal{O}(N^2)$ if all points are considered; if the operations are only performed on a shell, the number of operations scales as $\mathcal{O}(kN)$ where k is the number of bands. Adalsteinsson and Sethian [1] further investigated the efficiency of these narrowband techniques. They observed a memory savings of a factor of 4 and simulation run-time decreases of around a factor of 3 for their narrow band implementation. These savings increase with grid resolution. Although narrow band methods require slightly more programming complexity, the computations can be significantly more efficient.

When the numerical methods of Chap. 3 and 4 are tested, a full band structure of points is considered. A narrow band of approximately 20 cells thick is used for computational efficiency in the examples of Chap. 3 and 4. Chapters 5 and 6 always use narrow band methods. For the narrow bands, the outermost bands have reduced-order finite-difference discretizations in the reinitialization to preserve the hyperbolic nature of Eq. 2.22. Points outside of the narrow bands are assigned

values with the correct sign and a large magnitude. Narrow band methods require the level set reinitialization to initialize these points as the interface moves and points are added to the narrow bands.

2.4.4 Curvature calculation

Since the GFM is a sharp interface technique, the curvature is only calculated for points were $|Ba| = 1$. The interface curvature at a point of interest is calculated from a third-order, least-square polynomial fit (LSQ) of the local level-set field ϕ [91]. This fit is the minimum order necessary to approximate the curvature. Higher order polynomials were found unnecessary. All grid cells used in the fit are equally weighted. In 2D Cartesian coordinates, the nine nearest grid cells (rectangle around a point and itself) are used for fitting the polynomial. If the stencil points are located inside of a wall, the nearest points are offset accordingly. In 3D Cartesian coordinates, the nineteen nearest grid cells are used in the polynomial stencil. This configuration corresponds to a 3 x 3 x 3 cube around the point of interest with the outside corner grid cells removed (Fig. 2.2a). Inclusion of these corners was observed to give rise to unstable, parasitic oscillations. Against the wall, a pyramid shaped stencil (Fig. 2.2b) with the point of interest in the middle of the base was used to have sufficient information. The curvature κ is truncated such that $-1/\Delta x < \kappa < 1/\Delta x$ in Cartesian coordinates. These limits are the minimum/maximum resolved curvatures for the computational mesh.

In axisymmetric cylindrical coordinates, the mean curvature is the sum of the 2D Cartesian curvature κ_1 and the curvature due to the axis of symmetry κ_2,

$$\kappa = \kappa_1 + \kappa_2 \tag{2.23}$$

κ_2 depends on the radial cylindrical coordinate r and can be expressed as

$$\kappa_2 = \frac{1}{r} \frac{\frac{\partial \phi}{\partial r}}{\sqrt{\left(\frac{\partial \phi}{\partial r}\right)^2 + \left(\frac{\partial \phi}{\partial z}\right)^2}} \tag{2.24}$$

Figure 2.2: Cells used in the least square polynomial fit in 3D: a) 19 cells centered on the point of interest (non-wall), b) pyramid shaped collection of cells with the point of interest in the middle of the base (wall).

where z is the axial cylindrical coordinate. This second curvature contribution will be added to the 2D Cartesian curvature for the axisymmetric simulations in Chap. 6.

Although Eq. 1.9 can be used with finite-difference discretizations to calculate the interface curvature κ, the curvature varies more smoothly along the interface for the LSQ routine; the polynomial fit naturally smooths the level set information. Since a linear system of equations is solved to fit the data [56], this extra smoothness comes at the price of slightly increased computational overhead. However, the curvature calculation accounts for a negligible portion of the time involved in each simulation step and, thus, use of the LSQ routine does not significantly alter the simulation speed.

2.5 Summary

The numerical implementation uses second-order finite-difference discretizations of the incompressible Navier-Stokes equations in the NGA framework. The fluid properties and normal stress jump condition are treated using a sharp interface method, the ghost fluid method [73], which has been shown to have smaller parasitic velocity currents than a diffuse interface approach. These spurious fluid velocities would be particularly detrimental in the surface tension dominated fluid flows of the present work. The level set variable ϕ is transported using the Eulerian advection scheme QUICK [86] and the level set reinitialization is the modified Hamilton-Jacobi equation of Hartmann et al. [59]. The interface curvature is calculated using a least-square polynomial fit to ϕ.

Chapter 3

An improved method for level set reinitialization at a contact line [1]

Errors using inadequate data are much less than those using no data at all.

— Charles Babbage

3.1 Introduction

The reinitialization step is examined in this chapter to analyze any artificial, purely numerical effects; the contact line physics are not included in this chapter.[1] The Hamilton-Jacobi equation (Eq. 2.22) is hyperbolic with characteristics normal to the interface $\phi = 0$ (Fig. 3.1). While the reinitialization works well if no contact lines are present, a "blind spot" occurs near contact lines: there is a region where no characteristics exist because any characteristic would originate at the wall (Fig. 3.1). This region will always occur on the obtuse-angle side of the interface, and it vanishes only if the angle at the wall is $\theta = 90^o$ (hereafter this wall portion is referred to as the obtuse side). The mathematical solution for the Hamilton-Jacobi equation is, therefore, ill-posed because it lacks the proper boundary conditions. Depending on the blind spot boundary condition along the wall, a new type of numerical, parasitic current can be introduced due to interface curvature errors. Over time, these currents cause spurious interface evolution.

[1] The information in this chapter has been published in the Journal of Computational Physics [32].

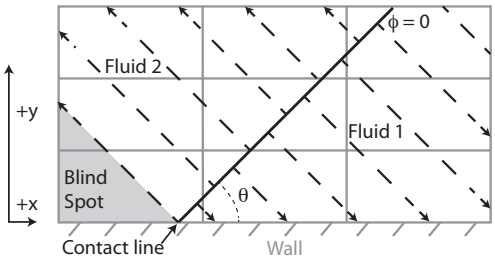

Figure 3.1: Diagram of the blind spot (grey). The black solid line corresponds to the interface $\phi = 0$. The dashed lines are the characteristics for the Hamilton-Jacobi equation which are perpendicular to the interface.

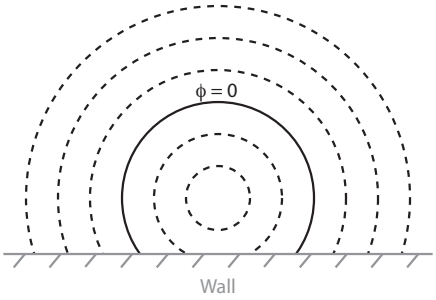

Figure 3.2: Example diagram of the level set isocontours (dashed lines) for a circular droplet on a wall. The black line is the interface $\phi = 0$.

To remedy this interface deformation, most previous studies using the standard level set or conservative level set methods have enforced a contact angle in the blind spot in one of two ways. In some cases, the blind spot contours have a pre-specified contact angle θ [142, 143, 147, 170]. This contact angle (spatially uniform and constant in time) is usually chosen as the static contact angle. In other cases, a dynamic or apparent contact-angle law is used to impose a different isocontour angle value θ at each time step [105, 137, 166, 168]. This angle is spatially uniform in the vicinity of a contact line.

Forcing the angle in these ways has two problems. First, *a priori* knowledge of a dynamic contact angle law is required and, thus, the angle does not arise from physical mechanisms in the simulation. If there were a consensus on a dynamic (or apparent) contact angle law, using such a relation would represent the missing physics and would provide a basis for reinitialization. However, as discussed in Chap. 1, there are numerous theories at this time and their applicability varies. Further, Yokoi

et al. [166] showed a strong dependence of droplet spreading on the applied contact-angle law. They found the correct spreading radius in time only when the contact angle was prescribed by an experimentally-observed relation. Second, using either method, all isocontours in the blind spot have the same contact angle. For a surface of constant curvature, such as a circular droplet (Fig. 3.2), the isocontours have spatially varying angles at the wall. This aspect is not captured by either technique. This forced angle distorts the interface and the curvature distortion leads to parasitic currents.

The goal of this chapter is to develop a reinitialization technique that neither alters nor presupposes the physics of the problem. This study is limited to reinitialization schemes based on the Hamilton-Jacobi equation for a signed distance function. The numerical method should be stable and should not induce changes to the level-set contact angle post-reinitialization. This new routine can be viewed as a necessary step towards a framework for contact-line dynamics where additional physics can be implemented without numerical biasing.

This chapter is organized as follows. Different methods for populating the blind spot with the level set ϕ during reinitialization are discussed in Sec. 3.2. These strategies are demonstrated for test cases of a fluid wedge (Fig. 3.3a) and arc (Fig. 3.3b) trapped between two walls with perfect slip conditions. The effect of blind spot errors are easy to visualize for these cases. A relaxation equation that holds the interface curvature nearly constant is proposed to avoid generating spurious interface deformations in Sec. 3.3. Extensions to this method and limitations are discussed in Sec. 3.4. Finally, Sec. 3.5 and 3.6 show applications of the proposed method. In Sec. 3.5, both 2D and 3D simulations are shown for a gravity-driven droplet sliding on a wall using this relaxation equation. In Sec. 3.6, a block of fluid deforms under gravity and contact lines merge on both the upper and lower walls.

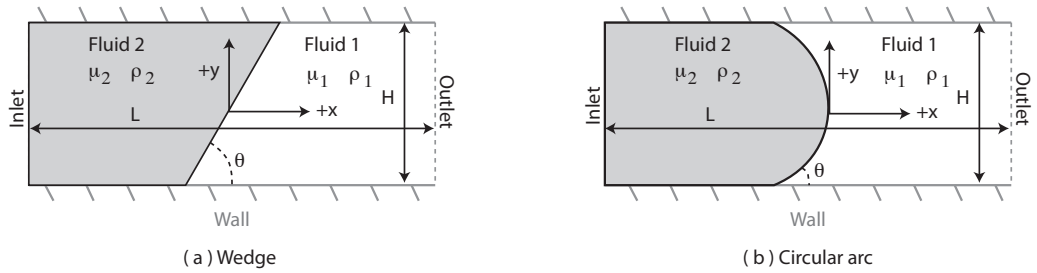

Figure 3.3: Test case geometries for (a) a wedge and (b) a circular arc. The coordinate system is centered in the domain of width L and height H.

3.2 Blind spot methods

This section presents different methods for populating the blind spot. Section 3.2.1 introduces the test cases used to evaluate the different methods. Section 3.2.2 presents a baseline for the error inherent purely to the QUICK transport scheme, i.e., without reinitialization. This case is sufficiently simple that the transport without reinitialization performs well; all subsequent errors are due to the reinitialization. Sections 3.2.3 and 3.2.4 discuss reinitialization methods which either are unstable or significantly distort the fluid interface. These existing methods are presented to contrast with the proposed solution. In Sec. 3.3, a new relaxation equation is coupled to the Hamilton-Jacobi equation, and it is shown to produce minimal interface deformation from reinitialization.

3.2.1 Configuration

Two different test cases are considered. The first case is a wedge of fluid trapped between two walls with an angle $\theta = 45^o$ at the wall (Fig. 3.3a). This case has zero underlying curvature and has both an obtuse and an acute angle for each fluid. The second case replaces the wedge by a circular arc with a contact angle $\theta = 45^o$ (Fig. 3.3b). This scenario corresponds to the constant curvature ($\neq 0$) expected for a fluid droplet at rest. Values of the angle θ other than 45^o have also been tested. Although smaller angles experienced more numerical error for every scheme tested, all the results are qualitatively similar and thus only the 45^o case is shown for clarity.

In both configurations, 2D domains are used to test the blind spot routines. The two walls are separated by a characteristic length scale H. The length of the walls are L= 70 H in the case of no reinitialization (Sec. 3.2.2) and $L = 3\ H$ in all other cases. The inlet (left side) and outlet (right side) boundary conditions are a uniform inlet velocity U and a zero Neumann boundary condition, respectively. The domain is discretized using a uniform grid, $\Delta x = \Delta y = 0.01\ H$. Convergence tests showed this grid to be sufficient for qualitatively non-varying solutions. The time integration was performed with a uniform time step of $\Delta t = 10^{-3}\ \mu H/\sigma$. The reinitialization procedure is applied at every time step. Equation 2.22 is evolved for 600 iterations.

For the present test cases the fluids on either side of the interface are set to the same properties ($\rho_1 = \rho_2,\ \mu_1 = \mu_2$) to isolate the effects of the blind spot. This arbitrary choice limits neither the scope nor the applicability of the present work as the presence of a blind spot is independent of fluid properties. A dimensionless Ohnesorge number $\mathrm{Oh} = \mu/\sqrt{\rho\sigma H}$ of 0.1 is used, which is similar to values used in other studies [142]. Smaller Oh simulations have stronger parasitic currents since the surface tension effects are more dominant. Gravity does not affect the reinitialization and is therefore neglected. For these parameters, there are two relevant time scales in the system: a viscous-capillary and characteristic simulation time scale $\tau_{Ca} = \mu H/\sigma = 1$ and an inertial-capillary time scale $\tau_{We} = \tau_{Ca}/Oh = \sqrt{\rho H^3/\sigma} = 10$. All simulations in this section are performed until $t = 60$, which is at least six times larger than the physical time scales.

To decouple the physics of the contact line from the numerical methods, a full slip boundary condition is used for the velocity along the walls. Under these conditions, the exact solution is a constant interface profile advected at a constant speed U; there should be no interface deformation. The error E_p in the profile shape is reported as the integrated quantity

$$E_p = \int_{-H/2}^{H/2} |x_{int}(y,0) - (x_{int}(y,t) + U \cdot t)| dy\ , \tag{3.1}$$

where x_{int} is the x-coordinate of the interface $\phi = 0$ as a function of time t and vertical distance y. This choice accounts for deformation along the entire fluid interface, and it provides an estimate for the global error. This error may average out local distortions of the interface at the wall. Therefore, the contact angle θ at the bottom wall is also monitored; this angle represents the local numerical error at the contact line. The contact angle is evaluated by fitting the three values of x_{int} closest to the wall with a second-degree polynomial in y, and the angle θ is calculated from the slope of that polynomial at the wall.

An obtuse-side cell indicator is also useful to locate cells along the wall in the blind spot. To identify obtuse-side cells on the wall, the quantity Φ,

$$\Phi = \phi_0 \frac{\partial \phi}{\partial n} , \tag{3.2}$$

is calculated where n is the outward normal direction to the wall. The sign of ϕ_0 is used instead of the sign of ϕ for stability similar to the Hamilton-Jacobi equation (Eq. 2.22). If $\Phi \geq 0$, then the point is on the obtuse side of the interface (blind spot); if $\Phi < 0$, then it is on the acute side.

3.2.2 Transport scheme errors

Pure transport with no reinitialization establishes a baseline for the error due to the transport scheme. Transporting the interface profiles with $Ca = \mu U/\sigma = 1$, the wedge and arc do not change qualitatively in time (Fig. 3.4). Quantitatively, the integrated error E_p is on the order of 10^{-4} for the arc and much smaller for the wedge, on the order of 10^{-7} (Fig. 3.5a). The angle θ at the wall also deviates by less than 1^o so the angle locally at the contact line is maintained (Fig. 3.5b). In summary, the transport alone appears to have negligible effects on the shape of the interface. As a consequence, any future deviations observed with reinitialization can be safely assumed to be the result of the parasitic currents from the contact line. Hence, all further simulations are performed

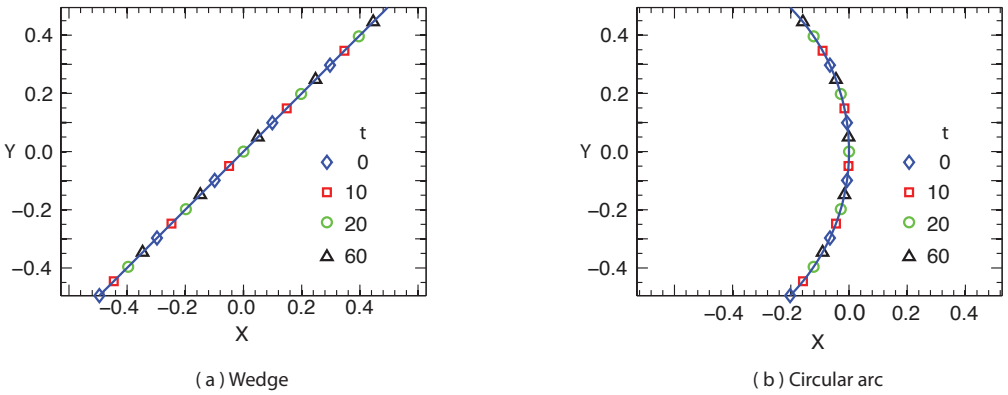

Figure 3.4: Interface profiles with no reinitialization as a function of time, t (pure transport at a constant speed).

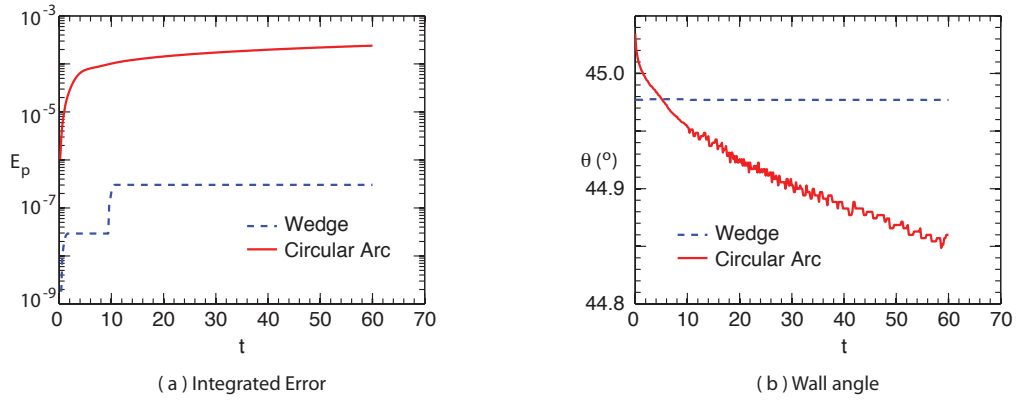

Figure 3.5: Integrated error E_p and angle at the wall θ as functions of time for both the wedge (dashed line) and circular arc (solid line) when the level set function is not reinitialized.

with $U = 0$ and the profiles should always remain stationary. This restriction reduces the computational cost of the simulations and focuses strictly on the reinitialization results.

Although the results above are highly accurate, they do not imply that the reinitialization step can be forgone. In any more general case with a deforming interface, such as droplet impacts, this strategy cannot be used because the level set function ϕ will lose its smoothness. The reinitialization step exists for precisely this reason [102].

3.2.3 WENO stencils with wall ghost values

The first reinitialization schemes considered are based on using ghost cells to complete the near-wall WENO stencils used to evaluate the derivatives in the Hamilton-Jacobi equation. For each direction, the scheme of Jiang and Peng [71] uses a four point derivative stencil biased either in the upwind ($\partial\phi/\partial y^+$) or the downwind ($\partial\phi/\partial y^-$) direction. The stencils are depicted in Fig. 3.6a where the shaded points a and b are inside of the wall. In order to evaluate the derivatives at point c, values of ϕ are needed at points a and b. The schemes below are different methods to populate these ghost cells.

3.2.3.1 Zero Neumann boundary condition

One of the simplest assumptions is that the blind spot has no effect on the evolution of the interface. Under this assumption, the choice of boundary condition for the obtuse points can be arbitrary. One boundary condition to use is a zero Neumann boundary condition,

$$\frac{\partial \phi}{\partial n} = 0 \, . \tag{3.3}$$

To implement this boundary condition, the ghost cells a and b just copy the value of ϕ from point c (Fig. 3.6b). The WENO stencils remain unchanged and use the values stored inside the walls.

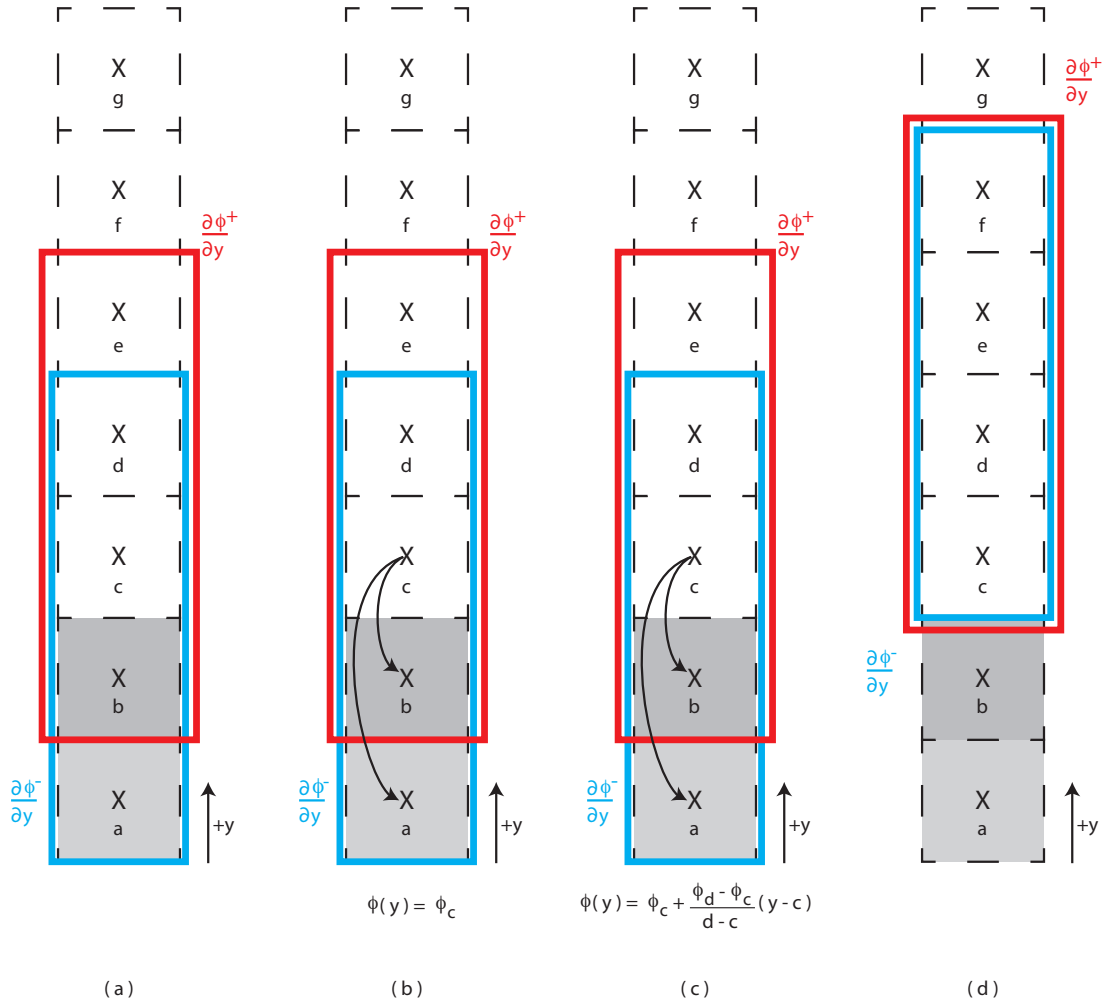

Figure 3.6: Diagram of the finite-difference stencil variations used in the presence of a wall: a) standard WENO stencil points for the upwind $\partial\phi/\partial y^+$ (red) and downwind $\partial\phi/\partial y^-$ (blue) directions, b) zero Neumann boundary condition, c) extrapolation method, d) shifted stencils around point c or d that exclude the wall. The solid line boxes surround the points used in the stencil. The shaded cells a and b are in the wall.

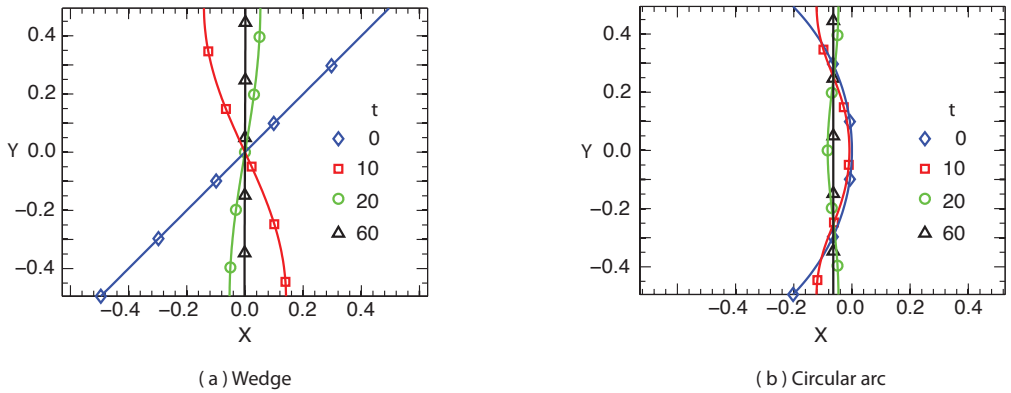

Figure 3.7: Interface profiles when a zero Neumann boundary condition is used.

The evolution of the interface for both test cases is shown in Fig. 3.7. In both cases, there is a systematic evolution from the original angle to the angle for which the zero Neumann boundary condition is correct, $\theta = 90^o$. The angle at the wall almost immediately jumps to $\theta = 90^o$ (Fig. 3.8b). This change occurs after only two calls to the reinitialization function (data points not shown in Fig. 3.8b). These curvature errors at the contact line generate a capillary wave that, in turn, propagates the deformation over the entire profile (Fig. 3.8a). The profile overshoots the flat interface ($t = 10$ in Fig. 3.7a) which causes the oscillations observed in the error E_p. These oscillations occur on a time scale comparable to τ_{We} as expected.

The assumption that the blind spot has no impact on the evolution of the interface is clearly poor because the curvature calculation includes points around the contact line as well as at the interface. While this choice is easy to implement, it suffers from a residual, unphysical forcing at the contact line and subsequent parasitic currents. The blind spot cannot be ignored.

3.2.3.2 Extrapolation

A natural extension of the Neumann scheme discussed in the last section is populating the ghost cells a and b in the wall with second-order extrapolated values (Fig. 3.6c). While this method

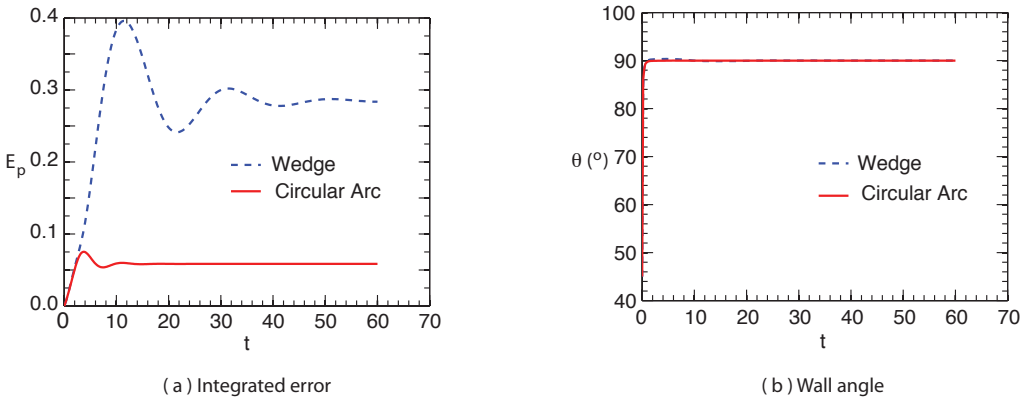

Figure 3.8: Integrated error E_p and angle at the wall θ as functions of time for both the wedge (dashed line) and circular arc (solid line) when a zero Neumann boundary condition is used.

works well for acute points (effectively reducing the derivative order in the vicinity of the walls), it does not work for obtuse points. For the obtuse points, a feedback loop develops where information propagates from points c and d to points a and b by the extrapolation and then back to points c and d using the Hamilton-Jacobi equation. This loop is found to be unstable and was observed to drive θ to 0^o all along the obtuse side.

3.2.3.3 Ghost interfaces

To fix the unstable extrapolation on the obtuse side, Spelt [137] proposed constructing a linear ghost interface from the contact line into the wall. This approach is similar to that of Sussman and Eto [147] except the angle is calculated at the contact line rather than forced to the static contact angle. Only a brief description of the method from Spelt is provided here. The reader is referred to Ref. [137] for more details.

In this method, the contact line points are first located using linear interpolation between grid cells. The angle θ at each point is then calculated using second-order upwind stencils. Given the contact angle θ and the contact point, a planar "ghost interface" can be reconstructed in the wall that satisfies these constraints. Finally, trigonometric relations are used to calculate the distance D_{ghost} to this interface for any point in the wall. Points on the obtuse side ($\Phi \geq 0$) are assigned the

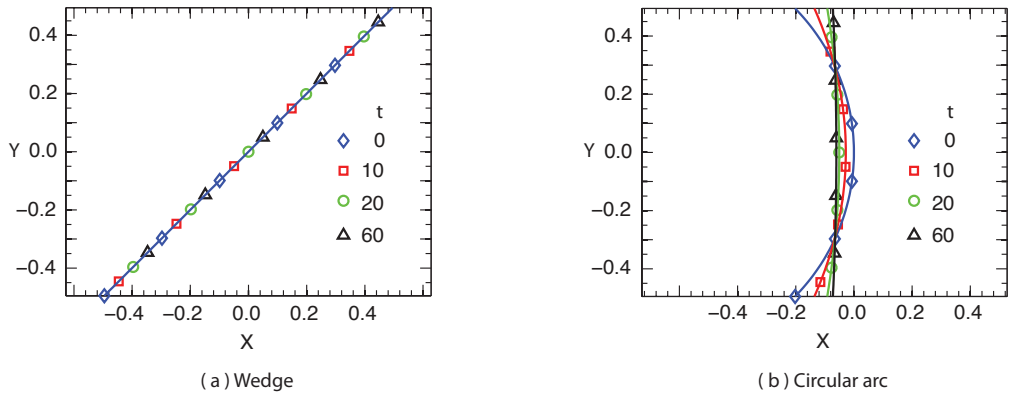

Figure 3.9: Interface profiles when the level set ϕ in the wall is populated using a ghost interface.

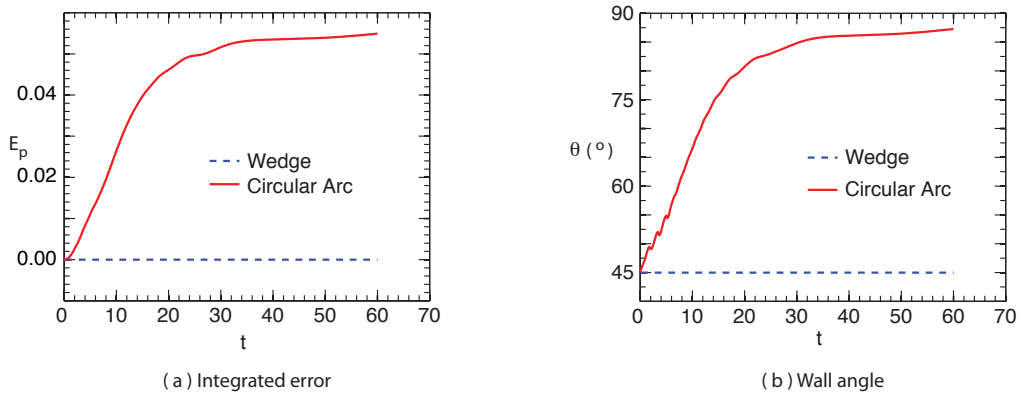

Figure 3.10: Integrated error E_p and angle at the wall θ as functions of time for both the wedge (dashed line) and circular arc (solid line) when the level set ϕ in the wall is populated using a ghost interface.

value D_{ghost}; points on the acute side are assigned the minimum distance

$$\phi = min\left(D_{ghost}, D_{extrap}\right) \ , \tag{3.4}$$

where D_{extrap} is the extrapolated value shown in Fig. 3.6c (Sec. 3.2.3.2). An additional modification was added in this study. It was noticed that since the value of D_{ghost} is independent of the local level set ϕ at the first grid point above the wall, occasionally the ghost cell would change the orientation of the level set: an obtuse cell would be represented as acute or vice versa in the first few

Hamilton-Jacobi iterations. To correct this misrepresentation, an additional check was included for the consistency of D_{ghost} with obtuse and acute points. Without this check, isocontours of ϕ sometimes inverted their contact angles far away from the contact line. If a cell failed the check, D_{ghost} could not be used in the wall and the wall cell was set to either a zero Neumann condition (obtuse) or the extrapolated value D_{extrap} (acute). In all cases by the end of the reinitialization process, no wall cells failed the check; the field satisfied the Hamilton-Jacobi equation with the contact angle θ imposed in the blind spot. Therefore, this additional step does not affect the validity of the final results.

The simulation results are nearly perfect for the wedge, but not for a circular arc. The wedge profile has virtually no spurious currents (machine precision) since the extrapolated and ghost interface values are exact (Fig. 3.9a). The integrated profile error E_p is zero to machine precision (Fig. 3.10a) and the angle at the wall does not change (Fig. 3.10b). This result is not surprising as the method was developed using the assumption of zero curvature (planar ghost interface). For cases with zero curvature, this is the best option in terms of simplicity and accuracy. However, when the interface has an inherent curvature, as in the circular arc case, the profile slowly but consistently relaxes towards a flat interface (Fig. 3.9b). The local angle at the wall θ transitions towards 90^o (Fig. 3.10b).

While the ghost interfaces work well for cases of zero curvature, it produces undesirable deformations for an interface of constant, non-zero curvature. Refined grid simulations did not alleviate this problem. This evolution occurs because a flat interface is the only solution that satisfies a constant interface curvature and a zero curvature condition at the wall (planar ghost interface). Furthermore, this technique is limited to 2D. Extending the technique to 3D would require constructing a general ghost surface and approximating the distance to such an interface. Routines to perform such surface construction are restricted to direct reconstruction techniques, such as the panel approximation technique of Sussman and Dommermuth [144]. These reconstruction techniques are fundamentally different from the Hamilton-Jacobi reinitialization discussed in this work and they tend to be less computationally efficient.

3.2.4 Offset finite-difference stencils

Rather than using ghost cells, an alternative method is to exclude points a and b from the WENO stencils (Fig. 3.6a) by shifting the derivative stencils away from the wall. The weights for each cell are then computed with standard finite differences. The offset stencils for points c and d include the same points (Fig. 3.6d), although the relative weighting of each point is different. For acute cells ($\Phi < 0$), neither stencil is unstable because information is propagating into the wall and the stencil orientation is upwind. However, for obtuse cells next to the wall ($\Phi \geq 0$), while the stencil for point d retains at least one point in the downwind direction, the derivative stencil around point c has no downwind information and will be unstable in a similar way to the extrapolation (Sec. 3.2.3.2).

3.3 Relaxation equation

In order to overcome the inherent difficulties of the previously discussed techniques, a new method is sought for the cells along the wall in the blind spot. If the slope of the isocontours at the wall is maintained during the reinitialization, it is expected that the curvature will also be preserved, minimizing spurious currents. Following this observation, the original Hamilton-Jacobi equation for the first layer of cells along the wall in the blind spot may be replaced by a new equation,

$$\frac{\partial \phi}{\partial \tau} = sgn \cdot \left(\left(\frac{\frac{\partial \phi}{\partial n}}{|\nabla \phi|} \right)_o - \left(\frac{\frac{\partial \phi}{\partial n}}{|\nabla \phi|} \right) \right) , \tag{3.5}$$

where the subscript o indicates the value prior to reinitialization. The value sgn is determined by the wall orientation; $sgn = -1/+1$, if the wall is in the negative / positive direction. The derivative normal to the wall ($\partial\phi/\partial n$) can be discretized using either first-order (points c,d), second-order (points c,d,e), or third-order (points c,d,e,f) finite-difference approximations (Fig. 3.6d). The ratio of $\partial\phi/\partial n$ and $|\nabla\phi|$ is $\cos\theta$. This relaxation equation is intended to keep the angle of the level set at the wall constant throughout the reinitialization. By analytic continuation, the variable ϕ is still

a distance function. Once a cell has been found as on the obtuse side ($\Phi \geq 0$), it always uses the relaxation equation (Eq. 3.5) for the remainder of that reinitialization step.

WENO stencils were used to calculate derivatives in the tangential directions ω since these were already available from the original Hamilton-Jacobi equation. The tangential derivative D_ω is determined by the signs of ϕ_0 and the upwind/downwind derivatives,

$$D_\omega = \begin{cases} \text{if } \phi_0 > 0 & \text{if } \phi_0 < 0 & \\ \hline \frac{\partial \phi}{\partial \omega}^+ & \frac{\partial \phi}{\partial \omega}^- & \text{if } \frac{\partial \phi}{\partial \omega}^+, \frac{\partial \phi}{\partial \omega}^- > 0 \\ \frac{\partial \phi}{\partial \omega}^- & \frac{\partial \phi}{\partial \omega}^+ & \text{if } \frac{\partial \phi}{\partial \omega}^+, \frac{\partial \phi}{\partial \omega}^- < 0 \\ m\left(\frac{\partial \phi}{\partial \omega}^+, \frac{\partial \phi}{\partial \omega}^-\right) & & \text{otherwise} \end{cases} \tag{3.6}$$

where $m(a, b)$ returns the derivative with the smaller absolute value. The resulting tangential derivative is biased in the interface direction. This orientation of the tangential derivatives along the wall in the relaxation equation was necessary for stability reasons. Otherwise, two adjacent cells might have overlapping tangential derivative stencils which can result in a feedback loop. This choice is similar to the maximum and minimum statements in the treatment of the WENO stencils from Jiang and Peng [71].

The wedge and arc test cases are shown in Fig. 3.11 when the relaxation equation is used. Similar to the ghost interfaces (Sec. 3.2.3.3), the wedge is virtually perfect: E_p is machine precision and θ does not change from its initial value. However, for the arc, the relaxation equation induces errors of $E_p \sim 10^{-3}$ that are at least an order of magnitude smaller than the other methods we considered ($E_p > 0.01$). Interestingly, the integrated error (E_p) decreases with the finite-difference order, whereas the contact angle θ has little variation in all cases. While the higher-order finite differences exhibit smaller integrated errors, it is difficult to justify their use instead of first-order

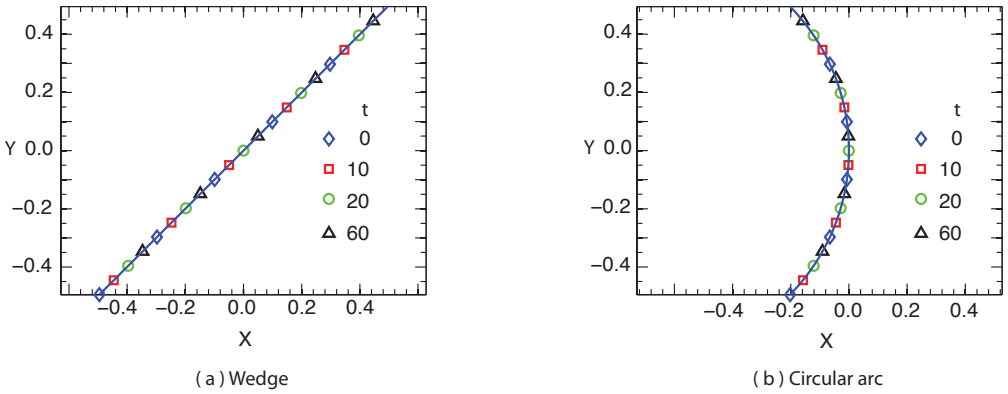

Figure 3.11: Interface profiles when the relaxation equation is used for cells on the wall in the blind spot.

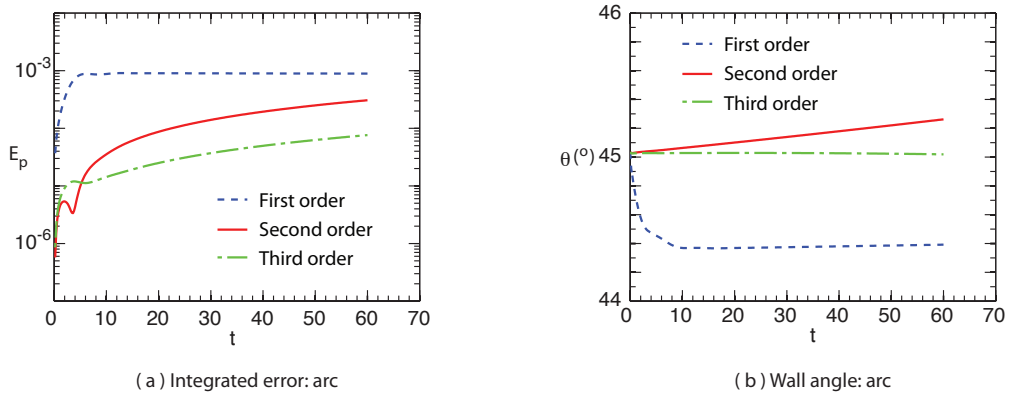

Figure 3.12: Integrated error E_p and angle at the wall θ as functions of time for the circular arc when the relaxation equation is used for cells on the wall in the blind spot. The different curves are first-order (blue), second-order (red), and third-order (green) discretizations of the normal derivative $(\partial\phi/\partial n)$. The y-axis in (a) is logarithmic.

finite differences for these cases because these errors are smaller than that of the transport scheme (Fig. 3.5). Additionally, first-order finite differences are more compact and less prone to error propagation. The higher-order finite differences with their smaller errors, however, were found more accurate for more complicated configurations. In all subsequent studies of this chapter, first-order finite differences were used, but third-order finite differences were used for Chap. 4–6.

To further underscore the benefit of using the proposed relaxation equation and demonstrate its effects on a non-perfect signed-distance function, another series simulations were performed for a circular drop trapped between two walls with the same contact angle and domain dimensions. This initial condition is the next worse scenario for the input to the reinitialization routine. In one case, the initial distance function was scaled by a factor of 1/2 (Fig. 3.13a) and in the other by a factor of 2 (Fig. 3.13b). The reinitialization routine was applied for 1,000 iterations. All of the angles at the wall are initially correct, but ϕ is not a distance function, i.e., $|\nabla\phi| \neq 1$. It is important to note that such a perturbation of the level set function is quite extreme and is rarely encountered in practice. The simulation results show that the level set function in the vicinity of the interface is converged within 500 iterations. While perfect concentric circles are expected, the half-scaled function shows some differences near the middle of the circle. These differences come from the slow convergence of the relaxation equation in this region of small initial angles (see next section). While these contours are clearly distorted, the important isocontours near the interface are still captured and the interface curvature of the zero level set is maintained. If the level set is only stored locally around the interface (narrow bands) [26], this distortion may not even exist.

3.4 Method extensions and limitations

The test cases of the wedge and circular arc considered are “worst case scenarios” as implemented. These simulations have minimal resistance to curvature errors because of the full slip boundary condition. The interface easily deforms and without additional physics, there is no driving force to

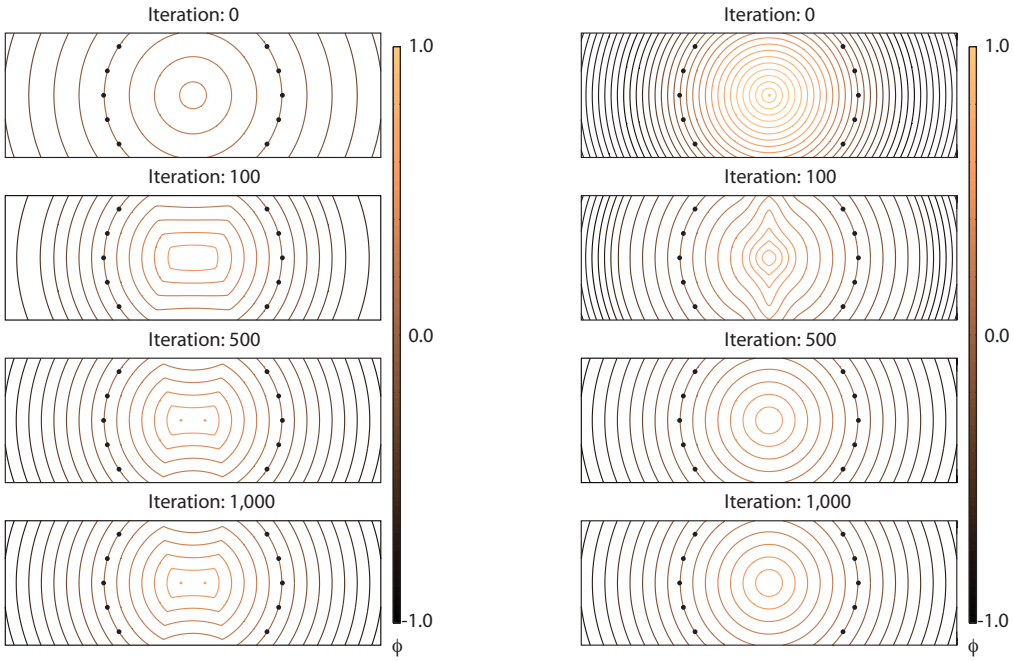

Figure 3.13: Isocontours for concentric circles during reinitialization for an incorrectly scaled distance function by a factor of a) 1/2 and b) 2. Neighboring isocontours differ by $\Delta\phi = 0.1$. The black circular dots indicate the zero level set.

return it to its original shape. Since the current framework does not include any physical terms, there is no single equilibrium shape. Rather, there is a family of arcs satisfying the Laplace condition (Eq. 2.17). If a contact angle was imposed as in previous studies, a single arc would be the equilibrium solution and the reinitialization would keep the contact angle.

The relaxation method is still compatible with imposing a dynamic (or apparent) contact-angle law. More precisely, the relaxation equation would be simply replaced by

$$\frac{\partial \phi}{\partial \tau} = sgn \cdot \left(cos\left(\theta_D\right) - \left(\frac{\frac{\partial \phi}{\partial n}}{|\nabla \phi|} \right) \right) \ . \tag{3.7}$$

In this scenario, it is necessary to reinitialize at every time step to ensure that the correct angle is present at the wall. Often with level-set methods, the reinitialization frequency is set to be less seldom than every time step for various reasons. This reinitialization restriction is a major disadvantage. Using the relaxation equation, the wall angle can be left freely floating and determined by the simulation physics. This approach requires neither an *a priori* contact-angle law nor reinitialization at every time step. The author is unaware of any other reinitialization technique that can have an accurate, unrestricted angle.

The main disadvantage to using the relaxation equation is that it converges very slowly for small angles ($\theta \rightarrow 0^o$, $|\partial\phi/\partial n| \rightarrow 1$). To see this result, the derivatives in the relaxation equation (Eq. 3.5) are first replaced by their trigonometric counterparts

$$\frac{\partial \phi}{\partial \tau} = sgn \cdot \left(cos\left(\theta_o\right) - cos\left(\theta\right) \right) \ , \tag{3.8}$$

where θ_o is the original and θ the current contact angles. Using Taylor series expansions for the cosine and only keeping the lowest order term,

$$\frac{\partial \phi}{\partial \tau} \sim sin\left(\theta_o\right)\left(\theta - \theta_o\right) \ . \tag{3.9}$$

The magnitude of the change for any given step of the equation scales roughly as the sine of the original angle. For the off-scaled distance functions (Fig. 3.13), the convergence difference between the half-scaled function and doubled function can be seen at iteration 100. The isocontours for the doubled function are nearly vertical in the center of the drop and thus $\theta - \theta_0$ is large. However, for the half-scaled function, the isocontours in the middle are flatter, thus $\theta - \theta_0$ is small and the convergence is poor. Care needs to be taken for simulations with small angles.

To treat small contact angles, there are a few possible approaches. The first option is to include a multiplier on the right hand side of Eq. 3.5. This number should grow as $\sin(\theta_0)$ and $(\theta - \theta_0)$ approach 0 to increase the rate of convergence. This approach, however, can have poor numerical stability and may need to be treated implicitly. A second option is to disregard the relaxation equation, but use its central idea of conserving the angle with a non-iterative approach such as the FMM (Eq. 1.11). This formulation is a single mathematical calculation. The relaxation-equation equivalent for the blind spot in the FMM is

$$|\nabla_s \phi|^2 = \frac{1}{sin(\theta_0)^2} \ . \tag{3.10}$$

where ∇_s is the surface gradient operator along the wall. The major disadvantage to this approach is that FMM methods are typically low-order and, therefore, the accuracy of the interface curvature suffers. The last option is the simplest. If the interface itself is not at the extreme contact angles, the locations where $\theta_0 = 0^o$ or 180^o are far from the interface. Therefore, the angle can be limited in these regions to a minimum θ_{min} and maximum angle θ_{max},

$$\theta_0 = min\left(\theta_{max}, max\left(\theta_{min}, \theta_0\right)\right) \ . \tag{3.11}$$

While this algorithm is extremely easy to implement, it places practical limitations on the angles that can be captured by the simulation. Throughout Chap. 5 and 6, angles limits of $\theta_{min} = 10^o$ and $\theta_{max} = 170^o$ were found sufficient for convergence.

3.5 Example 1: sliding droplets

In the previous section, the relaxation equation was found to introduce much smaller parasitic currents than any other method and any numerically-induced deformations remained extremely small. In this section, the physical deformation of sliding, gravity-driven droplets on a wall is investigated. These droplets are expected to deform into an aerodynamic, bulb-like shape. The simulations show that the relaxation equation captures varying contact angles and can be easily used in 3D.

3.5.1 Configuration

The domain used for the droplet simulations (2D and 3D) is shown in Fig. 3.14. The droplet has diameter D and is initially located at $x_{center} = 2.5\ D$. The length of the domain in the direction of flow is $L = 8\ D$ while the direction normal to the wall is $H = D$. The z-dimension, when applicable, has a width of $W = 2\ D$. A uniform grid of cubic cells $\Delta x = \Delta y = \Delta z = 0.02\ D$ is used. The z-direction is periodic while the x- and y-directions are bounded by walls. On the walls, a full slip condition is again used to generate maximum droplet deformation in the absence of a physical driving force to a static contact angle. A gravity vector with magnitude g is oriented in the positive x-direction.

This configuration is exactly like a symmetric droplet falling under gravity (no walls) subject to one caveat: leading and trailing angles do not have to be $\theta = 90^o$. The contact angle θ of the initial droplet is set as 90^o such that the simulated droplet on the wall can be compared to its free-fall, full droplet counterpart. For the free-fall droplet simulation, the domain is extended symmetrically in the y-direction an equal amount below the symmetry plane.

In order for the droplet to be gravity-driven and have an aerodynamic shape, a non-unity density ratio $\rho_2/\rho_1 \neq 1$ is required. For these test cases, the density ratio is $\rho_2/\rho_1 = 1/1000$, which corresponds to the density ratio for air and water. The viscosity ratio is still unity, $\mu_1 = \mu_2$. While the

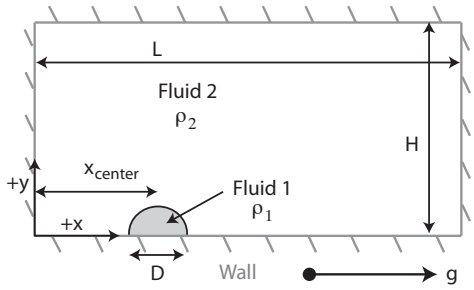

Figure 3.14: Diagram of the 2D and 3D computational domain and initial condition for the droplet on a wall simulations (not drawn to scale). The initial contact angle is 90^o. Gravity is oriented parallel to the wall.

viscosity ratio of air and water could be used, the drop would not experience as much shear-induced deformation and thus the unity viscosity ratio is used to enhance the droplet deformation. The Ohnesorge number is Oh $= \mu/\sqrt{\rho_1 \sigma D} = 0.001$: this value is appropriate for a small water droplet. The gravity vector is oriented in the negative x-direction with a magnitude such that the Bond number Bo $= \rho_1 D^2 g/\sigma$ is 10. A time step of $\Delta t = \sqrt{0.001}\ \mu D/\sigma$ was used which corresponds to a viscous CFL number of approximately 0.3. The reinitialization procedure is applied at every time step and is iterated until either 100 iterations or a maximum relative change $\Delta\phi$ of 10^{-4} between iterations is reached. A minimum of 30 iterations were required to ensure that the information would have sufficient time to propagate away from the interface. It is important to note that $\Delta\phi$ is always small for small angles; regardless of angle, the simulations required between 30 and 60 iterations to reach the end criterion.

3.5.2 Evolution of a 2D gravity-driven droplet on a wall

Different interface shapes for both a droplet sliding on the slip wall (solid line) and a droplet in free fall (dashed line) are shown in Fig. 3.15. The images are offset in space for easy visualization, but the relative position of the dashed and solid lines at a given time are correct. The results shown are phenomenological only; there is no exact analytic result to compare to quantitatively as long as the additional contact-line physics are excluded. While the droplets start off identical, gravity turns the droplet on a wall into a bulb-like shape with fluid accumulation in the positive x-direction as

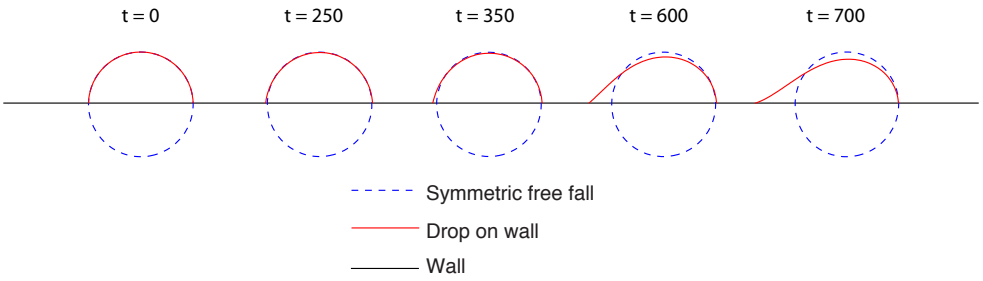

Figure 3.15: Deformation of a two dimensional semicircle and full droplet under gravity. The red line is the interface for a droplet on a wall (black line) and the blue dashed line is a full droplet in free fall.

expected. This asymmetric shape has a non-90^o contact angle at the trailing edge, while the drop in free fall remains nearly circular (as if the contact angle was 90^o). The difference in evolution comes from the high surface tension that preserves the shape of the free falling drop. On the other hand, the sliding drop has no corresponding curvature at the tail, and the final shape (at t = 700) even shows a slightly inverted curvature at the back of the droplet. The non-90^o contact angle could not be captured using another blind spot technique.

3.5.3 Evolution of a 3D gravity-driven droplet on a Wall

The droplet on the wall is repeated in 3D (Fig. 3.16). This extension to 3D is unique to the relaxation equation. The initially hemispherical drop deforms into a tear-drop shape with fluid again accumulating in the direction of gravity. The x-y profile of the droplet and the contact line on the wall are shown in Figs. 3.17a and 3.17b where the different times are offset to intersect at the leading edge. The x-y profile is qualitatively very similar to the 2D simulations as expected (Fig. 3.15), but will not be quantitatively the same because of the additional curvature in the y-z plane. The contact line on the wall also takes on a bulb-like shape that tapers to a point. The contact angle continuously varies along this contour.

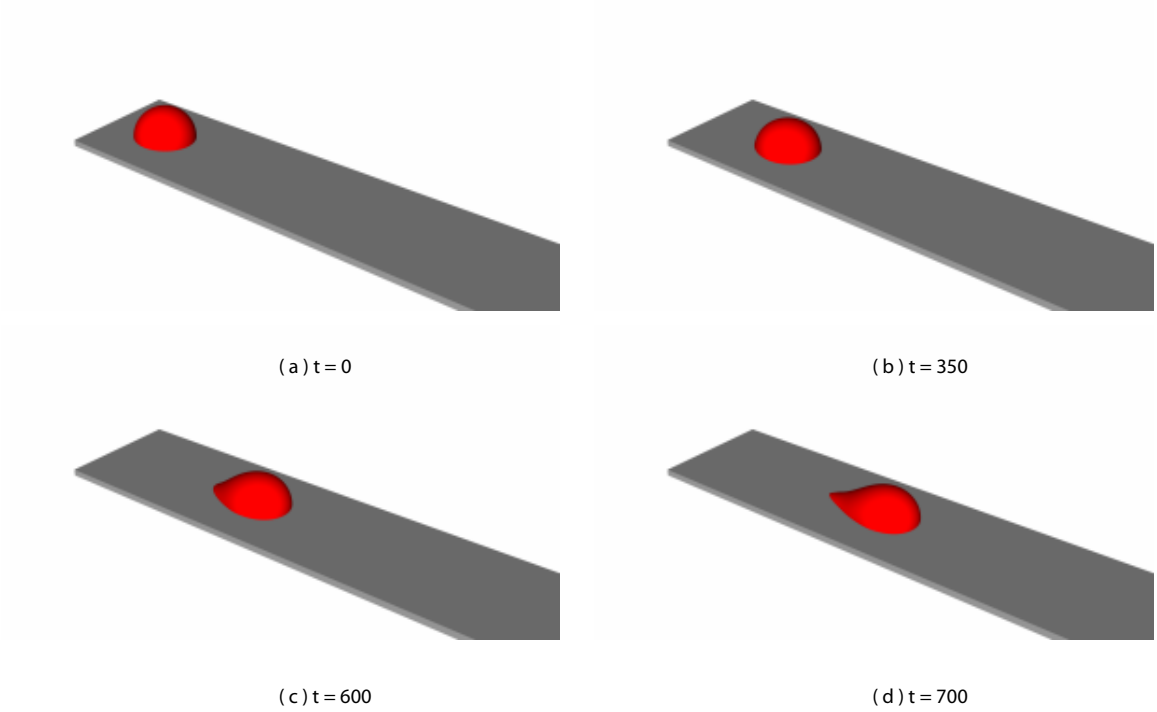

Figure 3.16: Deformation of the hemispherical droplet sliding under gravity.

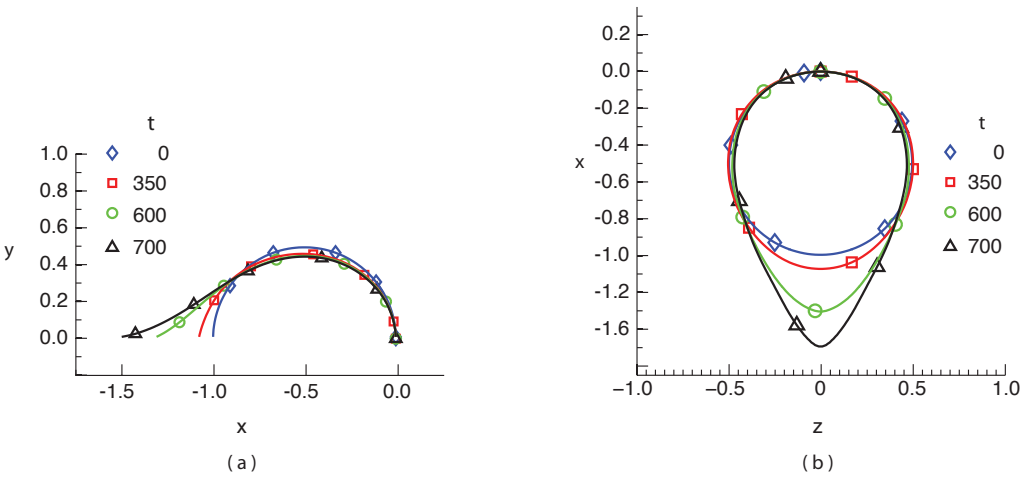

Figure 3.17: a) x-y profile and b) Droplet contact line for a 3D droplet. The profiles are overlaid to intersect at the leading edge.

3.6 Example 2: wedge of fluid

As mentioned in the Chap. 1, the level set method is often used for its natural handling of topological interfaces. In this section, the relaxation equation approach is shown for a 2D case where the contact lines merge along a wall. The fluid spreading is driven by a gravity vector $\vec{g}$ oriented perpendicular to the wall.

3.6.1 Configuration

The domain used is shown in Fig. 3.18. Two walls are spaced a distance H apart. The length of the domain in the x-direction is $L = 4\ H$. The initial condition is a trapezoid of fluid 1 centered in the domain with a base width $W = 2\ H$ and an obtuse trapezoidal angle of $\theta = 120^o$. A trapezoid was chosen because it has non-90^o contact angles. In addition, this initial condition promotes a smooth detachment from the upper wall as opposed to the capillary breakup of the thin fluid thread that forms. A uniform grid of square cells $\Delta x = \Delta y = 0.01\ H$ is used. The x-direction is periodic.

Similar to Sec. 3.5, a full slip velocity boundary condition is used along the walls. The density ratio is $\rho_2/\rho_1 = 1/1000$, and the viscosity ratio is unity, $\mu_1 = \mu_2$. The Ohnesorge number is Oh $= \mu/\sqrt{\rho_1 \sigma H} = 0.001$, and the Bond number Bo $= \rho_1 H^2 g/\sigma$ is 10. A time step of $\Delta t = \mu H/\sigma$ was used which corresponds to a capillary CFL number of ~ 0.5 using the criterion of Eq. 2.21. The reinitialization procedure is applied at every time step for a minimum of 30 iterations and ends when either 300 iterations or a maximum relative change $\Delta\phi$ of 10^{-4} between successive iterations is reached.

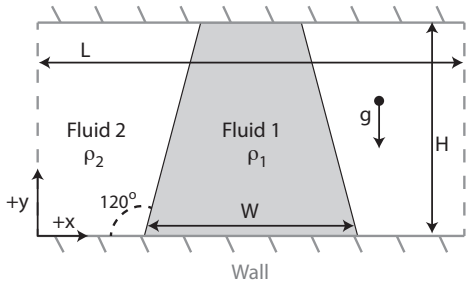

Figure 3.18: Diagram of the computational domain and initial conditions for the simulation with merging contact lines (not drawn to scale). Gravity is oriented perpendicular to the walls.

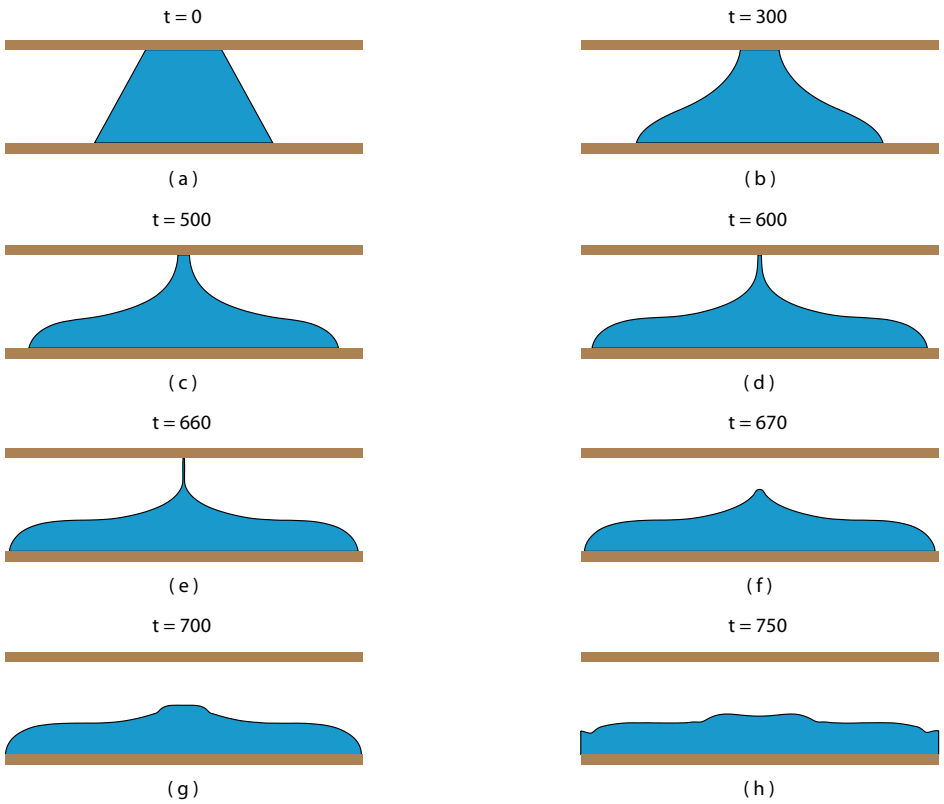

Figure 3.19: Time images of the spreading trapezoidal fluid block (blue) trapped between two walls (brown).

3.6.2 Evolution of a fluid wedge

The evolution of the trapezoidal block of fluid is shown in Fig. 3.19. Since the initial configuration (Fig. 3.19a) has straight sides, there is no capillary pressure jump across the interface and the motion is purely due to the gravitational forces. As fluid drains from the top of the block (Figs. 3.19b–d), the induced interface curvature provides a capillary pressure gradient against the gravitationally-induced spreading. However, due to the large Bond number the fluid still continues to drain. Eventually, a thin fluid filament is formed which detaches suddenly from the upper wall (Figs. 3.19e and 3.19f). The fluid continues to spread along the bottom wall until the edges merge due to the periodicity of the domain (Figs. 3.19g and 3.19h). At this point, standard level-set reinitialization routines can be used since there is no longer any contact line. The proposed method smoothly captures the motion of the interfaces and the merging of contact lines. The fundamental benefit of the level set method to handle changing topologies is not altered by the relaxation equation.

3.7 Summary

A new reinitialization technique, the relaxation equation, was proposed for the blind spot at contact lines. This routine fixes the level set isocontour angles in the blind spot during reinitialization to preserve the second derivative of the level set ϕ along the wall. The relaxation equation does not presuppose any physics and has minimal parasitic velocity currents. For the case of a circular arc, it was the only technique shown that did not flatten the interface. This technique, however, showed lower convergence for shallow angles ($< 10^o$) when $|\nabla\phi| < 1$. These angles may require either an angle limit or the use of a pseudo-time independent equation such as Eq. 3.10. As currently implemented, the relaxation equation (Eq. 3.5) is also limited by the accuracy of the angle calculated θ_o: this issue will be addressed in the next chapter. The routine presented in this chapter is the first of its kind that holds the curvature in the blind spot constant and allows freely floating interface angles.

Chapter 4

Extension velocities and angle propagation

The function of a scientist is to find the point of view from which the subject appears in its greatest simplicity.

— Josiah Gibbs

4.1 Introduction

While the relaxation equation was shown to work well, it is fundamentally limited by the knowledge of θ_o (Eq. 3.8); it does not introduce additional spurious currents, but it cannot correct a non-smooth, non-distance level set ϕ. This issue is particularly problematic if a local minimum in $|\phi|$ occurs in the blind spot. In addition, non-slip wall velocity boundary conditions would naturally distort the angle along the wall due to velocity gradients. The value of θ_o from the existing level set field may be non-ideal.

Some authors have tried different methods to exclude the blind spot. There are two alternative techniques which may not experience the problem of inaccurate curvature at the contact line. One option is to decouple the curvature at the contact line from the level set. In this way, the blind spot boundary condition has less of an effect on the solution. In a recent work, Sato and Ničeno [119] used this approach with the curvature methods outlined in Brackbill et al. [19]. In another study,

Deganello et al. applied a curvature at the wall not calculated from the level set, but derived instead from a physical law [31]. Both of these options require *a priori* knowledge of a forcing law. Furthermore, ϕ can be advected out of the blind spot, corrupting the solution elsewhere. Another option is fitting the interface with a basis function series. These basis functions are then used to populate the blind spot [87] or calculate the curvature [160]. This approach should work well as long as the choice of fitted function is appropriate. However, it is unclear how to choose appropriate fitting functions, particularly in 3D where the surfaces may not be ellipsoids. Sussman and Dommermuth [144] used a direct panel approximation to fit the interface shape. This approach can be exact, but it is computationally more expensive than an ordinary differential equation reinitialization.

A more basic question is whether it is possible to modify the advection equation (Eq. 1.10) such that after transport, the level set ϕ is still a signed distance function. This simple approach would reduce the necessary reinitialization frequency and, in the most extreme case, remove that step entirely. Such an advection scheme has three major benefits: mass loss due to reinitialization is reduced, fewer parasitic velocity currents are introduced at the contact line, and simulations are less computationally expensive because reinitialization is a time-intensive routine. Examining a general advection equation,

$$\frac{\partial \phi}{\partial t} + \hat{u} \cdot \nabla \phi = 0 \,, \tag{4.1}$$

the velocity $\hat{u}$ does not necessarily have to be the local fluid velocity $\vec{u}$. Rather, it must only be a velocity field such that the zero level set (fluid interface) is transported correctly in a Lagrangian fashion. A natural question is if there exists a velocity field $\hat{u}$ that 1) transports the fluid interface with the fluid velocity $\vec{u}$ and 2) maintains ϕ as a signed distance function. As derived by Zhao et al. in the appendix of Ref. [171], the velocity field that satisfies these conditions is the extension velocity u_n,

$$\hat{u} = (\vec{u} \cdot \hat{n})_{\vec{x}=P} \, \hat{n} = u_n \hat{n} \,, \tag{4.2}$$

where $\vec{u} \cdot \hat{n}$ is evaluated at the interface point P closest to the Eulerian grid node. This condition

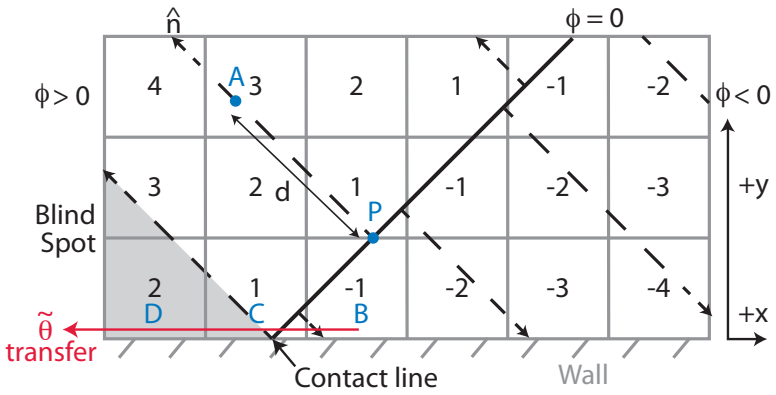

Figure 4.1: Domain diagram around a contact line. The shaded region is the blind spot where no characteristics (dashed lines) exist to trace the value of u_n. A, B, C, D, and P are points referenced in the text. Numbers correspond to the band value Ba at the cell centers. The red arrow indicates the direction of the propagated angle $\tilde{\theta}$ (Sec. 4.2.2.2).

corresponds to enforcing a constant velocity along characteristics normal to the fluid interface and zero velocity across the characteristic. For example, in Fig. 4.1, the extension velocity u_n at point A is the value of $\vec{u} \cdot \hat{n}$ evaluated at point P. An alternative statement is that the extension velocity must satisfy the equation

$$\nabla u_n \cdot \nabla \phi = 0 \tag{4.3}$$

throughout the domain. Using extension velocities, the fluid advection equation (Eq. 4.1) becomes

$$\frac{\partial \phi}{\partial t} = -u_n |\nabla \phi| \, . \tag{4.4}$$

The construction of extension velocities is very similar to the reinitialization step both in implementation and computational cost. In particular, a blind spot still exists near contact lines where there are no characteristics from the fluid interface (Fig. 4.1).

The goal of this chapter is to construct extension velocities u_n in the blind spot while maintaining the integrity of the level set ϕ. These extension velocities should reduce the necessity of reinitialization and would supplement the technique developed in Chap. 3. Section 4.2 briefly describes the existing extension velocity method employed outside of the blind spot and the proposed blind spot

extension velocity routine. The central concepts are fixing the tangential wall velocity and propagating the applied contact angle $\tilde{\theta}$. Section 4.3 reintroduces the circular arc test from Sec. 3.2.1 and evaluates the spurious velocity currents for this test case. An example is then shown for a pinned droplet deforming under gravity in Sec. 4.4. This test case has contact angle deformation. While all the equations of the present work are derived in 2D, the extension to 3D is straight forward and described in Sec. 4.5. This section also discusses the limitations of this approach. Although this chapter explores a new advection scheme, it is found in Sec. 4.6 that the central concept of propagating the contact angle $\tilde{\theta}$ alone is necessary when applied to the QUICK/HCR2/relaxation formulation of Chap. 3. This new relaxation equation reinitialization with QUICK is used throughout the Chap. 5 and 6.

4.2 Construction of extension velocities

4.2.1 Implementation outside of the blind spot

In order to use Eq. 4.4, the extension velocities u_n and gradient $\nabla\phi$ must be constructed at each grid point. A domain diagram near a contact line is shown in Fig. 4.1. The construction of extension velocities outside of the blind spot closely follows the FMM procedure of Adalsteinsson and Sethian [2]. The FMM is used because it is very computationally efficient.

A brief description of the FMM is given below; for a complete description see the review article by Sethian [124]. The FMM solves Eq. 4.3 for each node in the domain in a progressive, point-wise manner. The steps are:

Step 1: Points immediately next to the interface are initialized with their correct values u_n and labeled as "accepted." In general, accepted points are any points that have had their extension velocity u_n evaluated. These initial seed points can be initialized in many ways and are similar to a boundary condition for the FMM.

Step 2: All non-accepted points that border accepted points are labeled "neighbor." The neighbor points are arranged in a heap structure by their interfacial distance. The point at the top of the heap is always the closest of the neighbor points to the interface and has sufficient accepted neighbors to calculate its extension velocity u_n.

Step 3: The extension velocity for the top point is calculated from the linear algebraic equation that results from first-order finite-difference discretizations in Eq. 4.3 using the accepted neighbors and level set information. The top point is removed from the heap and changed to accepted.

Step 4: All of the new accepted point's non-accepted neighbors are added to the heap.

Step 5: Return to *Step 3*.

This process repeats until all points have extension velocities. The extension velocities can be evaluated in this way because a given location's extension velocity is only calculated when there is sufficient information around it. An example of accepted, neighbor, and far away points is shown in Fig. 4.2a.

There are two crucial differences between the routine in Ref. [2] and the present work. First, the initial accepted points where $|Ba| = 1$ (the points closest to the interface) use a different calculation to determine the extension velocity u_n. For these points, the nearest interface point $\tilde{x}$ is first determined from

$$\tilde{x}_i = x_i - d \cdot \hat{n}_i = x_i - \frac{\phi}{|\nabla\phi|^2}\frac{\partial\phi}{\partial x_i} \,, \tag{4.5}$$

where the subscript i denotes directional components (Fig. 4.2b). d is the approximate distance to the interface calculated using the signed, approximate distance function ϕ. The gradient components $\partial\phi/\partial x_i$ are calculated using a least square, quadratic polynomial curve fit, similar to that

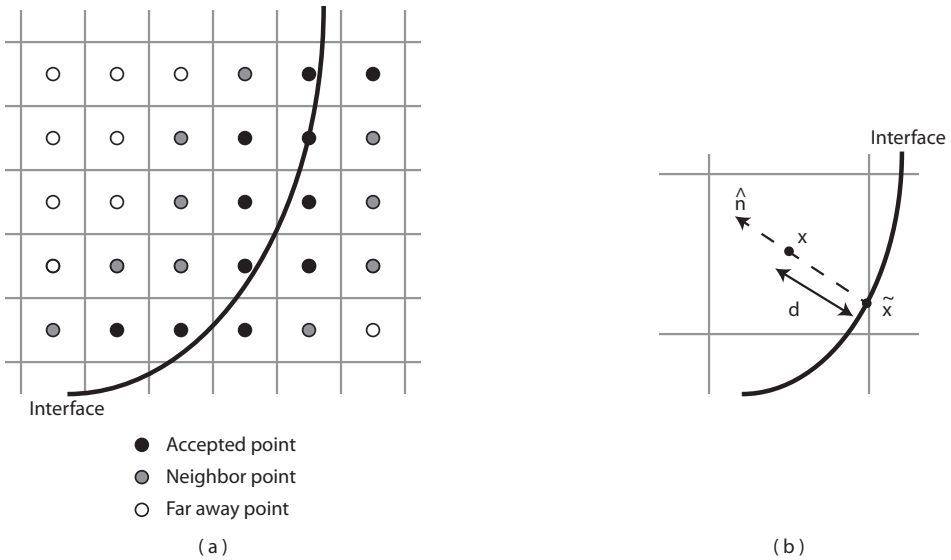

Figure 4.2: a) Example diagram for the FMM. Accepted, neighboring, and far points are black, grey, and white respectively. b) Diagram for computing the nearest interface point $\tilde{x}$.

for curvature [32]. Hereafter, these normals are referred to as "LSQ normals" as opposed to the normal components calculated by first-order finite differences. Then, linear interpolation is used to calculate the velocity components at $\tilde{x}$ ($u_i(\tilde{x})$) and the extension velocity $u_n(\vec{x})$ is calculated as

$$u_n(\vec{x}) = \vec{u}(\tilde{x}) \cdot \hat{n}(\vec{x}) \; . \tag{4.6}$$

The second difference is that while in [2], a temporary, reinitialized level set variable ϕ_{temp} was calculated for the evaluation of $\nabla\phi$ in Eq. 4.3, no such variable can be readily calculated here due to the blind spot effects on the reinitialization. As such, the level set ϕ is always used for $\nabla\phi$. The level set is never reinitialized for Sec. 4.3 and Sec. 4.4. This restriction leads to drastic consequences if a local minimum in $|\phi|$ occurs away from the interface; points could be mistakenly chosen as the next point in the heapsort algorithm of the FMM and the first-order finite-difference stencils for $\nabla\phi$ could overlap. To solve the heapsort problem, the points with the smallest $|Ba|$ are always at the top of the heap and the ordering within these points is by the smallest $|\phi|$. The second problem is mitigated by derivative limiters; the first-order finite-difference gradients are checked to ensure that the gradient implies accepted points are closer to the interface. For example, if $\phi > 0$ at a point

(i, j) and point $(i+1, j)$ is accepted, the derivative in the x-direction is

$$\frac{\partial \phi}{\partial x} = min\left(0, \frac{\phi(i+1,j) - \phi(i,j)}{x(i+1) - x(i)}\right) \tag{4.7}$$

For a perfect signed distance function ϕ, these limiters would never be applied.

4.2.2 Implementation in the blind spot

4.2.2.1 Fast Marching Method (FMM) in the blind spot

For points such as C and D near the blind spot of Fig. 4.1, a different routine must be applied to calculate u_n. Points not directly against the wall can use Eq. 4.3 since u_n should be specified for its nearest accepted neighbors in the FMM. The problem is, therefore, reduced to specifying u_n only for points along the wall in the blind spot. These points are identified in the algorithm as points that are against the wall, but which do not have an accepted neighbor normal to the wall when they are at the top of the heap.

The following condition is proposed for wall points in the blind spot: the component of the extension velocity vector tangential to the wall, u_{tan}, is kept constant. This choice is consistent with uniform translation along the wall. Instead of Eq. 4.3 in the FMM, the 2D equation for this condition is

$$u_n(\vec{x}) sin\left(\theta(\vec{x})\right) = u_{tan} = u_n(\vec{x}_1) sin\left(\theta(\vec{x}_1)\right) \tag{4.8}$$

where $\vec{x}$ is the target point, $\vec{x}_1$ is its accepted neighbor, and θ is the local angle of the ϕ isocontours. For points with $|Ba| = 1$ such as point C, the interface location $\vec{x}_1$ is interpolated between points B and C; both the normal velocity u_n and the isocontour angle θ in Eq. 4.8 are then calculated at $\vec{x}_1$ using the LSQ normals. For points $\vec{x}$ with $|Ba| > 1$, the angle θ could be computed using finite differences from the underlying level set ϕ. This approach, however, was found to be unstable due to a negative feedback loop. For example, the angle θ at point D in Fig. 4.1 is determined (among other things) by the value of ϕ in the cell above it (point E). The evolution of ϕ at that point, in

turn, is determined by the value of u_n at point D. A feedback loop was observed which created a checkerboard pattern in the contact angle θ after several transport iterations.

4.2.2.2 Propagation of isocontour angle $\tilde{\theta}$

In order to remove the previously-mentioned feedback loop and stabilize the isocontour angle, the angle θ used at each grid node is defined by propagating θ along the wall in the blind spot. For clarity, the propagated angles are denoted by $\tilde{\theta}$. In Fig. 4.1, the direction of $\tilde{\theta}$ transfer is indicated by the red arrow along the wall. For $|Ba| = 1$, $\tilde{\theta}$ is calculated from the LSQ normals and then for higher bands, $\tilde{\theta}$ is marched outwards with the FMM using either **Method 1:** constant angle or **Method 2:** linear extrapolation. For example, in Fig. 4.1, $\tilde{\theta}$ at point D is

Method 1: $\tilde{\theta}_D = \tilde{\theta}_C$,

Method 2: $\tilde{\theta}_D = min\left(\tilde{\theta}_{max},\ max\left(\tilde{\theta}_{min},\ \tilde{\theta}_C + (x_D - x_C)\frac{\tilde{\theta}_C - \tilde{\theta}_B}{x_C - x_B}\right)\right)$,

where $\tilde{\theta}_i$ and x_i are the isocontour angle and x-location of point i, respectively. $\tilde{\theta}_{min}$ and $\tilde{\theta}_{max}$ are minimum and maximum values of $\tilde{\theta}$. For physically realistic values, $0^o \leq \tilde{\theta}_{min} < \tilde{\theta}_{max} \leq 180^o$. To be consistent with Sec. 3.4, $\tilde{\theta}_{max} = \theta_{max} = 170^o$ and $\tilde{\theta}_{min} = \theta_{min} = 10^o$ throughout this work. While method 1 is simple, it is similar to the ghost interfaces approach (Sec. 3.2.3.3) and, therefore, is expected to be insufficient. Hence, the next order method (method 2) is also included. With such propagation of the angle $\tilde{\theta}$, information for determining u_n in the blind spot only depends on points that are closer to the interface and previously accepted, and no negative feedback was observed.

4.3 Spurious currents

To quantify the spurious currents using this transport scheme, a uniform circular arc with a contact angle $\theta = 45^o$ trapped between two complete slip walls is translated. This case is the same as the one used in Chap. 3: however, now, the arc must be transported; otherwise, the extension velocity scheme would not be engaged.

4.3.1 Configuration

Figure 4.3 shows the computational domain. It has a height H and a length L= $5H$. The inlet has a uniform velocity U for a capillary number Ca= $\mu U/\sigma = 1$ in the x-direction. Both fluids have equivalent densities ($\rho_1 = \rho_2$) and an Ohnesorge number Oh= $\mu/\sqrt{\rho\sigma H} = 0.1$. The initial condition of the level set ϕ was a signed distance function. The domain was discretized in square cells with a resolution of 125 H cells in the x-direction for the case labelled "Base". Three more grid resolutions were also considered and are referred to as "x2" , "x4", and "x8" for twice, four times, and eight times the number of grid points in the "Base" case. A time step of $\Delta t = 10^{-4}\mu H/\sigma$ was used in all simulations.

Since the extension velocity routine is concerned with calculating the correct interface velocity, the interface error here is characterized in terms of the magnitude of the parasitic currents. The exact solution to this problem is uniform, rigid-body motion at velocity U. Therefore, any velocity deviations are due to errors caused by the transport scheme. For simplicity, only the x-direction velocity errors are considered, but the y-direction velocity errors are comparable due to the fluid incompressibility. The L_∞ norm of the velocity error,

$$E = max(|u(\vec{x}) - U|) \, , \tag{4.9}$$

is evaluated at time t both over the entire computational domain (E_D, Figs. 4.4a and 4.5a) and only along the walls (E_W, Figs. 4.4b and 4.5b) at different grid resolutions. These errors are measures of the spurious (parasitic) velocity currents.

4.3.2 Velocity error

When method 1 (fixed angle) is used to propagate $\tilde{\theta}$, the velocity error does not show strong convergence behavior (when finer meshes are used) in either E_D or E_W (Fig. 4.4). This lack of convergence is expected; while $\partial(\hat{n} \cdot \vec{n})/\partial n$ (the contribution of $\kappa = -\nabla \cdot \hat{n}$ normal to the wall) is correct and

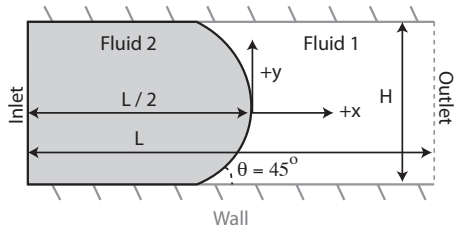

Figure 4.3: Simulation domain for the transport of a circular arc (not drawn to scale).

converges, the curvature contribution along the interface always has an error from the fixed contact angle. Thus, the spurious currents do not decrease to zero with increasing grid resolution for method 1. Method 2 (linear extrapolation), on the other hand, does exhibit error convergence for both E_D (Fig. 4.5a) and E_W (Fig. 4.5b). While the maximum error initially occurs along the wall ($E_D = E_W$), at later times the wall velocity error actually decreases and the maximum error occurs at the center of the arc. When doubling grid resolution, the maximum velocity error E_D decreases by a factor between 0.45 – 0.55 and is nearly linear in $\Delta x/H$ (Fig. 4.6) reflecting first-order convergence to the exact solution of zero. The linear $\tilde{\theta}$ extrapolation is the lowest order propagation method necessary for a solution that converges with grid resolution.

Although the velocity errors E_D were found to increase in time for method 2 (Fig. 4.5a), their magnitude is very small and can be controlled by sufficient mesh refinement. As will be shown in the next section, these errors do not have a large effect on the solution.

4.4 Example: Pinned droplet

This example is used to verify that the proposed extension velocity method does indeed capture the evolution of the contact angle. In order to show correct angle evolution, a non-equilibrium droplet subject to gravity on a wall is allowed to equilibrate and then its final shape is compared to the analytic solution.

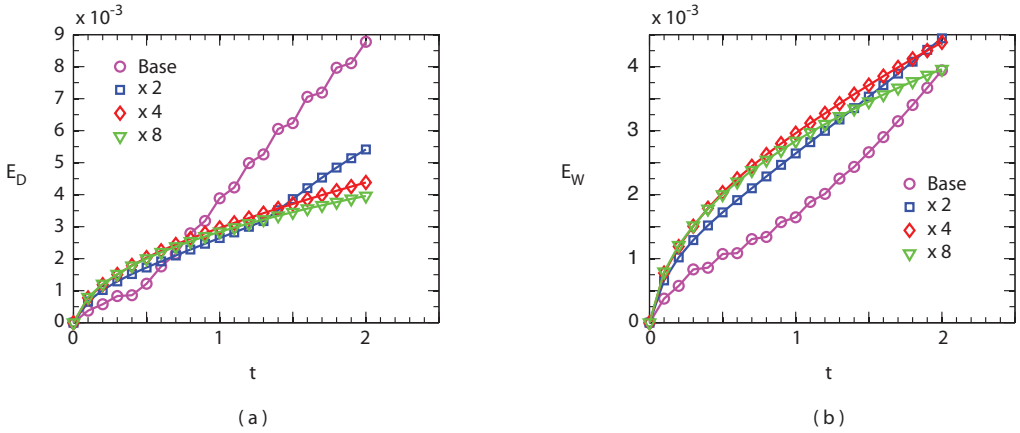

Figure 4.4: a) Domain spurious velocity error E_D and b) wall spurious velocity error E_W as functions of time when a fixed angle $\tilde{\theta}$ is propagated (method 1). Data sets differ by grid resolution. The multiplication factor is relative to the base resolution (125 H cells in the x-direction).

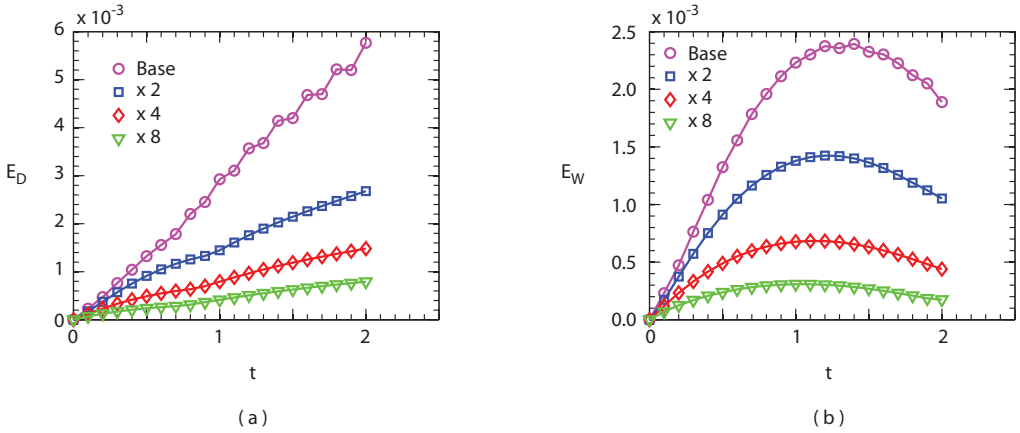

Figure 4.5: a) Domain spurious velocity error E_D and b) wall spurious velocity error E_W as functions of time when the angle $\tilde{\theta}$ propagated linearly (method 2). Data sets differ by grid resolution. The multiplication factor is relative to the base resolution (125 H cells in the x-direction).

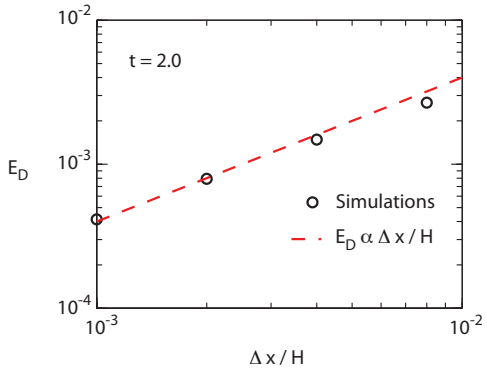

Figure 4.6: Domain spurious velocity error E_D as a function of the grid resolution $\Delta x/H$ for method 2 at time $t = 2$. The red dashed line is the behavior when E_D is linearly proportional to the grid cell size.

4.4.1 Configuration

The domain is a rectangle of height H and length $L = 2H$ surrounded by walls with a no slip velocity boundary condition (Fig. 4.7). The droplet is centered in the x-direction. The gravity vector of magnitude g is oriented parallel to the bottom wall and the density ratio of the fluids is set to $\rho_2/\rho_1 = 0.9$ to induce motion. The flow has an Ohnesorge number $\mathrm{Oh} = \mu/\sqrt{\rho_1 \sigma H} = 0.1$. A uniform grid of square cells with 200 H cells in the y-direction and a uniform time step Δt of $5 \cdot 10^{-4}$ $\mu H/\sigma$. Despite the no slip boundary condition on the wall, there is a small amount of numerical slip due to the finite grid discretization [96]. This small slip can change slightly the droplet base width W from its initial value. Therefore, all the final comparisons are made with the final value of the base width W (at equilibrium). The simulation is run until $t = 40$ when the drop appears to be at steady state and the velocity is three orders of magnitude smaller than its maximum in time.

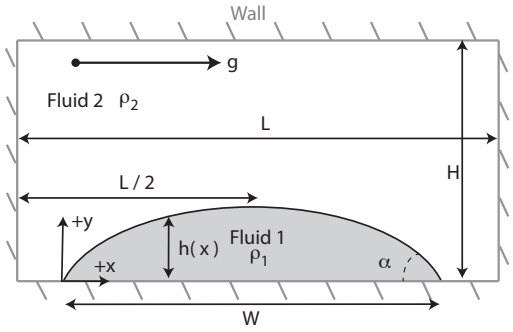

Figure 4.7: Configuration for a pinned droplet deformed by gravity in the positive x-direction (not drawn to scale).

4.4.2 Derivation

For a 2D, equilibrium capillary surface with contact angles less than 90^o, the surface can be expressed as a height profile $h(x)$ (Fig. 4.8a). This particular test case was chosen because it has an exact solution. When gravity g is present along the wall, the drop deforms into a bulb shape as in Sec.

3.5. An equilibrium fluid interface in this scenario can be derived from the Laplace condition,

$$[p] = \sigma\kappa \tag{4.10}$$

Using the height profile $h(x)$, this equation takes the form

$$[p] = \sigma \frac{-\frac{d^2h}{dx^2}}{\sqrt{1+\left(\frac{dh}{dx}\right)^2}}\,. \tag{4.11}$$

The hydrostatic pressure p_i in each fluid is simply

$$p_1 = \rho_1 g x + a_1$$

$$p_2 = \rho_2 g x + a_2$$

where a_1 and a_2 are constants. Combining these relations with Eq. 4.11, the governing non-linear, ordinary differential equation for the interface height $h(x)$ is

$$\sigma \frac{-\frac{d^2h}{\partial x^2}}{\sqrt{1+\left(\frac{dh}{dx}\right)^2}} = p_1 - p_2 = (\rho_1 - \rho_2)gx + (a_1 - a_2) = \Delta\rho g(x - x_0) \tag{4.12}$$

where x_0 is a constant. Physically, x_0 corresponds to the position where the surface curvature is 0 and the pressure is equal in both fluids. However, x_0 is not strictly defined to be between $x = 0$ and $x = W$. Let $\bar{*}$ be the non-dimensionalization of a variable with respect to drop width W. The governing equation can be recast as

$$\frac{\frac{d^2\bar{h}}{d\bar{x}^2}}{\sqrt{1+\left(\frac{d\bar{h}}{d\bar{x}}\right)^2}} = -\frac{\Delta\rho g W^2}{\sigma}(\bar{x} - \bar{x}_0) = -Bo_W(\bar{x} - \bar{x}_0) \tag{4.13}$$

where Bo_W is the Bond number using the length scale W. The boundary conditions for the equation are $\bar{h}(0) = \bar{h}(1) = 0$ since the drop is pinned. For a given $\bar{x}_0$ and Bo_W, this equation can be solved numerically. The Matlab script used to accomplish this is given in appendix A. The relative tolerance was set as 1/1000.

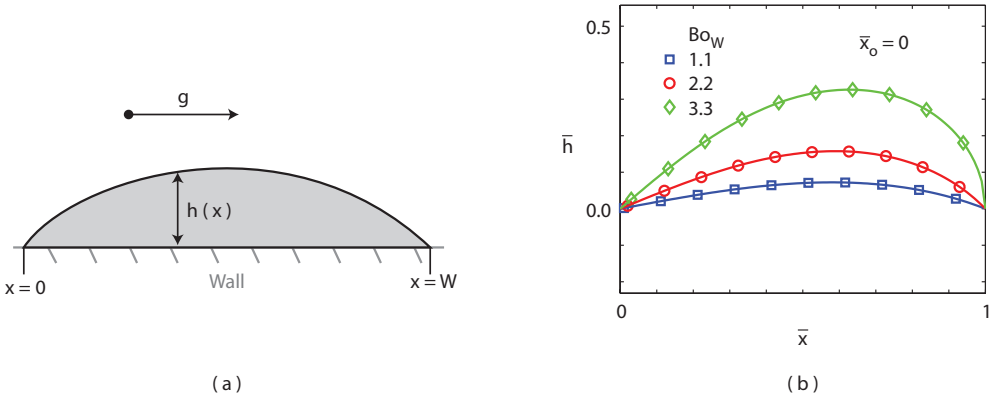

Figure 4.8: a) Diagram of an interface $h(x)$ pinned to the wall (not drawn to scale). b) Variation of the solution interface shape with Bond number Bo_W for fixed $\bar{x}_0$.

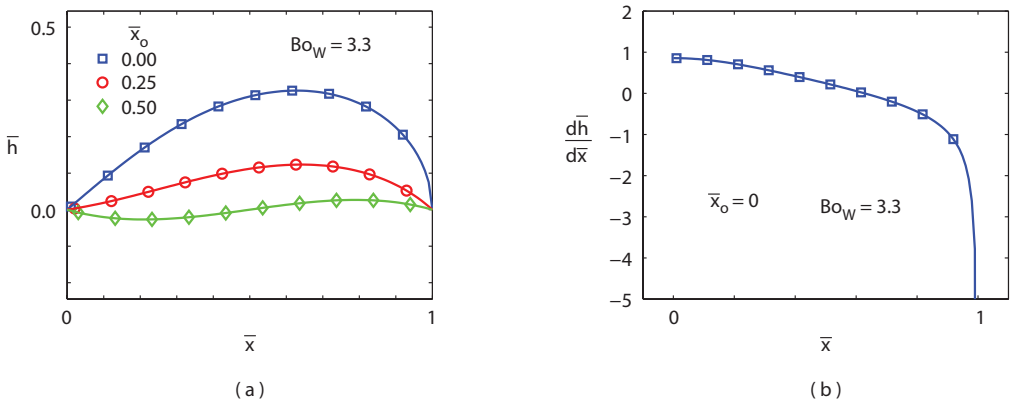

Figure 4.9: a) Variation of the solution interface shape with $\bar{x}_0$ for fixed Bond number Bo_W. b) Interface slope $\partial h/\partial x$ for the interfaces in (a).

4.4.3 Solution $\bar{h}$ behavior for different inputs, Bo_W and $\bar{x}_0$

Figures 4.8b and 4.9a show interface profiles varying either Bo_W or $\bar{x}_0$, respectively, while holding the other parameter fixed. The curve $Bo_W = 3.3$ and $\bar{x}_0 = 0$ is the same in both figures. These interface profiles are exact solutions to Eq. 4.13. The Bond number Bo_W determines the degree of asymmetry in the droplet shape while x_0 moves the curvature inversion point of the shape. It is important to note that solutions may not exist for all combinations of $\bar{x}_0$ and Bo_W. For $\bar{x}_0 = 0$ (Fig. 4.8b), there is a practical limit for solving Eq. 4.13 at $Bo_W \approx 3.3$. At this value of the Bond number, the right edge of the droplet has a contact angle $\theta \approx 90^o$ ($\partial\bar{h}/\partial\bar{x} \to -\infty$, Fig. 4.9b) and $\bar{h}$ becomes multivalued at $\bar{x} = 1$. As a result, the interface equation as formulated (Eq. 4.13) is no longer valid. For fixed Bond number Bo_W, the value of $\bar{x}_0$ could make $\bar{h} < 0$ at some locations which is also physically unrealistic (Fig. 4.9a).

The constant $\bar{x}_0$ is not easily determined *a priori* for a given initial condition. For a given Bond number Bo_W, it is assumed $\bar{x}_0$ corresponds to a unique drop area. This assumption seems to be supported by numerical results. As $\bar{x}_0$ increases in Fig. 4.9a, the surface height $\bar{h}$ at every point (save the ends) decreases. To compare solutions, the normalized droplet area $\mathfrak{A}$ is first calculated from the fluid mechanics results. Then, Eq. 4.13 is solved for a range of $\bar{x}_0$ and the solution that most closely matches the area $\mathfrak{A}$ is taken as the equilibrium solution.

4.4.4 Simulation comparison to the exact solution

The case chosen for comparison is $\bar{x}_0 = 0$ and $Bo_W = 3.3$ which is the most highly deformed drop as it approaches the contact angle limit. The initial condition is a circular arc of width $W = H$ and contact angles $\alpha = 64.79^o$. The initial shape of the droplet and its equilibrium shape are shown in Fig. 4.10a. The trailing edge ($\bar{x} = 0$) of the final shape has a different contact angle than initially and is slightly displaced due to the small inherent, grid-dependent slip. This slip distance decreases with grid resolution since the no slip velocity boundary condition is more strictly enforced. The final shape has a base width $W = 0.9787\ H$ and the corresponding Bond number is now $Bo_W = 3.16$.

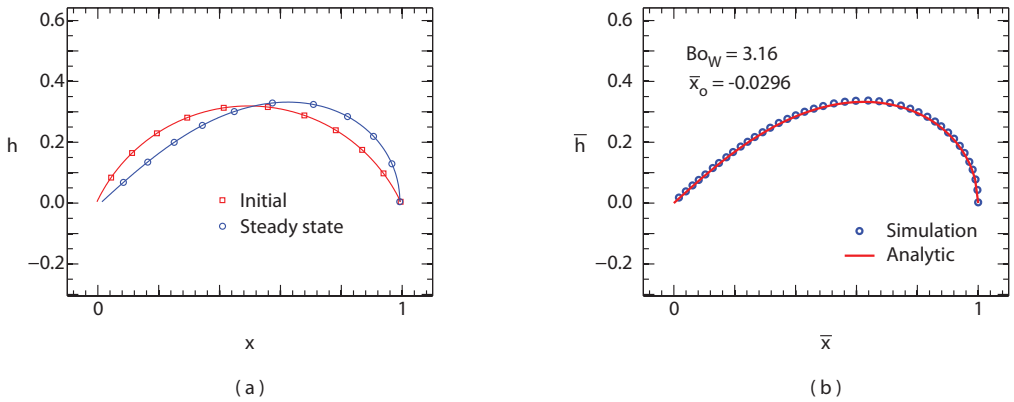

Figure 4.10: a) Initial (red squares) and steady state (blue circles) surface shapes. b) Comparison on the solution for Eq. 4.13 (curve) and the numerical simulation (dots) for a $Bo_W = 3.16$ and $\bar{x}_0 = -0.0296$.

Angle	Simulation	Analytic
Leading edge	89.59^o	89.69^o
Trailing edge	41.02^o	41.30^o

Table 4.1: Leading and trailing contact angles for the pinned droplet. The angles were estimated using a quadratic polynomial.

The fitted value $\bar{x_0} = -0.0296$ gives the closest approximation to the drop area $\mathfrak{A}$. The contact angle at the leading edge ($\bar{x} = 1$) is very close to 90^o which prevents a closer area fitting. The simulated drop shape is shown with the exact solution to the boundary value problem (Eq. 4.13) in Fig. 4.10b. The qualitative agreement is very good. Importantly, the solution contact angles are captured correctly (Tab. 4.1).

4.5 Extensions and limitations of blind spot extension velocities

Although the algorithm presented here is in 2D, the technique can be readily extended to 3D. The two equations that need to be reconsidered are the condition for constant tangential velocity u_{tan} (Eq. 4.8) and the linear extrapolation of the isocontour angle $\tilde{\theta}$ (method 2). The tangential velocity can still be held constant by changing the right side of Eq. (4.8) into a weighted average

of $u_n sin(\tilde{\theta})$ at the accepted neighbors along the wall where the weighting is determined by the 3D normal vector at point $\vec{x}$. Similarly, the extrapolation of angle $\tilde{\theta}$ can be determined by solving the equation $\nabla_s^2 \tilde{\theta} = 0$ where ∇_s^2 is the surface Laplacian operator for the accepted neighbor points and the derivatives are approximated by stencils biased towards accepted points. Such an extension greatly increases application of the method for realistic simulations.

It is important to note that the results presented here do not imply that the reinitialization step can be forgone; rather, it can be used less often and the values of θ_o (used in Eq. 3.8) have higher fidelity. There are three reasons why reinitialization (defined in the previous chapter) is still necessary. First, the narrow band structure requires reinitialization: when the interface moves and new points are added to the narrow band, reinitialization is necessary to set the values of these new points. Second, regions where the isocontour normal is not well defined, such as circle centers, will have inaccurate values of the extension velocity u_n. The limiters on the derivatives in Eq. 4.7 are a solution to this problem, but they are not sufficient. Reinitialization inherently fixes the level set ϕ. Third, as shown in Fig. 4.5, the velocity errors are growing in time t. This growth rate scales approximately linearly with the velocity U (and subsequently Ca) because the errors in the advection equation are multiplied by the velocity magnitude. While the errors are less than 1% for all the grid resolutions shown (Fig. 4.5), at some time the error might grow to unacceptable levels. A reinitialization step would smooth out the level set and reduce these errors. Higher-order discretizations of the extension velocity FMM are also expected to reduce these errors. However, while such algorithms exist, their implementation is more complicated [124] and beyond the scope of this work.

4.6 Reinitialization with angle propagation

Ideally, a reinitialization technique should handle the blind spot correctly even with an incorrect initial level-set field. In other words, the reinitialization technique should populate the blind spot with correct values as long as the interface location is known. For an incorrect level set function

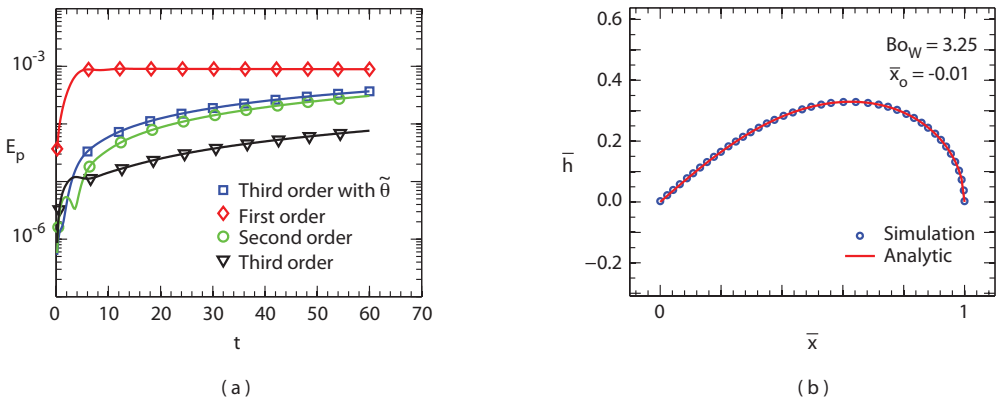

Figure 4.11: a) Integrated error E_P for a circular arc (Sec. 3.3). b) Equilibrium surface using the QUICK transport scheme and the reinitialization routines with angle $\tilde{\theta}$ (Sec. 4.4).

away from the interface ($\phi = 0$), the computed local θ_o could be wrong, but the propagated $\tilde{\theta}$ would still be a good approximation to the correct target angle. The relaxation equation (Eq. 3.8) becomes

$$\frac{\partial \phi}{\partial \tau} = sgn \cdot \left(cos(\tilde{\theta}) - \left(\frac{\frac{\partial \phi}{\partial n}}{|\nabla \phi|} \right) \right) . \tag{4.14}$$

By using the angle $\tilde{\theta}$ from Sec. 4.2.2.2 instead of the angle θ_o in Eq. 3.8, the level set in the blind spot is constructed using data from points closer to the interface. An incorrect level set is transformed into one consistent with the fluid interface. This reinitialization would be a stand-alone procedure.

To demonstrate the reinitialization with angle propagation, two previous cases are repeated. The circular arc integrated error E_p for the prior relaxation equation tests (Sec. 3.3) and this new scheme is shown in Fig. 4.11a. The angle propagation does decrease the accuracy of the solution since the new solution (blue squares) has more error than the original third-order test (black triangles), but it has nearly the same error as the second-order relaxation equation (green circles). Figure 4.11b shows the equilibrium surface for the droplet in Sec. 4.4. In these new simulations, the QUICK scheme was used to advect the level set. The angle evolution is again preserved correctly. The values of $Bo_W = 3.25$ and $\bar{x}_0 = -0.01$ ($W = 0.993\ H$) are closer to the values originally targeted indicating less numerical slip of the surface profile.

While the extension velocities can be used, they are inherently low-order since a first order FMM was employed unlike the QUICK transport scheme (third-order spatial accuracy). Furthermore, the QUICK scheme is more computationally efficient than the extension velocities since u_n does not need to be calculated. For these reasons, the QUICK scheme is used in the remainder of the present work.

4.7 Summary

In this chapter, an algorithm to construct extension velocities in the blind spot was developed. This method propagates the value of the tangential extension velocity, u_{tan}, along the wall. This choice is consistent with uniform translation along the wall. To prevent an instability, it was also necessary to propagate the local level-set contact angle θ along the wall away from the interface. This angle $\tilde{\theta}$ must be propagated with at least linear extrapolation to capture accurately cases with non-zero curvature. This choice enforces the curvature at the contact line in a manner similar to the relaxation equation. While the extension velocities can be used for advection, angle propagation algorithm is further extended to the relaxation equation and found sufficient for easier advection schemes. The reinitialization routine at a contact line is now complete, self-sufficient, and accurate. Hereafter, this reinitialization will be referred to as the relaxation equation reinitialization. The QUICK scheme will be used to advect the level set ϕ. The following chapter adds contact-line physics.

Chapter 5

Volumetric-filtered contact-line source terms

Do what you can, with what you have, where you are.

— Theodore Roosevelt

5.1 Introduction

The prior two chapters developed a level set function transport scheme and a reinitialization routine that did not produce parasitic velocity currents at contact lines. All previous simulations were performed without knowledge of a specific contact angle. Realistic simulations must also contain contact-line physics. This is the focus of this chapter. Section 5.1.1 introduces the assumptions for the contact-line physics and Sec. 5.1.2 describes the inherent numerical difficulties for these conditions.

5.1.1 Assumptions

As discussed in Sec. 1.2.2, there are two necessary pieces: a velocity boundary condition at the wall to remove the stress singularity and a means to achieve the equilibrium contact angle at rest. The choices adopted are

Assumption 1: a Navier-slip boundary condition (Eq. 1.4),

Assumption 2: a fixed contact angle at the wall.

Both of these assumptions have arguments for and against them and all of the modeling results are subject to their validity. Since the Navier-slip boundary condition (Assumption 1) has been observed in molecular dynamic simulations for small (subcritical) shear rates [151, 152], this choice may be physically accurate. Other authors have argued that a slip-model-based approach cannot describe experiments [132] or that the slip length is not a physical quantity, but rather it is a function of the contact-line speed [39, 92] or spatially varying [77]. Nevertheless, it has been suggested that different slip models will *macroscopically* look alike [38, 128] and thus it is not necessary to have the slip model exactly correct. Natural choices for the fixed contact angle (Assumption 2) are the static equilibrium angle θ_S, the static advancing angle θ_{sa}, and the static receding angle θ_{sr}. The later two can be used to represent contact angle hysteresis [23, 113]; for simplicity, the static contact angle θ_S is considered in this chapter, but the hysteresis angles can be substituted for it as a simple contact angle hysteresis model (Chap. 6). A fixed static contact angle (Assumption 2) is often used in numerical [19, 137] and classic analytic [28, 63, 67] studies. Other studies, however, have suggested that the microscopic contact angle is not fixed (Assumption 2); rather, it is velocity dependent due to changing surface energies in Young's equation (Eq. 1.1) [129]. There is no common agreement in literature for what choices are the best; the choices adopted here are the simple, classical options. With these choices, the fluid mechanics is mathematically well-posed.

While other phenomenon such as evaporation / condensation [126, 127] and disjoining pressure [6, 109, 165] could be modeled, excluding these mechanisms does not necessarily limit the applicability of the mathematical framework developed in this chapter. The slip length λ, which is fit to experimental data, may even be equivalent to substrate heterogeneities [83] and other physical mechanisms [120, 134]; this "effective slip length" is a model itself. For example, the Cassie-Baxter model for wettability on porous surfaces [23] has pockets of gas trapped underneath the liquid. The trapped gas could be represented by a large slip length since the surface is less resistant to flow than a solid

surface. Despite the assumption limitations, relevant interfacial fluid dynamics can still be examined.

If the slip length is of the order of molecular length scales, the continuum limit may no longer apply [132]. In order to still use the Navier-Stokes equations (Eq. 2.1), the fluid is approximated as still in the continuum-limit.

Assumption 3: Continuum fluid mechanics can be used at the slip length scale.

5.1.2 Numerical limitation

There is a fundamental computational challenge when using the Navier-slip boundary condition; realistic slip lengths are expected to be of the order of nanometers [39, 92]. For millimeter sized droplets, this problem could have over 6 orders of magnitude difference in length scales! This is the multiscale nature of the contact-line problem. For DNS, computational memory is a limiting factor. Furthermore, even if non-uniform meshes are used, the capillary CFL condition (Eq. 2.21) requires a prohibitively small time step Δt because the smallest grid dimension must be less than the slip length in order to achieve velocity convergence [4, 137]. Using adaptive mesh refinement (AMR), the smallest slip length ratio simulated to date is 10^{-4} by Sui and Spelt [141, 142]. Ideally, one would prefer to perform simulations with a grid length scale $\Delta x >> \lambda$ to reduce both of these limitations. For these grid sizes, however, the shear rate near the contact line is not captured well (Fig. 5.1). The viscous resistance is underestimated. Even for a no slip boundary condition, there is an inherent grid dependent slip [96] due to this missing resistance.

The approach explored here to capture this unaccounted viscous shear at large length scales Δx is similar in concept to Large Eddy Simulations for turbulent flows [118]. When volume averages occur on a length scale $\Delta x >> \lambda$, there will be unclosed terms in the Navier-Stokes equations. Rather than calculate the dynamic or apparent contact angles, these source terms will just add the physics that are under-represented on a coarse mesh. The contact angle at the cell center nearest the wall can be left freely floating using the relaxation equation reinitialization and will be determined by

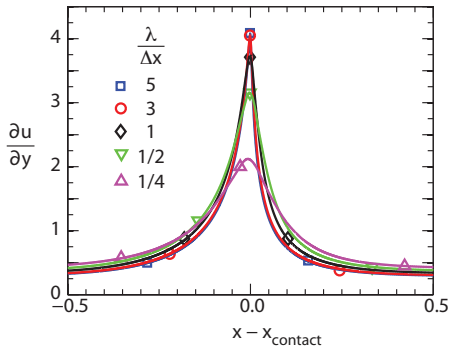

Figure 5.1: Shear rate $\partial u/\partial y$ along the wall. The curves are different number of grid points per slip length λ.

all the physics in the simulation as a whole. There are three major benefits to this approach over a contact angle law. First, some variable dependencies, such as the Reynolds number Re, do not have to be known *a priori* since these are inherent to the simulation. Second, non-unique contact angles are allowed; the contact angle can be history dependent. Lastly, reinitialization at every time step is not required since the contact angle is not enforced by it. The modeled terms may have sufficient accuracy to enable simulation of multiple droplet contact lines without supercomputers.

To derive appropriate momentum source terms, the Navier-Stokes equations are first volume-filtered in Sec. 5.2 to identify the terms that need to be modeled. Then, a collection of fully-resolved simulations for a 2D Cartesian capillary are performed and analyzed to determine appropriate forms of the average curvature and the contact-line viscous shear (VS). While the slip length λ in these exploratory simulations is made rather large to be computationally tractable, useful scaling information can still be obtained; these scalings are assumed to hold at smaller slip lengths. Unfortunately, a true computational comparison at these small length scales is not possible with current computer technology. To the author's knowledge, this is the first study to numerically analyze the scaling of the viscous resistance at a contact line for the Navier-slip boundary condition. Prior work by Afkhami and Bussmann [4] and Spelt [137] showed similar velocity distributions along the wall, but those works only used these curves to show convergence of the numerical solutions. The viscous resistance is examined here as a function of the static contact angle θ_S, the slip length ratio ϵ, and

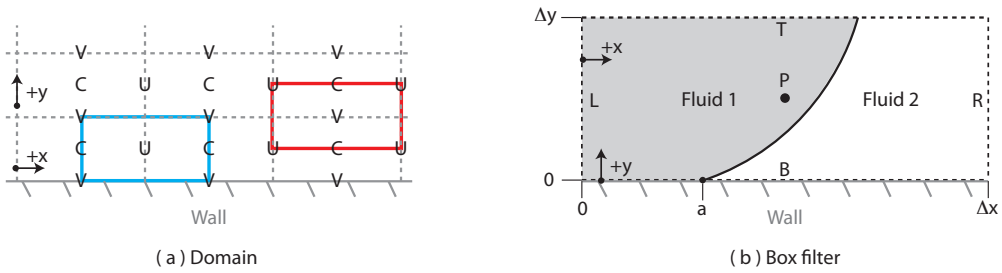

Figure 5.2: a) Diagram of the staggered grid. C is the locations of cell centered variables and u, v are the face centered velocity locations. The blue and red rectangles are the control volumes (box filters) $\mathfrak{V}$ centered on u and v, respectively. b) 2D box filter of size Δx x Δy containing the contact line. L, R, T, and B denote the four cell sides. Point P is the grid node about which the control volume is centered.

the capillary number Ca. These relations would fully close the momentum equations and enable simulations with small and realistic slip lengths on coarse meshes. This approach is general: other physical mechanisms such as evaporation can be easily incorporated using this methodology if so desired.

5.2 Filtered Navier-Stokes equations at a contact line

The filtered Navier-Stokes equations are derived using a box filter. In other words, the equations are averaged over a given volume. The volume integration (filter) over a control volume $\mathfrak{V}$ is defined as

$$\overline{\Psi} = \frac{1}{\mathfrak{V}} \iiint_V \Psi \mathrm{d}\mathfrak{V} = \frac{1}{\mathfrak{V}} \left(\iiint_{\mathfrak{V}_1} \Psi \mathrm{d}\mathfrak{V} + \iiint_{\mathfrak{V}_2} \Psi \mathrm{d}\mathfrak{V} \right) \tag{5.1}$$

where Ψ represents any quantity and $\mathfrak{V}_i$ is the volume of fluid i. Integrating Eq. 2.1 over a grid cell and applying the divergence theorem,

$$\frac{\partial \overline{\rho \vec{u}}}{\partial t} + \frac{1}{\mathfrak{V}} \iint_S (\rho \vec{u} \otimes \vec{u}) \cdot \mathrm{dS} = -\frac{1}{\mathfrak{V}} \iint_S P \mathrm{dS} + \frac{1}{\mathfrak{V}} \iint_S D \cdot \mathrm{dS} \tag{5.2}$$

where S is the surface of the box filter. Only the 2D case (box filter size $\Delta x \times \Delta y$) with a horizontal wall is shown here for simplicity, although an extension to 3D or vertical walls is straightforward.

The staggered mesh arrangement is shown in Fig. 5.2a: u / v denote the face centered locations of the velocity components and C represents the cell centers where the level set ϕ, curvature κ, and pressure p are stored. The box filter for volume averaging the x-momentum equation is in blue while the red box is for the y-momentum equation. As the slip length affects the behavior only close to the wall, grid cells far away from the contact line should be well approximated on the coarse mesh and do not need to be considered. Since the v grid cell near the wall (red, Fig. 5.2a) does not contain a contact line, the y-momentum equation does not need to be considered: the field of surrounding information is the same as anywhere else in the fluid domain and all quantities are correct in the macroscopic sense. The x-momentum equation, however, is affected by contact lines for the given wall orientation. A box filter containing a contact line is shown in Fig. 5.2b. L, R, T, and B are the left, right, top, and bottom edges of the cell, respectively. Let LHS be the left hand side of the x-component of Eq. 5.2 (u-momentum equation). The inertial terms (LHS) are most important at large length scales and thus do not need to be modeled. Terms will be added to LHS if they are correct in the macroscopic sense and do not require variable closure. **Note:** LHS does not have a rigid value in this derivation. All terms that need to be modeled will be isolated on the equation's right hand side. In this notation,

$$\begin{aligned} LHS = \frac{1}{\Delta x \Delta y}\int_0^{\Delta y}(P_L - P_R)\mathrm{dy} + \frac{1}{\Delta x \Delta y}\int_0^{\Delta y}\left(2\mu\frac{\partial u}{\partial x}_R - 2\mu\frac{\partial u}{\partial x}_L\right)\mathrm{dy} + \\ \frac{1}{\Delta x \Delta y}\int_0^{\Delta x}\left[\mu\left(\frac{\partial v}{\partial x}+\frac{\partial u}{\partial y}\right)_T - \mu\left(\frac{\partial v}{\partial x}+\frac{\partial u}{\partial y}\right)_B\right]\mathrm{dx} \end{aligned} \tag{5.3}$$

Subscripts indicate the side over where each term is evaluated.

Assumption 4: The averaging volume dimensions are much larger than the slip length, $\lambda << \Delta x, \Delta y$.

This regime is where a model would be most useful. The contact line is assumed to be generally far away from the edges (L and R) and only at the edges momentarily such that the velocity distortion due to the contact line is fully contained in the grid cell. In this case, the top T, left L, and right R sides are far away from the contact line: the averages over these sides do not need to be modeled. The bottom B, however, does need to be considered as well as the effect on the jump condition in

pressure. For ease of notation, let

$$\overline{a}^x = \frac{1}{\Delta x}\int_0^{\Delta x} a\mathrm{dx}$$

$$\overline{a}^y = \frac{1}{\Delta y}\int_0^{\Delta y} a\mathrm{dy}$$

be the directional averages of quantity a. Moving terms to LHS, Eq. 5.3 becomes,

$$LHS = \frac{1}{\Delta x}\left(\overline{P_L}^y - \overline{P_R}^y\right) - \frac{1}{\Delta y}\overline{\left(\mu\frac{\partial v}{\partial x}\right)_B}^x - \frac{1}{\Delta y}\overline{\left(\mu\frac{\partial u}{\partial y}\right)_B}^x \tag{5.4}$$

Since $v = 0$ on the wall (no penetration boundary condition), the second term on the right hand side is identically zero. To further reduce the first term on the right hand side, an assumption consistent with the GFM is used,

Assumption 5: $\nabla\overline{P}^y$ is the same on both sides of the interface.

The pressure difference to first order can be written as

$$\overline{P_L}^y - \overline{P_R}^y = -\nabla\overline{P}^y\Delta x + [\overline{P}^y] \tag{5.5}$$

where $[a]$ is a jump in the variable a across the interface between the fluids. Applying the simplified Laplace condition (Eq. 2.17),

$$\overline{P_L}^y - \overline{P_R}^y = -\nabla\overline{P}^y\Delta x + \overline{\sigma\kappa}^y \tag{5.6}$$

The gradient of $\overline{P}^y$ is a macroscale quantity and can be added to LHS. If the surface tension σ is constant, it can be removed from the average in the last term. Eq. 5.4 then simplifies to

$$LHS = \frac{1}{\Delta x}\sigma\overline{\kappa}^y - \underbrace{\frac{1}{\Delta y}\overline{\left(\mu\frac{\partial u}{\partial y}\right)_B}^x}_{VS} \tag{5.7}$$

Two unclosed terms remain: an average curvature $\overline{\kappa}^y$ and a viscous shear (VS). These terms are modeled from DNS. All other terms are the exact same as in the unfiltered Navier-Stokes equations.

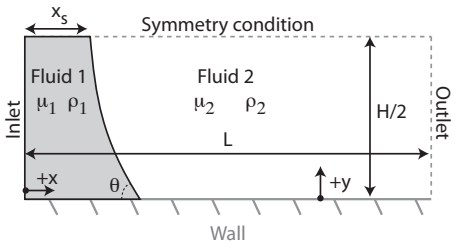

Figure 5.3: 2D Cartesian capillary tube domain for the DNS of contact line dynamics (not drawn to scale).

5.3 Slip-length resolved simulations

DNS were conducted to generate interface and velocity data for approximating the average curvature and the viscous shear VS. This section describes the configuration (Sec. 5.3.1), parameters examined (Sec. 5.3.2), and a new numerical implementation for the contact angle (Sec. 5.3.3). The results from these simulations are analyzed in the subsequent sections (Sec. 5.4 and 5.5).

5.3.1 Configuration

The test geometry for the DNS is a 2D Cartesian capillary tube of height H and length L (Fig. 5.3). A symmetry boundary condition is imposed at the top of the domain to decrease the number of grid nodes. The inlet has a Poiseuille flow velocity distribution with mean velocity U_{CL} and the outlet has a zero Neumann boundary condition for the normal velocity u. The bottom wall has a Navier-slip boundary condition on u (Eq. 1.4) and a no penetration boundary condition on v. In other works [46, 128, 137], a grid resolution of 5 points per slip length was determined sufficient for solution convergence. As such, gird cells are squares with sides $\Delta x = \Delta y = \lambda/5$. The initial fluid interface is a circular arc located a distance X_S from the inlet with the static contact angle θ_S at the wall. The simulations are run until a steady interface shape has been achieved with uniform velocity U_{CL} in the x-direction and zero velocity in the y-direction. The exact values of the domain length L, interface start location X_S, time step Δt, and the end time t_{end} are unimportant as long as the interface has sufficient space and time to evolve towards a steady propagating interface. The QUICK scheme and relaxation equation reinitialization are used with the level set (Chap. 3 and 4).

While most DNS did not require more than two days run-time on one 12-core Intel Xeon CPU node, a few modifications were necessary to decrease the simulation time for the smallest slip lengths, $\lambda = H/160$ and $H/320$. In these cases, four changes were employed. First, the reinitialization frequency was reduced to only once every hundred time steps. Since the reinitialization is computationally expensive, real simulation time greatly decreases with reinitialization frequency. This less-often reinitialization frequency is allowed because of the techniques discussed in the previous chapters. Second, only a region around the interface had grid size $\Delta x = \lambda/5$; far away from the interface, the grid cell size Δx grew exponentially by a factor of 1.1 to decrease the total number of grid nodes while still isolating the inlet and outlet. Third, the initial condition was no longer a circular arc; rather, the initial condition was the final solution at the next largest value of the slip length λ. This change substantially decreased the number of time steps necessary to reach steady state. Lastly, the domain was only decomposed in the y-direction among the multiple processors for better load balancing. Otherwise, only the processors containing the interface would be utilized when calculating curvature and reinitializing. A steady state profile computed in this way was compared against the original procedure for $\lambda = H/80$, $\theta_S = 50^o$. The profiles were found identical.

5.3.2 Relevant parameters

Only part of the contact-line parameter space is examined in this study. Continuum-scale dimensionless parameters that could play a role in the contact-line region are:

- Reynolds number Re$= \rho_1 U_{CL} L_M/\mu_1$
- Density ratio $\eta = \rho_2/\rho_1$
- Viscosity ratio $\xi = \mu_2/\mu_1$
- Slip length ratio $\epsilon = \lambda/L_M$
- Static contact angle θ_S

- Capillary number Ca= $\mu_1 U_{CL}/\sigma$

where L_M is a large length scale in the problem. For the 2D Cartesian capillary geometry, L_M is chosen to be capillary height H. Since viscous effects are expected to dominate in the vicinity of the wall, the fluid is in the Stokes flow regime. For Stokes flow, neither the Reynolds number Re nor the fluid densities (hence η) are important parameters and, therefore, they are not considered. Furthermore, Stokes flow implies that the fluid behavior next to the contact line can be assumed quasi-static. The viscosity ratio ξ was examined and found to have a weak dependence on the models derived outside of its current use; it will not be discussed here. All simulations have unity values of the density ratio η and the viscosity ratio ξ since the specific values are unnecessary in the current model. A parameter space of the remaining three variables is considered. The slip length ratio ϵ is varied from 1/20 to 1/80 with two additional points at 1/160 and 1/320. These values of ϵ are somewhat large to be computationally feasible. The static contact angle θ_S is varied in the partially-wetting regime ($30^o < \theta_s < 150^o$) for two reasons. First, this regime is more difficult to describe analytically because lubrication approximation approaches are not appropriate. Despite its obvious physical relevance, this partially-wetting regime has also not been as well characterized. Second, the square grid cells can better approximate interfaces and the relaxation equation (Eq. 3.5) converges best for angles that are not near 0^o or 180^o. The simulations here are not expected to easily capture entrained fluid films that may exist on surfaces when the grid is not sufficiently refined. The capillary numbers Ca are 0.0033, 0.01, and 0.03. At these capillary numbers, surface tension effects are dominant. For the largest capillary number, the number of available contact angles θ_S is reduced because the apparent contact angle θ_{app} for the fluid profile approaches 180^o and a film of fluid 2 remains on the wall (viscous fingering).

A table of all the simulations performed and the figures where they are used is given in appendix B.

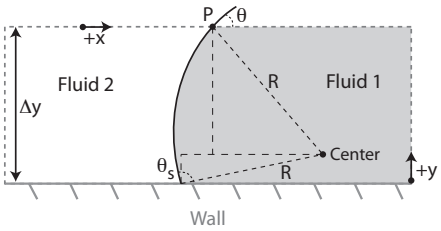

Figure 5.4: Diagram of the geometry when calculating the average interface curvature. The interface intersects the wall at the static contact angle θ_S and has an angle θ at point P.

5.3.3 Contact angle implementation

In order to enforce a static contact angle at the wall (Assumption 2), a fixed angle could be used for θ_o in the relaxation equation (Eq. 3.5). In other words, $\theta_0 = \theta_S$. This approach, however, **requires** reinitialization at every time step to ensure the angle is exact. Rather than a strong boundary condition for angle enforcement, a weak boundary condition would allow reinitialization to occur less often. This is a new approach. One such option is adding a forcing term to the Navier-Stokes equations at the contact line. The forcing term chosen here is an additional curvature contribution at the contact line,

$$\kappa_{app} = \kappa + \frac{cos(\theta) - cos(\theta_s)}{\Delta y} c \tag{5.8}$$

where κ_{app} is the curvature applied in the GFM, κ the curvature calculated from the level set variable ϕ, θ the contact angle calculated from ϕ, θ_S the static contact angle, and c any positive constant. This term was observed to drive the angle to the static contact angle for $c = 1$. The choice of c is arbitrary and larger values can be used to more strictly enforce the static contact angle.

5.4 Average curvature model

In this section, a model is proposed for the average curvature and then compared to DNS interface results from Sec. 5.3. The last subsection describes how this term can be implemented numerically.

5.4.1 Model derivation

To derive a model for the average curvature, a point P at distance Δy above the wall is considered (Fig. 5.4). The fluid interface at point P has an isocontour angle θ relative to the wall orientation.

Assumption 6: The fluid interface smoothly transitions from an apparent contact angle θ at $y = \Delta y$ to the static contact angle θ_S at $y = 0$.

Averaging is a naturally smoothing process; therefore, an average curvature should be the approximation from such a smooth interface. This assumption may not be good if a fluid film is entrained at the wall ($\theta \sim 180^o$). A smooth angular transition can be approximated by a circular arc of radius R. From the geometry in Fig. 5.4, the distance Δy can be expressed as

$$\Delta y = R\cos\left(180^o - \theta_S\right) + R\cos\left(\theta\right) \ . \tag{5.9}$$

Rearranging and using trigonometric relations, the average interface curvature in the plane is

$$\bar{\kappa} = \frac{1}{R} = \frac{cos\left(\theta\right) - cos\left(\theta_s\right)}{\Delta y} \ . \tag{5.10}$$

This formula is the same regardless of the orientation of θ and θ_S; it is not specific to the curvature shown in Fig. 5.4. This formula is similar to those used by other authors [19, 31, 160]. Surprisingly, this formula is consistent with other physical arguments. If the unbalanced (non-compensated) Young's force (Eq. 1.2) is averaged over the height Δy, a similar forcing term is obtained,

$$F_Y = \frac{1}{\Delta y}\int_0^{\Delta y} \delta(y)\sigma\left(cos\left(\theta\right) - cos\left(\theta_s\right)\right) dy = \sigma\frac{cos\left(\theta\right) - cos\left(\theta_s\right)}{\Delta y} \tag{5.11}$$

where δ is the Dirac delta function. This variation assumes a dynamic contact angle θ at the wall. The model derived here could, therefore, arise from other derivations.

Fig. #	θ_S	Ca	ϵ
5.5	50^o	0.01	1/40
5.6	90^o	0.01	1/40
5.7	50^o	0.03	1/40
5.8	50^o	0.01	1/80

Table 5.1: Values for the capillary number Ca and static contact angle θ_S in Fig. 5.5 – 5.8.

5.4.2 Average curvature from DNS

The DNS results are post-processed to determine the correct average curvature. A selection of results are shown in Fig. 5.5 – 5.8. Other parameter values showed similar results. The slip length ratio ϵ, the capillary number Ca , and the static contact angle θ_S for these simulations are given in Table 5.1. All of these figures show the initial and final steady-state interface profiles in panel (a). The static contact angle is maintained at the bottom of the interface in all cases since the initial and final curves align there. This result implies that the weak boundary condition for angle enforcement (Sec. 5.3.3) is sufficient to enforce the static contact angle at the wall. In panel (b) of Fig. 5.5 – 5.8, the exact value of the interface curvature κ is shown by the black circles, the average value of the curvature is the red squares, and the average curvature from the model (Eq. 5.10) is the blue diamonds. In all cases, the model agrees very well with the DNS average curvature at distances larger than five slip lengths from the wall. The agreement is slightly better for static contact angles approaching 90^o (Figs. 5.5b and 5.6b) and worse as the capillary number Ca increases (Figs. 5.5b and 5.7b). As the slip length ratio ϵ decreases, the comparison also improves (Figs. 5.5b and 5.8b). In summary, the model appears to represent the average curvature very well.

5.4.3 Model implementation

Implementing the average curvature model is straightforward. For nodes at the contact line, the interface curvature κ is replaced by the average curvature $\bar{\kappa}$ (Eq. 5.10) in the Laplace condition (Eq. 2.17) for the GFM. This substitution only occurs for velocity components tangential to the wall. For example, with the horizontal wall orientation in Fig. 5.2a, the Laplace condition for

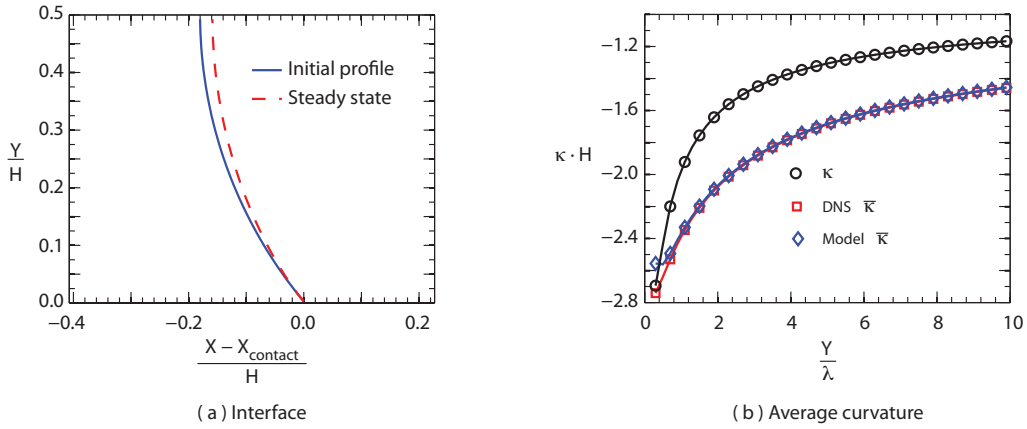

Figure 5.5: Results for $\epsilon = 1/40$, $\theta_S = 50^o$, and $Ca = 0.01$. a) Interfaces profiles at $t = 0$ and at steady state. b) The actual curvature κ at a given y location (black circles), the average curvature $\bar{\kappa}$ from the DNS (red squares), and the average curvature $\bar{\kappa}$ from Eq. 5.10 (blue diamonds). The x-axis of the plot is distance from the wall in slip lengths.

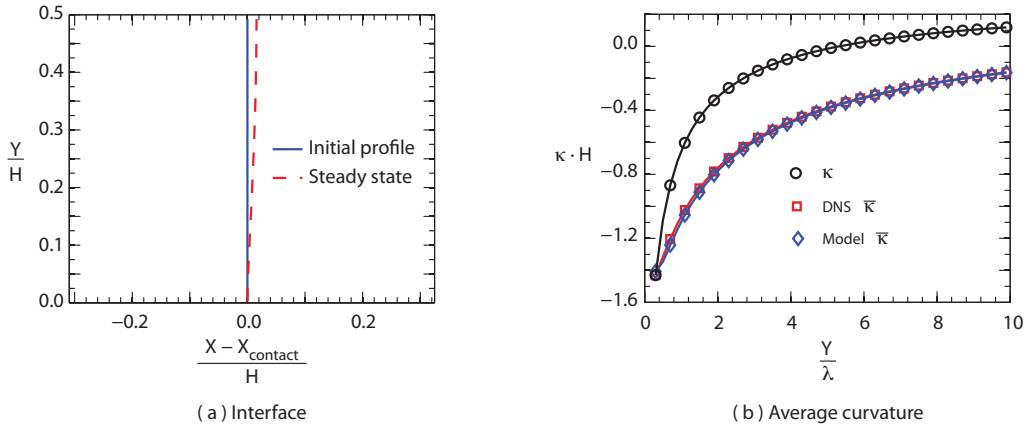

Figure 5.6: Results for $\epsilon = 1/40$, $\theta_S = 90^o$, and $Ca = 0.01$. a) Interfaces profiles at $t = 0$ and at steady state. b) The actual curvature κ at a given y location (black circles), the average curvature $\bar{\kappa}$ from the DNS (red squares), and the average curvature $\bar{\kappa}$ from Eq. 5.10 (blue diamonds). The x-axis of the plot is distance from the wall in slip lengths.

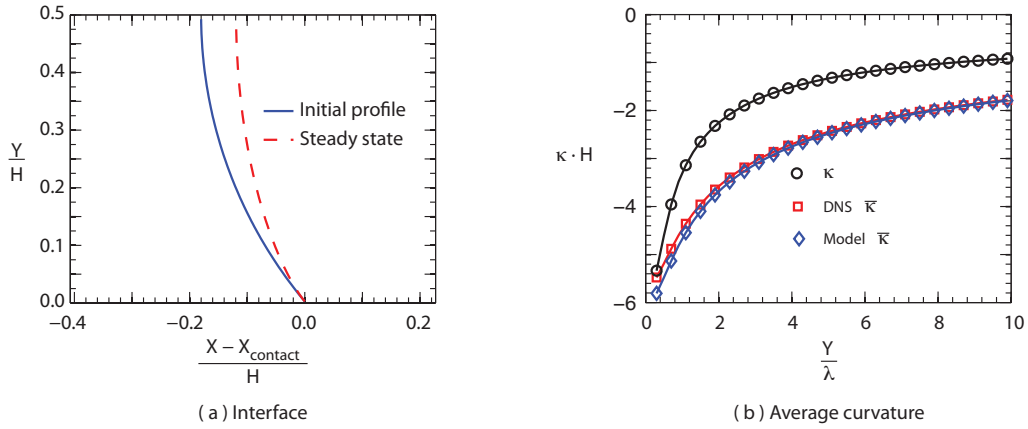

Figure 5.7: Results for $\epsilon = 1/40$, $\theta_S = 50^o$, and $Ca = 0.03$. a) Interfaces profiles at $t = 0$ and at steady state. b) The actual curvature κ at a given y location (black circles), the average curvature $\bar{\kappa}$ from the DNS (red squares), and the average curvature $\bar{\kappa}$ from Eq. 5.10 (blue diamonds). The x-axis of the plot is distance from the wall in slip lengths.

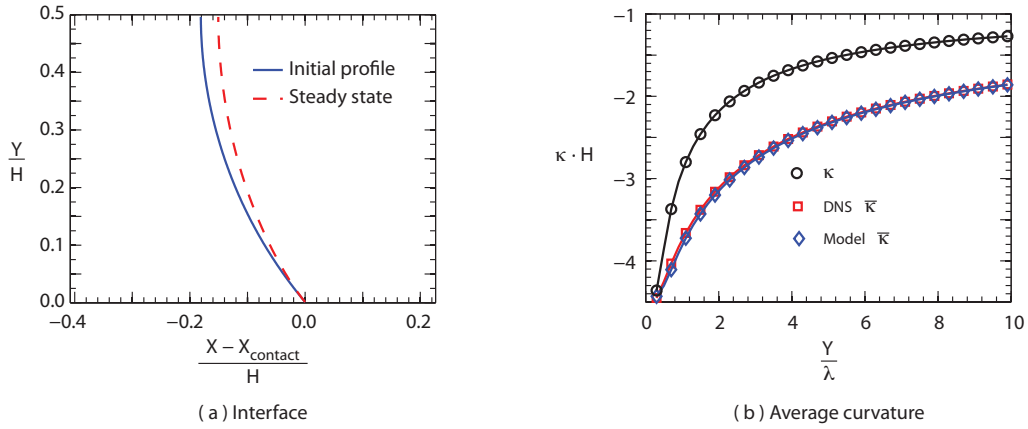

Figure 5.8: Results for $\epsilon = 1/80$, $\theta_S = 50^o$, and $Ca = 0.01$. a) Interfaces profiles at $t = 0$ and at steady state. b) The actual curvature κ at a given y location (black circles), the average curvature $\bar{\kappa}$ from the DNS (red squares), and the average curvature $\bar{\kappa}$ from Eq. 5.10 (blue diamonds). The x-axis of the plot is distance from the wall in slip lengths.

the y-momentum equation still uses the local curvature κ value, while the x-momentum equation uses the average curvature $\bar{\kappa}$. One small point should be noted; the apparent angle θ at the wall is actually calculated at the cell center where the level set ϕ is stored. Therefore, the average curvature is applied numerically as

$$\bar{\kappa} = \frac{cos\,(\theta) - cos\,(\theta_s)}{\frac{\Delta y}{2}} = 2\frac{cos\,(\theta) - cos\,(\theta_s)}{\Delta y} \tag{5.12}$$

5.5 Viscous shear (VS) model

In this section, the form of the viscous shear VS is first analyzed to determine the appropriate quantities to model. These quantities are then examined using the DNS data from Sec. 5.3 and approximate forms are suggested. The last subsection describes an implementation method for the viscous shear using an effective fluid viscosity.

5.5.1 Model derivation

The viscous shear term (Eq. 5.7) that needs to be modeled along the wall is

$$VS = \frac{1}{\Delta x}\Delta y \int_0^{\Delta x} \mu \frac{\partial u}{\partial y}|_B dx\,. \tag{5.13}$$

Let the interface be at location $x = a$ on the bottom wall (Fig. 5.2b). As before, this point is assumed sufficiently far from the filter edge that any velocity distortion due to the contact line is contained within the filter. Substituting in the Navier-slip boundary condition (Eq. 1.4) for $\partial u/\partial y$,

$$VS = \frac{1}{\Delta x}\Delta y \int_0^{\Delta x} \mu \frac{u}{\lambda} dx\,. \tag{5.14}$$

Assumption 7: The velocity tangential to the wall u can be expressed as the linear combination of a macroscopic bulk flow velocity u_B and a microscopic velocity perturbation u_S ($u = u_B + u_S$).

The viscous shear can now be expressed as

$$VS = \frac{1}{\Delta x}\Delta y \int_0^{\Delta x} \mu \frac{u_B}{\lambda} dx + \frac{1}{\Delta x}\Delta y \int_0^{\Delta x} \mu \frac{u_S}{\lambda} dx \; . \tag{5.15}$$

The first term is a macroscopic quantity. It does not need to be modeled and is calculated at the large length scale. It is therefore removed from the term VS and moved into the LHS. This removal is important to avoid "double counting" [132] viscous forces that might otherwise occur when the microscale model and the macroscale simulation are used simultaneously. Let $\hat{x}= x/\lambda$ and $\bar{u}_S= u_S/(U_{CL} - u_B)$ where U_{CL} is the contact line velocity. This non-dimensionalization makes the maximum value of $\bar{u}_S$ along the wall unity. As u_B represents the velocity along the wall far away from the contact line where the no-slip condition is nearly valid in the limit of small slip lengths, it is appropriate to assume

$$u_B \approx 0, \quad \bar{u}_S \approx \frac{u_S}{U_{CL}} \; . \tag{5.16}$$

With the prior considerations, the viscous shear becomes

$$VS = \frac{U_{CL}}{\Delta x \Delta y} \int_0^{\Delta x/\lambda} \mu \bar{u}_S d\hat{x} \; . \tag{5.17}$$

Splitting the integral into each fluid,

$$VS = \frac{U_{CL}}{\Delta x \Delta y} \left(\int_0^{a/\lambda} \mu_1 \bar{u}_S d\hat{x} + \int_{a/\lambda}^{\Delta x/\lambda} \mu_2 \bar{u}_S d\hat{x} \right) \tag{5.18}$$

For convenience, the integrals can be recentered at a/λ ($\bar{x}= (x - a)/\lambda$),

$$VS = \frac{\mu_1 U_{CL}}{\Delta x \Delta y} \left(\int_{-a/\lambda}^{0} \bar{u}_S d\bar{x} + \xi \int_0^{(\Delta x - a)/\lambda} \bar{u}_S d\bar{x} \right) \tag{5.19}$$

An example of $\bar{u}_S$ is shown in Fig. 5.9. The left curve ($\bar{x} < 0$, fluid 1) can be expressed as some function $\bar{u}_S = f(\bar{x}, Ca, \epsilon, \theta_S)$ while the right curve ($\bar{x} > 0$, fluid 2) is $\bar{u}_S = g(\bar{x}, Ca, \epsilon, 180^o - \theta_S)$. Regardless of Ca, ϵ, or θ_S, as $|\bar{x}| \to 0$ both functions approach 1 and as $|\bar{x}| \to \infty$ approach 0. This

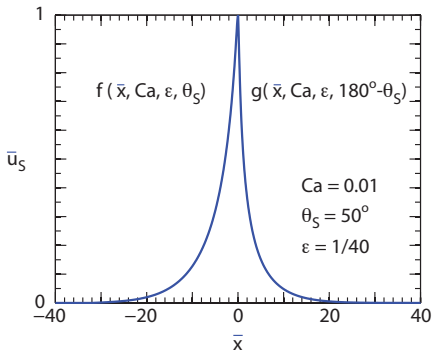

Figure 5.9: Example microscopic velocity $\bar{u}_S$ along the solid wall. f and g are functions for the left and right hand sides of the peak, respectively.

behavior suggests that the infinite integrals in Eq. 5.19 may be finite.

Assumption 8: Both $f(\bar{x}, Ca, \epsilon, \theta_S)$ and $g(\bar{x}, Ca, \epsilon, 180^o - \theta_S)$ have finite integrals.

Since $f(\bar{x}, Ca, \epsilon, \theta_S)$ and $g(\bar{x}, Ca, \epsilon, 180^o - \theta_S)$ should be exactly zero after a certain distance from the contact line, this assumption is valid. As long as $\lambda << \Delta x$ (Assumption 4) and a is not near the filter edges, the integrals in Eq. 5.19 can be replaced by their infinite counterparts with only a small approximation error,

$$VS = \frac{\mu_1 U_{CL}}{\Delta x \Delta y} \left(\int_{-\infty}^{0} f(\bar{x}, Ca, \epsilon, \theta_S) d\bar{x} + \xi \int_{0}^{\infty} g(\bar{x}, Ca, \epsilon, 180^o - \theta_S) d\bar{x} \right) \tag{5.20}$$

In the special case when $\Delta x \to \lambda$, the integral bounds would need to be included in order to cause the source term VS to vanish. The grid dependence of the integrals in this limit is not considered here. If $\Delta x >> \lambda$, the exact functions $f(\bar{x}, Ca, \epsilon, \theta_S)$ and $g(\bar{x}, Ca, \epsilon, 180^o - \theta_S)$ do not need to be known, but only their integrals F and G,

$$F\,(Ca, \epsilon, \theta) = \int_{-\infty}^{0} f(\bar{x}, Ca, \epsilon, \theta) d\bar{x} \tag{5.21}$$

$$G\,(Ca, \epsilon, \theta) = \int_{0}^{\infty} g(\bar{x}, Ca, \epsilon, \theta) d\bar{x}\ . \tag{5.22}$$

The resulting expressions for the term that needs to be modeled is

$$VS = \frac{\mu_1 U_{CL}}{\Delta x \Delta y} \left[F\left(Ca, \epsilon, \theta_S\right) + \xi G\left(Ca, \epsilon, 180^o - \theta_S\right) \right] . \tag{5.23}$$

F and G are hereafter referred to as the shear factors. The data processing procedure to calculate the shear factors F and G is described in appendix C.

5.5.2 Viscous shear from DNS

The compilation of all the numerical shear factors F and G is shown in Fig. 5.10. For a given static contact angle θ_S, the F points (squares) are when $\theta = \theta_S$ and the G points (circles) are when $\theta = 180^o - \theta_S$. The analysis is divided into three sections. Section 5.5.2.1 discusses the relative values of F and G. These variables are nearly equal. The shear factors' dependence on capillary number Ca is then examined in Sec. 5.5.2.2 and the dependence on the slip length ratio ϵ and static contact angle θ_S is explored in Sec. 5.5.2.3.

5.5.2.1 Shear factors F and G

The shear factors appear to form smooth curves in θ for fixed Ca and ϵ. In most cases, $F \approx G$. This similarity is worse as slip length ratio ϵ decreases, capillary number Ca increases, or the contact angle θ decreases. Since θ_{app} differs more from the static contact angle θ_S in these ways, the asymmetry of F and G is not surprising because the interface is more distorted; the viewpoints of the advancing and receding contact lines have different interfaces. Symmetry will apply if the viewpoints have the same interface.

Assumption 9: $F = G$.

This assumption greatly simplifies the analysis and increases the amount of data available for averaging. For most values in Fig. 5.10a and Fig. 5.10b, this assumption seems accurate; however, at higher capillary number Ca (Fig. 5.10c), it may not be valid. This last data set ($Ca = 0.03$) is particularly hard to analyze because F or G is unavailable at the edge angles; the maximum simulated static contact angle θ_S simulated was 110^o (appendix B) because a liquid film would be

entrained at these high velocities ($\theta_{app} \to 180^o$).

5.5.2.2 Variation with capillary number *Ca*

In order to analyze the capillary number Ca effects, let γ be the ratio of the shear factors at a given value of ϵ and θ, but differing capillary numbers. The values of γ comparing $Ca = 0.0033$ against $Ca = 0.01$ and $Ca = 0.01$ against $Ca = 0.03$ are shown in Fig. 5.11. Despite the capillary numbers varying by a factor of three, the ratios γ have a much smaller spread. Since γ is nearly always between 0.9 and 1.1, F (or G) is nearly independent of Ca.

Assumption 10: F and G are independent of capillary number Ca.

This assumption makes the viscous shear VS vary linearly with the contact line velocity U_{CL}. The remaining shear factor analysis will only use the intermediate capillary number $Ca = 0.01$, Fig. 5.10b.

5.5.2.3 Variation with slip length ratio ϵ and static contact angle θ_s

The asymptotic hydrodynamic theory (Eq. 1.5) suggests that the viscous terms may only have a weak, logarithmic dependence on the slip length ratio ϵ. Plotting the data for $\theta_S = 50^o$ (Fig. 5.12), F (or G) appears linear which indicates a power-law dependence on the slip length ratio ϵ. The power-law exponent is determined by the angle θ. The relationship found here is stronger than the logarithmic dependence of hydrodynamic theory. For a power law, the form of F can be approximated as

$$F(\epsilon, \theta) = A(\theta)\epsilon^{B(\theta)} \tag{5.24}$$

where $A(\theta)$ and $B(\theta)$ are unknown functions of the contact angle θ.

$B(\theta)$ is approximated first because it can be easily evaluated by taking the ratio of two shear factors at different values of ϵ and constant θ. The four values of $B(\theta)$ from F and G in Fig. 5.10b at a given θ are averaged together to create the curve in Fig. 5.13a. This curve for $B(\theta)$ has an

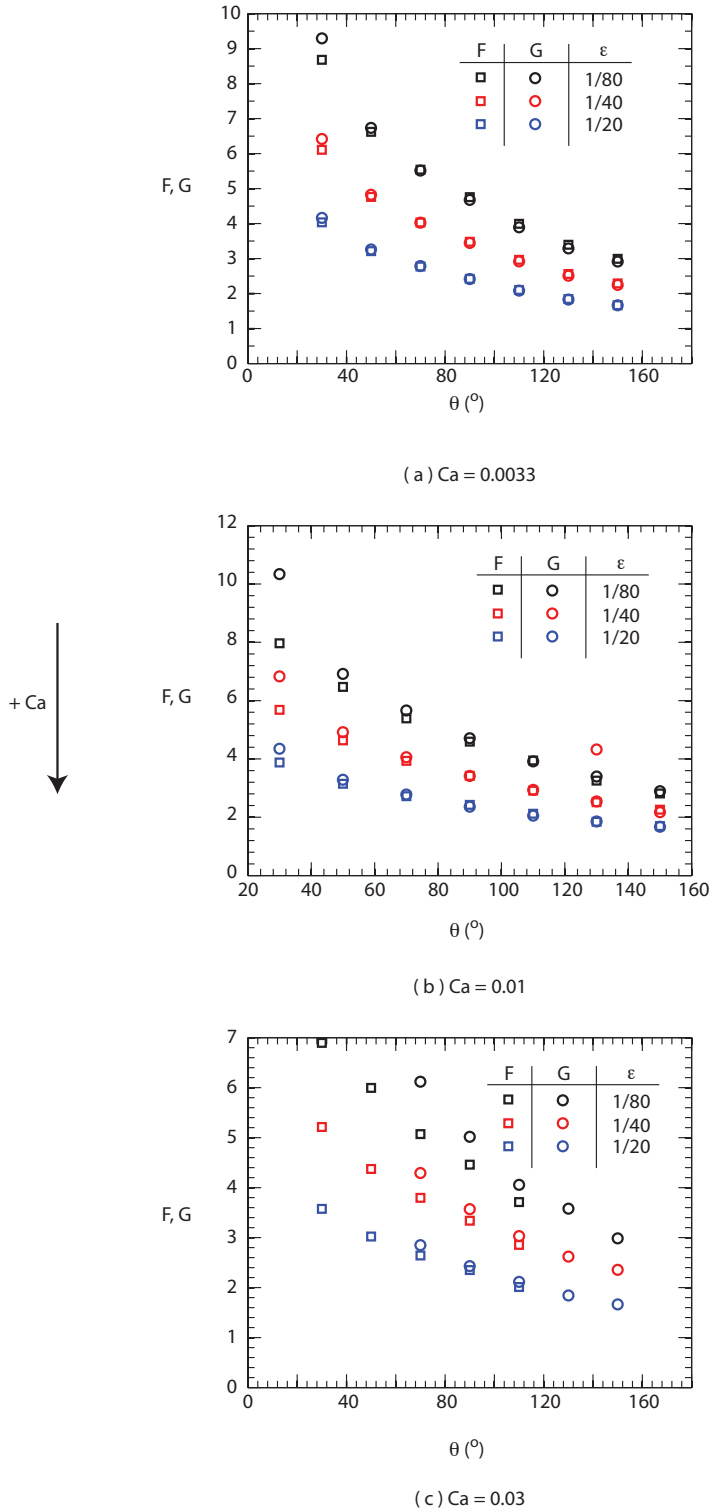

Figure 5.10: Diagrams of the integrated quantities F (squares) and G (circles) as functions of contact angle θ, slip length ratio ϵ, and capillary number Ca. Colors denote different values of the slip length ratio ϵ. The different figures are different Ca : a) $Ca = 0.0033$, b) $Ca = 0.01$, c) $Ca = 0.03$.

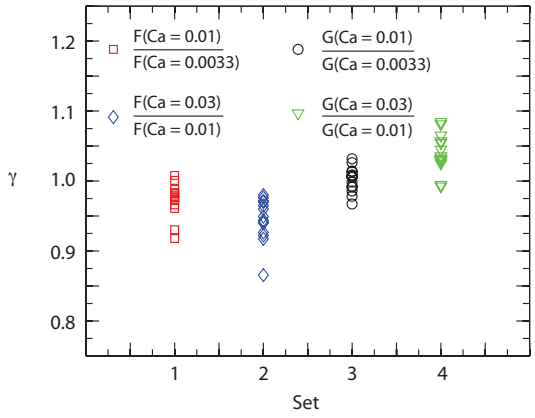

Figure 5.11: Ratios γ of the data in Fig. 5.10 for all data sets. The set definitions are: Set 1 (red squares) = ratio of F in Figs. 5.10b and 5.10a, Set 2 (blue diamonds) = ratio of F in Figs. 5.10c and 5.10b, Set 3 (black circles) = ratio of G in Figs. 5.10b and 5.10a, Set 4 (green triangles) = ratio of G in Figs. 5.10c and 5.10b.

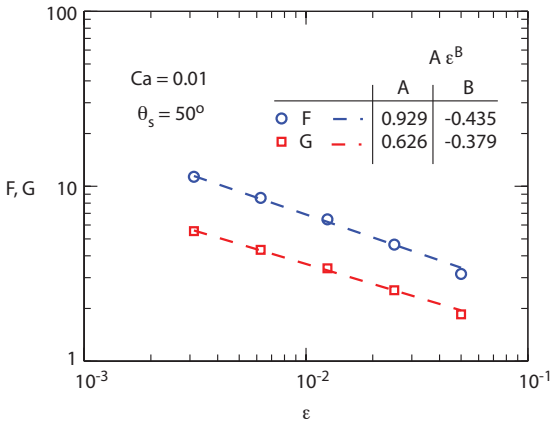

Figure 5.12: Value of F and G as a function of slip length ratio ϵ for $\theta_S = 50^o$ and $Ca = 0.01$. The lines are a power-law fit $A\epsilon^B$ to the data.

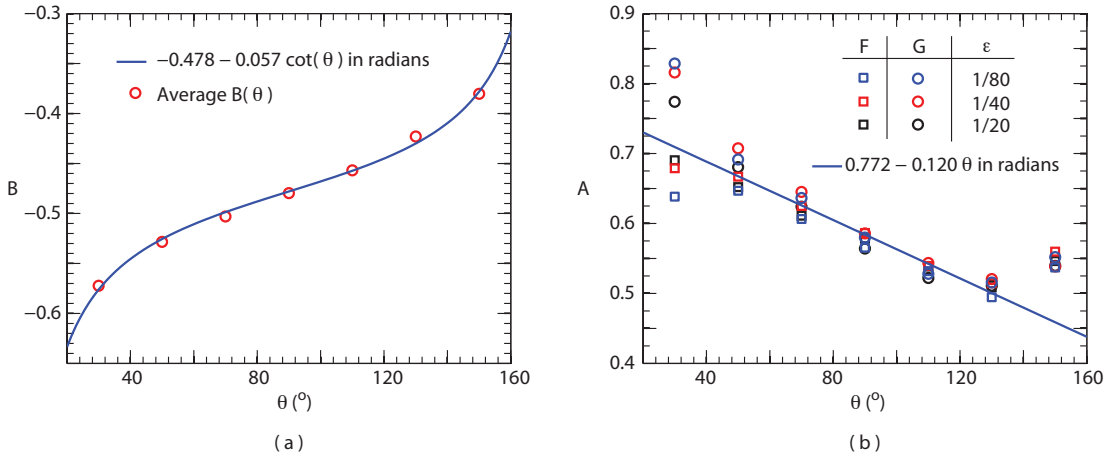

Figure 5.13: a) Approximate value of $B(\theta)$ from the data in Fig. 5.10b. b) Approximate value of $A(\theta)$ after $B(\theta)$ is removed from F (squares) and G (circles).

inflection point at $\theta = 90^o$ and is well approximated by the function

$$B(\theta) = -0.478 - 0.057cot(\theta)\ . \tag{5.25}$$

Factoring out ϵ^B from the shear factors yields $A(\theta)$ (Fig. 5.13b). Excluding the extreme angles ($\theta = 30^o, 150^o$), the function $A(\theta)$ is almost linear. These end values of θ may be poorly represented by Eq. 5.24 for two reasons. First, Fig. 5.10b, the data source, had a large spread in F and G at $\theta = 30^o$; the distortions in Fig. 5.13b could be a direct result of this spread. Second, the grid cells used in the DNS were square; neither an angle of 30^o nor 150^o may be well represented on such meshes. Nonetheless, the relationship found seems very good for angles θ close to 90^o. The model viscous shear source term is

$$VS = -\frac{\mu_1 U_{CL}}{\Delta x \Delta y}\left(F(\epsilon, \theta_S) + \xi F(\epsilon, 180^o - \theta_S)\right) \tag{5.26}$$

where

$$F(\epsilon, \theta) = (0.772 - 0.12\theta)\epsilon^{-0.478-0.057cot(\theta)}\ . \tag{5.27}$$

The viscous shear term is added to the right-side of the Navier-Stokes equations for the node nearest

the contact line. For a wall in the positive y-direction, this term would have opposite sign.

Assumption 11: Although the viscous shear term VS is derived from a small range of large values ϵ, it also holds for smaller slip length ratios ϵ.

This assumption allows the model to be extended to the region of small slip lengths λ. More fully resolved simulations may be needed to confirm the form proposed.

5.5.3 Model implementation

The slip length ratio ϵ is expected to be very small ($< 10^{-4}$) for most realistic simulations. This small slip length ratio yields two practical considerations.

First, a no slip boundary condition ($u_{wall} = 0$) can be used instead of a Navier-slip boundary condition with small error. To calculate $\partial u/\partial y$ for a node P at the top of the box in Fig. 5.2b, the formulation for a no slip condition is

$$\left(\frac{\partial u}{\partial y}\right)_P = \frac{2}{\Delta y} U_P \tag{5.28}$$

while the equation for a Navier-slip boundary condition is

$$\left(\frac{\partial u}{\partial y}\right)_P = \frac{2}{\Delta y + \lambda} U_P \ . \tag{5.29}$$

where U_P is the x-velocity component at point P. Thus, the two expressions are nearly identical if $\lambda << \Delta y$ ($\epsilon << 1$). This change is important to simplify the application of the viscous shear VS.

Second, since $B(\theta)$ is a negative exponent (Fig. 5.13a), the value of VS can be very large for small ϵ. As a result, the source term for VS cannot be easily applied in an explicit fashion. While there are many implicit approaches for the linear relationship between VS and Ca, one option is to modify the corner viscosity (Eqs. 2.14 and 2.16) appropriately.

$$\mu_{eff} = \mu + \frac{\mu_1}{2}\frac{\Delta y}{\Delta x}\left(F\left(\epsilon, \theta_S\right) + \xi F\left(\epsilon, 180^o - \theta_S\right)\right) \tag{5.30}$$

This effective viscosity μ_{eff} is the sum of the viscosity calculated using Eqs. 2.14 and 2.16 and a viscous shear component. If μ_{eff} is applied for the shear stress term near the contact line, the viscous shear VS is automatically accounted for; this compact form requires minimal modification to existing variable-viscosity, computational frameworks. Most such frameworks will already be capable of handling the viscous terms in the Navier-Stokes equations implicitly. An important point to note about the effective viscosity μ_{eff} is the cell ratio $\Delta y/\Delta x$. If the wall was in the y-direction (vertical) instead of the x-direction (horizontal), this ratio would be flipped.

5.6 Summary

Two terms in the volumetric-filtered Navier-Stokes equations, the average curvature and the viscous shear VS, were identified as important when the grid size Δx is much larger than the slip length λ. A large number of DNS at different capillary number Ca, slip length ratio ϵ, and static contact angle θ_S was used to create models for each term. The average curvature is well represented by assuming a constant curvature transition between the static angle θ_S at the wall and the apparent angle θ a distance Δy from the wall. A power law in the slip length ratio ϵ with functions of contact angle θ_S was proposed to model the viscous shear term. This relationship has reasonable agreement for contact angle around 90^o, but may have difficulty when $\theta_S < 45^o$ or $\theta_S > 135^o$. Now that source terms have been derived to represent the contact-line physics on coarse meshes, realistic capillary fluid flows can be simulated with very small slip length ratios ϵ. The following chapter uses these models for the difficult case of a drop impacting a wall and a static contact angle $\theta_S = 90^o$.

Chapter 6

Experimental comparison: drop impact

All models are wrong, some models are useful.

— George Box

6.1 Introduction

The prior three chapters established a computational framework with volumetric source terms for contact-line physics: this framework is used in this chapter to simulate a water drop impacting a partially-wetting surface ($\theta_S = 90^o$). While there are many types of contact-line experiments, four common configurations are flow in a capillary tube [44, 65], drop spreading [9, 47, 149], plunging tapes [21], and droplet impacts [11, 49, 156, 166]. Capillary tube experiments have flows driven at a known velocity or pressure; the steady or quasi-static interface shape is then photographed. These experiments are typically performed at low capillary number Ca and Reynolds number Re. The second case, drop spreading, has a drop carefully placed on a surface and then the drop spreads by capillary forces. Again, these flows are generally slow (small Ca) and not all contact angles are appropriate for this spreading (a wetting fluid should be used). In some cases, the fluid interface is a collection of quasi-static, nearly circular arcs. Plunging tape experiments can have high capillary numbers Ca and Reynolds numbers Re. This case starts to bring the inertial fluid effects into the problem; these effects should be captured well in the framework proposed here because the inertial

terms do not need to be explicitly modeled. However, a 3D, V-shape air film may form in these tests [21], which would necessitate a 3D simulation. Finally, droplet impacts are the worst case scenario: not only is the impact itself difficult to capture numerically, but the contact angle is varying in space, the Reynolds number Re and capillary number Ca can be large during the spreading process, and the drop is highly deformed. The impacting, spreading, and recoiling process contains elements of the three prior cases because of the variation in contact-line velocity throughout the experiment. Furthermore, additional physical effects such as gravity may be important. The drop impact would show the ability of the present method to capture the high Reynolds number effects. Since this scenario is the most challenging, if the framework can capture the spreading behavior for it, the framework would likely work well in other types of experiments.

The work of Yokoi et al. [166] is a comparison of numerical simulations with experimental data (Fig. 6.1a). They found that the experimental behavior was only recovered if their experimentally derived contact law (which they described as model I) was used in the simulations. Other models tested were variants of model I except for model II, where the contact angle is fixed at the static value, $\theta_S = 90^o$. Model II caused the drop to have an exaggerated maximum contact diameter, eject a droplet away from the substrate during the recoil process, and oscillate far longer in time, $t_{end} > 100\ ms$. The main conclusion of that study was the apparent contact angle must be modeled accurately to predict drop impact characteristics.

Model I of Yokoi et al. [166] is

$$\theta(U_{CL}) = \begin{cases} min\left[\theta_S + \left(\frac{Ca}{k_a}\right)^{1/3}, \theta_{mda}\right] & \text{if } U_{CL} \geq 0 \\ max\left[\theta_S + \left(\frac{Ca}{k_r}\right)^{1/3}, \theta_{mdr}\right] & \text{if } U_{CL} < 0 \end{cases} \tag{6.1}$$

where θ_{mda} is a maximum advancing contact angle, θ_{mdr} is a minimum receding contact angle, k_a is a material-related advancing parameter, and k_r is a material-related receding parameter. While this model led to good predictions (Fig. 6.1a) and established compelling evidence for the ne-

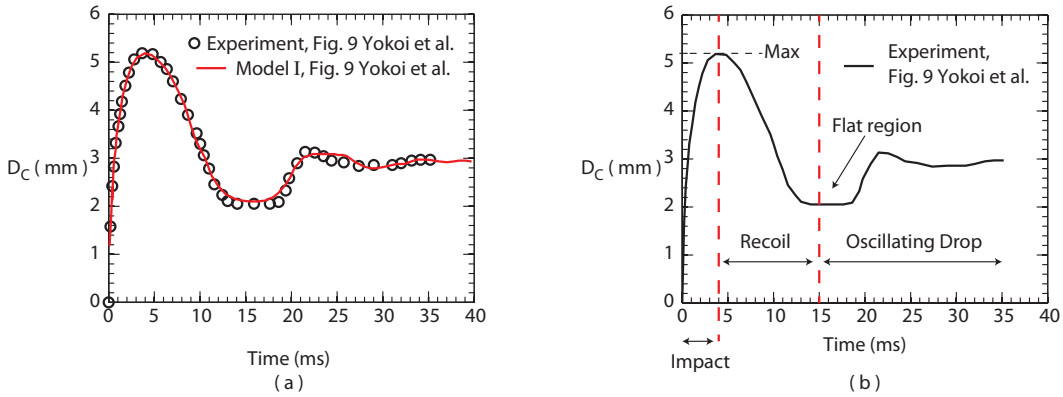

Figure 6.1: a) Numerical drop contact diameter D_C in time t for model I compared to the experimental data from Fig. 9 in Yokoi et al. [166]. b) Labeled features for the drop impact process.

cessity of correctly capturing contact angle behavior, there are questions about the generality of their approach. First, there are four fitted parameters to the experimental data, which may over-parametrize the problem. It may be argued that their agreement was a consequence of using the resulting dynamic solution and not fundamental physical quantities. Second, if $\theta_{mdr} < \theta < \theta_{mda}$, the hydrodynamic theory applied, $Ca = k(\theta - \theta_S)^3$, has no physical justification according to one of the references they cited [131]. However, there are two similar equations that do have physical justification: $Ca = k\theta(\theta^2 - \theta_S^2)$ from lubrication theory [20, 30] or the Hoffman-Voinov-Tanner law $Ca = k(\theta^3 - \theta_S^3)$ [13, 14, 135]. These other equations may be more appropriate in a physical sense than the relationship used. Third, Yokoi et al. use a no slip condition: even if the slip length is much smaller than the mesh size, it cannot be ignored for solution convergence [4, 137]. Without the viscous shear term VS (Sec. 5.5), it is not surprising that their model II did not lose enough energy and, therefore, ejected a droplet away from the wall. Their experimentally fitted contact angle law (model I) showed good agreement to the experiment and grid convergence because it compensated for this missing flow resistance. The present work is more general and fundamental than their prior work.

Section 6.2 describes the experimental data used in Yokoi et al. [166] and the present work. For simplicity, Yokoi et al. [166] will be referred to as YVHH throughout this chapter. The simulations

for different configurations of the average curvature and viscous shear are compared to the experimental data in Sec. 6.3. Contact angle hysteresis is introduced in this section and good agreement to the experimental contact diameter is shown when using the slip length ratio ϵ as the only fitted parameter. The apparent contact angle law is not imposed directly. Section 6.4 discusses the final simulation results and considers the discrepancies. The chapter concludes with a summary in Sec. 6.5.

6.2 Experimental setup

The experimental drop data in YVHH (Fig. 9 in Ref. [166], Fig. 6.1b) is used for comparison. The original experimental data comes from one of the authors' thesis [155]. YVHH reported an experimental, quantitative contact (splat) diameter D_C in time for the impact and recovery process of a water droplet (Fig. 6.1b). The initial period ($t \approx 0 - 4\ ms$) is the drop impact after which the drop reaches its maximum contact diameter. The drop then recoils ($t \approx 4 - 15$) and reaches a point where the drop contact diameter temporarily stabilizes - the flat region in Fig. 6.1b. Finally, the drop oscillates until it reaches a stable, nearly circular cap. It is important to note that the slopes $\partial D_C/\partial t$ are asymmetric for the drop impact and recoil regions. The Reynolds number Re, Bond number Bo, and Weber number We for water are 1140, 0.177, and 15.8, respectively. The first two numbers indicate that inertial effects are more important than viscous effects and surface tension dominates over gravity. The Weber number is moderate; while surface tension is not important during the initial impact, it is important later once the drop is on the surface and slows down.

6.3 Numerical results

A collection of droplet impact simulations are conducted with different contact angles in the average mean curvature (Eq. 5.12) and the viscous shear VS (Eq. 5.26). These equations have x and y replaced by r and z respectively. Table 6.1 is a summary of the different cases for quick reference.

Fig. #	Average mean curvature, Eq. 5.12	Viscous shear VS, Eq. 5.26 / Eq. 6.3
6.3	$\theta_S = 90^o$	$\beta = 0$
6.5	$\theta_S = 90^o$	$\beta = 100,\ 200,\ 300,\ 400$
6.7	$\theta_{sr} = 77^o / \ \theta_{sa} = 107^o$	$\theta_S = 90^o \quad \epsilon = 10^{-5},\ 2 \cdot 10^{-5},\ 4 \cdot 10^{-5}$
6.8	$\theta_S = 90^o$	$\theta_{sr} = 77^o / \ \theta_{sa} = 107^o \quad \epsilon = 5 \cdot 10^{-6},\ 10^{-5},\ 2 \cdot 10^{-5}$
6.9	$\theta_{sr} = 77^o / \ \theta_{sa} = 107^o$	$\theta_{sr} = 77^o / \ \theta_{sa} = 107^o \quad \epsilon = 2 \cdot 10^{-5}$

Table 6.1: Simulation inputs for the average mean curvature and viscous shear VS.

6.3.1 Configuration

The drop impact domain is shown in Fig. 6.2. A no slip boundary condition wall is present at the bottom ($z = 0$) and top ($z = H$) of the domain. The initially circular drop has a radius of R= 1.14 mm and an initial velocity of $U_i = 1\ m/s$ towards the bottom wall to match the experimental conditions. The drop starts at a height $X_S = 1.02R$ such that the initial shape is not touching the bottom wall. Material parameters are given in Fig. 6.2. The equilibrium contact angle from the experiment is $\theta_S = 90^o$, but the contact angle hysteresis angles are $\theta_{sr} = 77^o$ and $\theta_{sa} = 107^o$. The domain dimensions are L= $4R$ and H= $4R$ (except in Sec. 6.3.2 where $H = 10R$). The outer cylindrical boundary has a zero Neumann boundary condition for velocity in the r-direction and zero velocity in the z-direction.

The domain is discretized with square grid cells $\Delta r = \Delta z = R/50$. The SMG solver is used to solve the fluid pressure with a maximum number of 10 iterations and a relative convergence tolerance of 10^{-7} [80]. The average curvature and viscous shear VS are applied using the procedures outlined in Sec. 5.4.3 and 5.5.3. Since the viscous shear is formulated as the effective viscosity μ_{eff}, the viscosity terms in the Navier-Stokes equations (Eq. 2.1) are solved implicitly. The simulation has a surface tension CFL number of 0.05 using the criterion of Eq. 2.20. The reinitialization relaxation equation is applied every ten time steps. The simulations typically runs for less than 12 hours on one 12-core Intel Xeon CPU node.

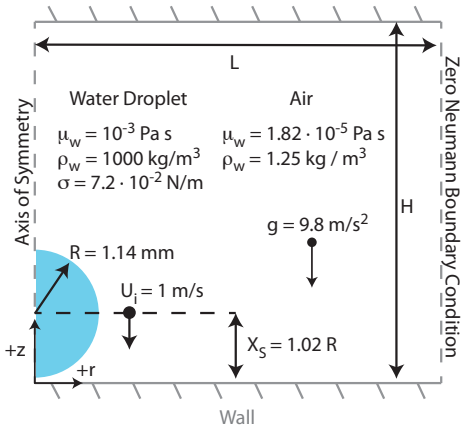

Figure 6.2: Cylindrical geometry for a droplet impacting on a flat wall (not drawn to scale). The two fluids are water (droplet) and air (surrounding fluid) with the given properties. The droplet has an initial velocity U_i in the negative z-direction and an initial distance X_S from the wall. Gravity is oriented in the negative z-direction. The walls at the top and bottom of the domain have no slip velocity boundary conditions.

For convenience, the shear factor β is sometimes quoted instead of the shear factor F where

$$\beta\left(\xi,\epsilon,\theta\right) = F\left(\epsilon,\theta\right) + \xi F\left(\epsilon, 180^o - \theta\right) \ . \tag{6.2}$$

and

$$VS = -\frac{\mu_1 U_{CL}}{\Delta r \Delta z}\beta \ . \tag{6.3}$$

This notation has the merit of simplifying the comparison of numerical results and experimental values for a single contact angle θ.

The experimental error on the contact diameter is reported as $\pm 2\%$ in YVHH. This range is roughly the size of the black circles with which the data set is drawn in subsequent figures.

6.3.2 Static contact angle θ_S without viscous shear

Similar to model II in YVHH, the first test case uses the static contact angle $\theta_S = 90^o$ in the average curvature $\bar{\kappa}$, but no viscous shear is included. This case is not physical and is intended to demonstrate the necessity of the viscous shear VS. The side contour of the water (2D) and a

3D visualization for this case is shown in Fig. 6.4. The contact diameter D_C in time is plotted in Fig. 6.3. Like model II of YVHH, the maximum contact diameter is too large, a satellite droplet is ejected during the recoil process, and the drop oscillates far longer than the experiment. An interesting feature is the kink that occurs around $t \approx 25\ ms$ (Fig. 6.3). This kink corresponds to the formation of a "mushroom" shape when the fluid pinches, but does not have enough energy to eject a droplet and thus the bulge crashes down while, at the same time, almost detaching from the wall. This feature occurs in later curves and is indicative of insufficient viscous shear. The satellite drop impacts the top wall and sticks there; this particular feature is an artifact of the finite domain size.

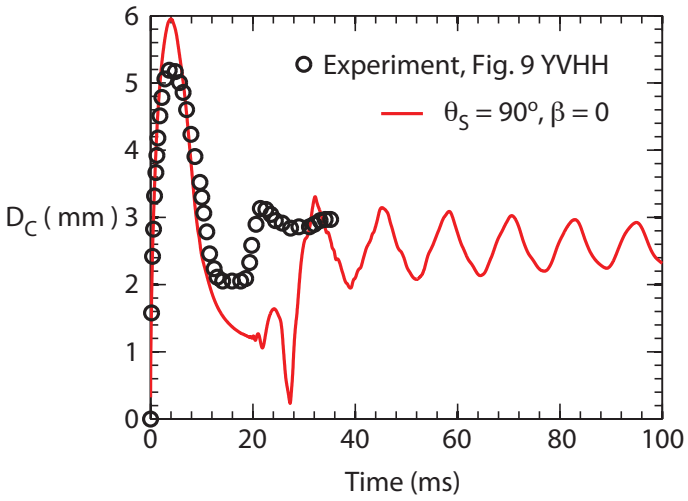

Figure 6.3: Drop contact diameter D_C in time t for a set static contact angle of 90^o in the average curvature $\bar{\kappa}$ and no additional viscous shear VS. The black dots are the experimental data of Fig. 9 in YVHH.

6.3.3 Static contact angle θ_S with viscous shear

It is clear from Fig. 6.3 that some amount of viscous shear VS (energy loss) is necessary to match experiments. The curves in Fig. 6.5 are the contact diameter in time for increasing amounts of the shear factor β. The curve $\beta = 100$ (red) matches the maximum splat diameter well, but there is not enough dissipation in the later recoil stage as evidenced by the kink (mushroom formation) at $t \sim 28$. Increasing the shear factor β reproduces better the frequency of the oscillating drop, but does not

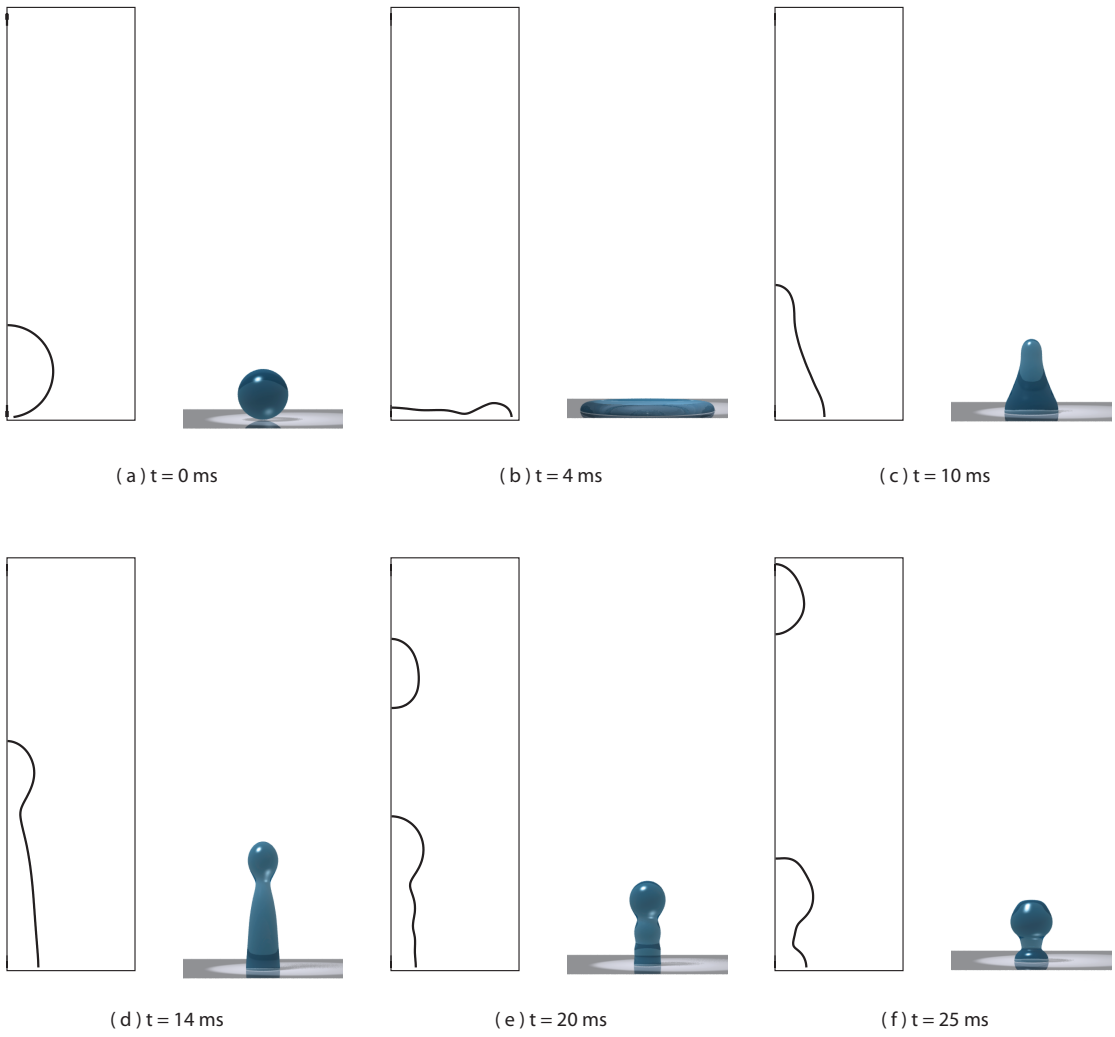

Figure 6.4: Cross-section and revolved surfaces for the water droplet with a set static contact angle of 90^o in the average curvature $\bar{\kappa}$ and no additional viscous shear VS. The 2D and 3D images are not the same scale. The 3D images are taken at a slight angle relative to the side profile and do not include the satellite droplet.

capture the correct maximum diameter. Only the diameter peak or the oscillation frequency can be captured. Furthermore, the flat region in the experimental data after recoil is not present; all of the valleys in the curves of Fig. 6.5 are rounded. There is still some physical component missing.

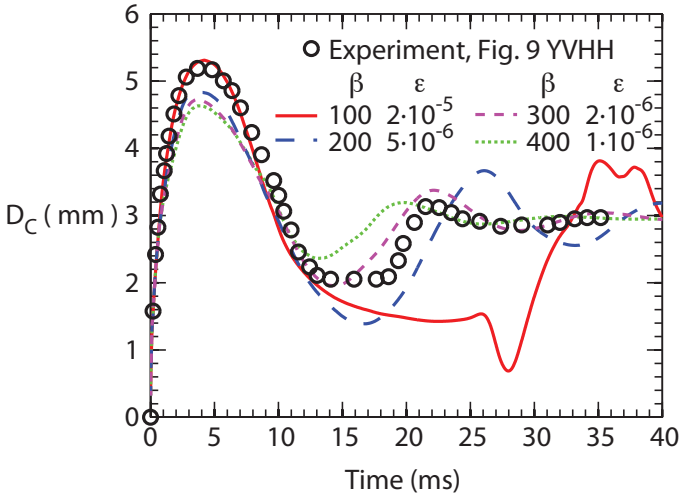

Figure 6.5: Drop contact diameter D_C in time t for a set static contact angle of 90^o in the average curvature $\bar{\kappa}$ at different values of the shear factor β. Approximate values of the slip length ratio ϵ are given with each value β. The black dots are the experimental data of Fig. 9 in YVHH.

6.3.4 Contact angle hysteresis

The experimental drop impact had measurable contact angle hysteresis ($\theta_{sr} = 77^o$, $\theta_{sa} = 107^o$). As mentioned in the introduction to Chap. 5, these angles can be used instead of the static contact angle θ_S with identical results for the average curvature and viscous shear representation. For the application of the contact angle hysteresis, the static contact angle was set as

$$\theta_S = \begin{cases} \theta_{sa} & \text{if } U_{CL} \geq 0 \\ \theta_{sr} & \text{if } U_{CL} < 0 \end{cases} \tag{6.4}$$

in Eqs. 5.12 and 5.26. These hysteresis angles will have different values of the viscous shear VS through the shear factor F (Eq. 5.27) at a fixed slip length ratio ϵ. Figure 6.6 shows a graph of the shear factor F for the different angles as functions of the slip length ratio ϵ. A large difference

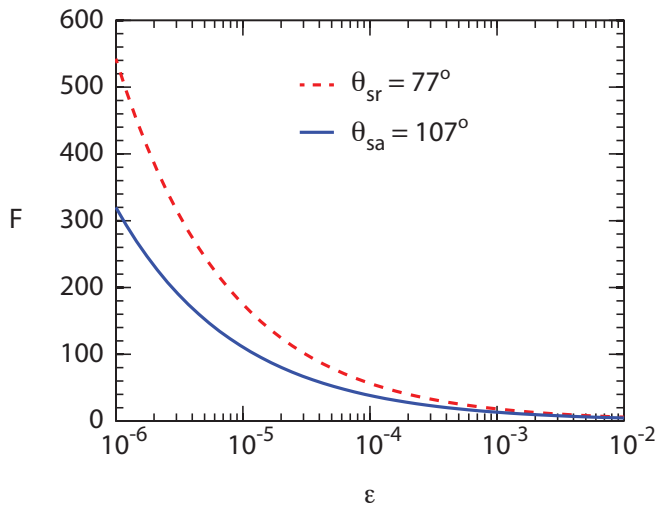

Figure 6.6: Shear factor F (Eq. 5.27) as a function of the slip length ratio ϵ for the static advancing and receding angles. Note: the x-axis is logarithmic.

appears as $\epsilon \to 0$ which could explain the asymmetric slopes near the experimental data's peak ($t \approx 4\ ms$ in Fig. 6.1b). The variants of the contact angle hysteresis are contact angle hysteresis in the average mean curvature only (Fig. 6.7), contact angle hysteresis in the shear factor F only (Fig. 6.8), and both applied (Fig. 6.9). When contact angle hysteresis is used for the average mean curvature, the flat regions after recoil appear in the contact diameter curves (Fig. 6.7) and the energy is reduced. The contact angle hysteresis in the viscous shear VS creates more asymmetric curves and captures better the maximum splat diameter (Fig. 6.8). Only when both pieces are added together does a faithful representation of the experimental data form (Fig. 6.9). A profile comparison of the drop at different times is shown in Fig. 6.10. Qualitatively, the overall drop shapes are correct. Quantitatively, the behavior is not quite as good as YVHH model I (Fig. 6.9), particularly for the maximum splat radius. However, model I involved 4 fitted parameters; there is only one approximated parameter, $\epsilon = 2 \cdot 10^{-5}$ in the approach of this work.

6.4 Discussion

It is remarkable given the many assumptions in Chap. 5 (Tab. 6.2) that the model gives such good agreement. Even more surprising, using the initial drop radius R as the large length scale in

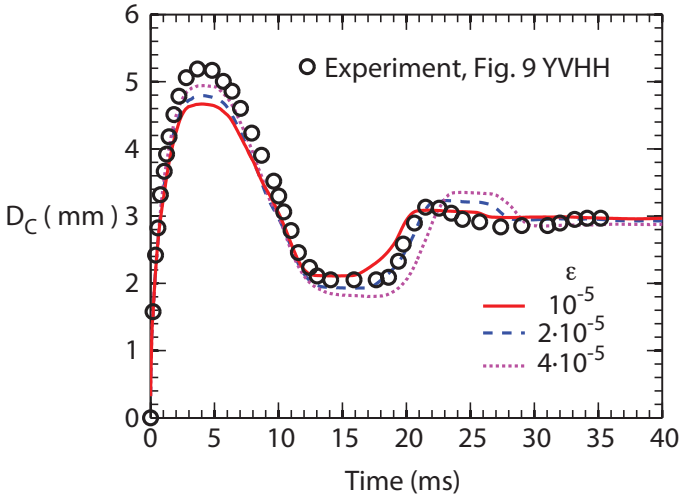

Figure 6.7: Drop contact diameter D_C in time t for a set contact angle hysteresis angles $\theta_{sa} = 107^o$, $\theta_{sr} = 77^o$ in the average curvature $\bar{\kappa}$ and a set shear factor β. The black dots are the experimental data of Fig. 9 in YVHH.

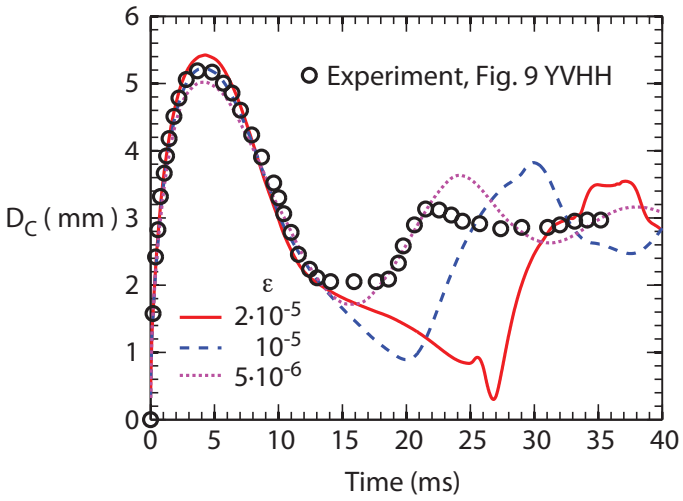

Figure 6.8: Drop contact diameter D_C in time t for a set static contact angle of 90^o in the average curvature $\bar{\kappa}$ and the contact angle hysteresis angles $\theta_{sa} = 107^o$, $\theta_{sr} = 77^o$ in the shear factor F. The black dots are the experimental data of Fig. 9 in YVHH.

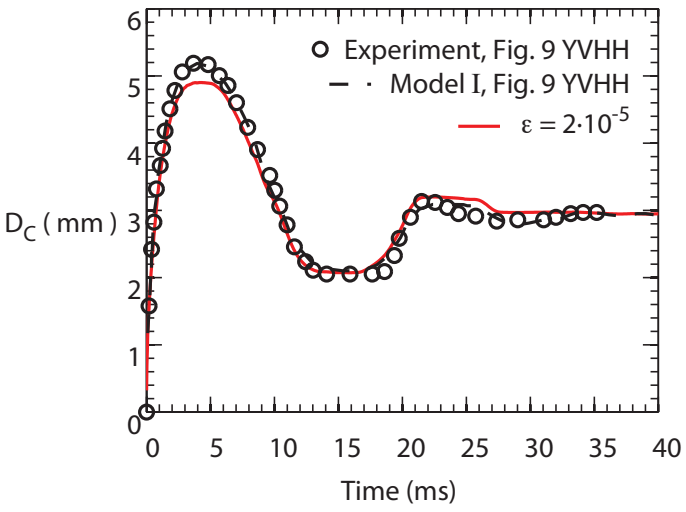

Figure 6.9: Drop contact diameter D_C in time t using the contact angle hysteresis angles $\theta_{sa} = 107^o$, $\theta_{sr} = 77^o$ in the average curvature $\bar{\kappa}$ and the shear factor F. The black dots and black dashed line are the experimental data and model I data from Fig. 9 in YVHH, respectively.

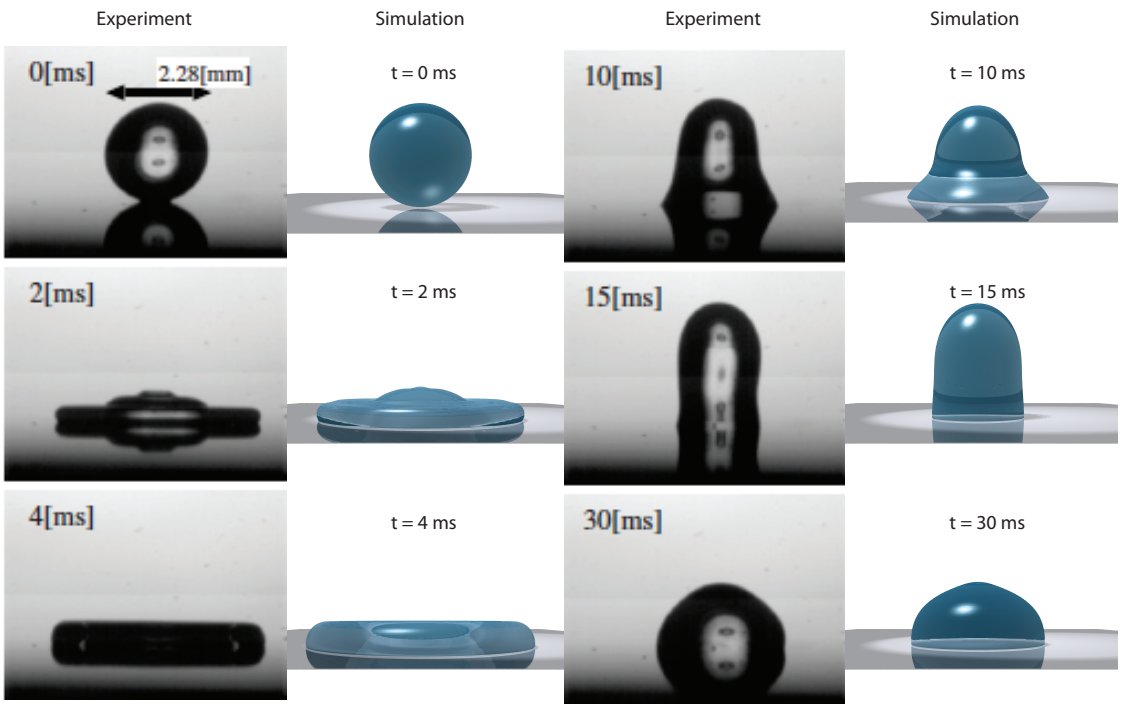

Figure 6.10: Drop images from Fig. 8 in YVHH compared to simulation images from Fig. 6.9 at t = 0, 2, 4, 10, 15, and 30 ms. The camera for images is at a slight angle to mimic the reflection observed in the experimental images. The experimental images are reproduced with permission under license 3375611208717.

Assumption 1: A Navier-slip boundary condition.

Assumption 2: A fixed contact angle at the wall.

Assumption 3: Continuum fluid mechanics can be used at the slip length scale.

Assumption 4: The averaging volume dimensions are much larger than the slip length, $\lambda << \Delta x, \Delta y$.

Assumption 5: $\nabla \bar{P}^y$ is the same on both sides of the interface.

Assumption 6: The fluid interface smoothly transitions from a contact angle θ at $y = \Delta y$ to the static contact angle θ_S at $y = 0$.

Assumption 7: The velocity tangential to the wall u can be expressed as the linear combination of a macroscopic bulk flow velocity u_B and a microscopic velocity perturbation u_S ($u = u_B + u_S$).

Assumption 8: Both $f(\bar{x}, Ca, \epsilon, \theta_S)$ and $g(\bar{x}, Ca, \epsilon, 180^o - \theta_S)$ have finite integrals.

Assumption 9: $F = G$.

Assumption 10: F and G are independent of capillary number Ca .

Assumption 11: Although the viscous shear term VS is derived from a small range of large values ϵ, it also holds for smaller slip length ratios ϵ.

Table 6.2: Assumptions in Chap. 5

$\epsilon = 2 \cdot 10^{-5}$, the predicted slip length λ is 25 nm. The substrate roughness in the experiments was specifically stated as less than 50 nm; the approximate slip length is around the surface roughness and may be realistic. Unlike YVHH, only one parameter was fit, and this parameter has a realistic meaning. Furthermore, the apparent contact angle was never specified, but evolved naturally. This predicted slip length ratio ϵ is smaller than any currently existing DNS has achieved [141, 142].

The small remaining discrepancy between the experiment and the simulation in Fig. 6.9 seems to be due to too much energy loss at impact which prevents the maximum contact diameter from being achieved. There are a couple possible causes for this energy loss that have been tried and dismissed. The grid resolution is sufficiently fine for grid convergence (Fig. 6.11). The droplet start location does not matter (Fig. 6.12) because the air cushion underneath the droplet is not dissipating much energy and the drop velocity is too large (subsequently time to impact is too short) for gravity to

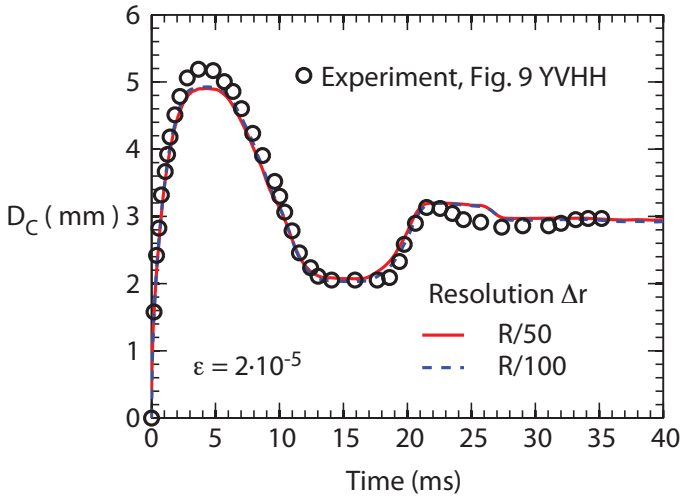

Figure 6.11: Drop contact diameter D_C in time t using the contact angle hysteresis angles $\theta_A = 107^o$, $\theta_R = 77^o$. The curves are different grid resolutions. The black dots are the experimental data of Fig. 9 in YVHH.

accelerate the drop much. If the diameter error tolerance ($\pm 2\%$) is applied to the initial velocity, the contact diameter does not vary much in time. That being said, an increase in the initial velocity by 10% is sufficient to achieve the correct maximum diameter (Fig. 6.13). Interestingly, while the curve with 10% more initial velocity (Fig. 6.13) has a different maximum contact diameter D_C, its behavior at later time mimics the other curves. This convergence suggests that the value of β, specifically for $\theta_{sa} = 107^o$, is not exactly right. There is too much viscous loss during the initial impact spreading. If the shear factors β_a and β_r are varied independently (two fitted parameters), better agreement can be found for the maximum contact diameter (Fig. 6.14). The receding shear factor in Fig. 6.14 is nearly the same as in Fig. 6.9 implying that the relationship for F may need refinement. Another option is the persistence of an air film during drop impact that lubricates the spreading water [78, 89, 90]. This film decreases the appropriate viscous shear factor F from the form proposed in Eq. 5.27 during this initial impact period. In addition to the different maximum contact diameters, the second peak in Fig. 6.14 is too flat; since flatness was shown to be controlled by the contact angle hysteresis in the average curvature, the simple model for contact angle hysteresis used here (Eq. 6.4) may need to be modified as well. Given the many assumptions in Table 6.2, some discrepancy is not surprising.

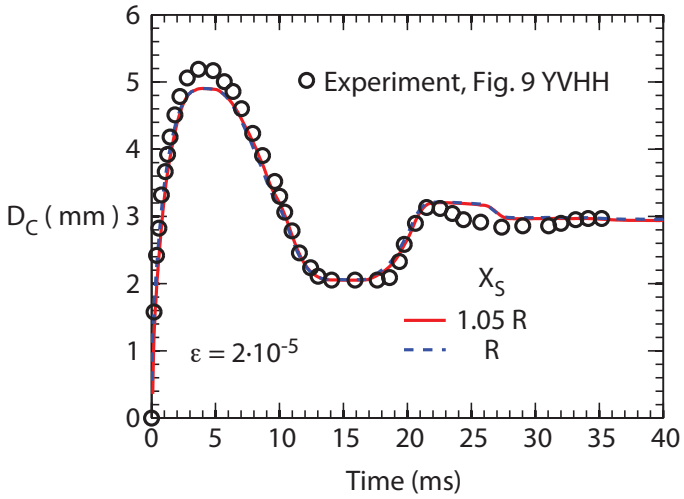

Figure 6.12: Drop contact diameter D_C in time t using the contact angle hysteresis angles $\theta_{sa} = 107^o$, $\theta_{sr} = 77^o$. The curves are drops started at different positions X_S. The black dots are the experimental data of Fig. 9 in YVHH.

6.5 Summary

The modeled source terms proposed in Chap. 5 and the relaxation equation reinitialization developed in Chap. 3 and 4 form an accurate numerical framework for the simulation of a drop impact experiment with a realistic slip length. Unlike prior work, only one free parameter, the slip length ratio ϵ, was approximated and it has a realistic value. The contact angle naturally evolved and automatically included high Reynolds number Re and capillary number Ca effects. The simulation was run on a much coarser mesh than would be required for the predicted slip length to be sufficiently resolved. Furthermore, this predicted slip length ratio was outside the range currently accessible by DNS. These results show that the methods proposed throughout this work are extremely promising.

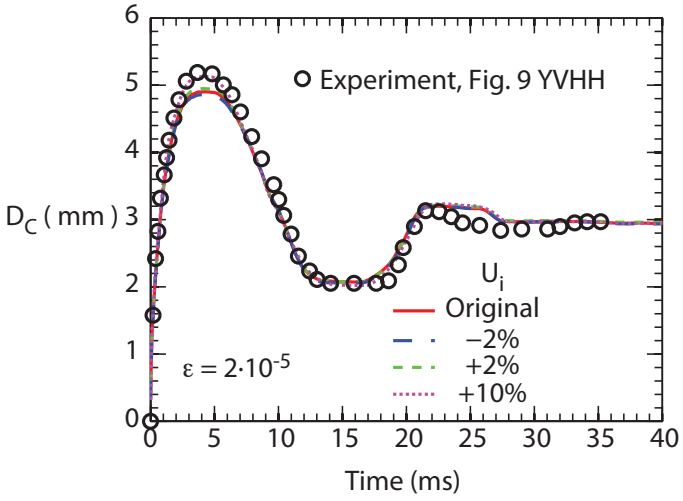

Figure 6.13: Drop contact diameter D_C in time t using the contact angle hysteresis angles $\theta_{sa} = 107^o$, $\theta_{sr} = 77^o$. The curves are drops with different initial velocities U_i. The black dots are the experimental data of Fig. 9 in YVHH.

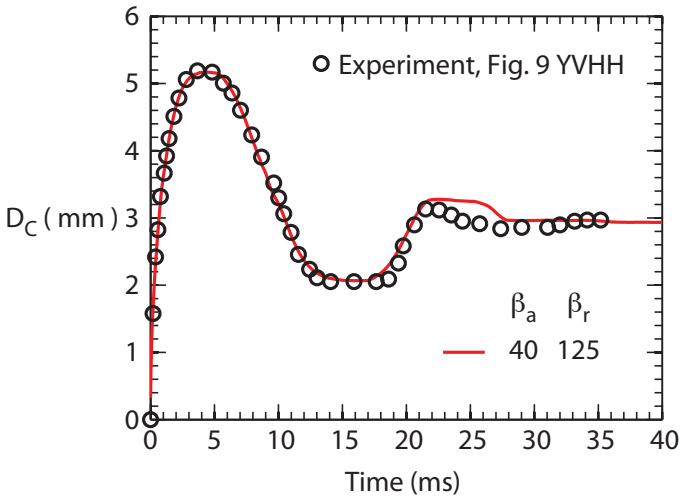

Figure 6.14: Drop contact diameter D_C in time t using the contact angle hysteresis angles $\theta_{sa} = 107^o$, $\theta_{sr} = 77^o$ in the average curvature. The shear factors β_a and β_r are varied independently for the advancing and receding contact lines. The black dots are the experimental data of Fig. 9 in YVHH.

Chapter 7

Conclusion

> *Now this is not the end. It is not even the beginning of the end. But it is, perhaps, the end of the beginning.*
>
> — Winston Churchill

7.1 Summary

There were two goals of this thesis outlined in Chap. 1. The first goal was to **create a numerical framework that allows the contact angle to evolve naturally with appropriate contact-line physics.** The second goal was to **develop equations and numerical methods such that contact-line simulations may be run on coarse computational meshes.**

A relaxation equation was proposed to modify the standard Hamilton-Jacobi reinitialization equation in the contact-line blind spot to reduce the numerical parasitic currents in Chap. 3. This equation held fixed the curvature at the contact line during reinitialization. While floating contact angles in prior methods added an unphysical driving force to circular arcs, this new algorithm did not introduce any numerical artificial forcing. This particular equation has slower convergence properties with small contact angles, but the concepts can be applied to other reintialization techniques such as the FMM. Chapter 4 created a blind spot algorithm for level-set extension velocities to maintain the correct angle in the relaxation equation. The stable construction of extension velocities required information to propagate along the wall into the blind spot. This propagation when

combined with the relaxation equation creates a new relaxation equation reinitialization that is a self-sufficient, complete algorithm. The relaxation equation reinitialization accomplished the first part of goal 1 by creating a numerical framework that did not introduce errors to a floating contact angle.

Chapter 5 identified the terms that need to be included in coarse simulations at contact lines and then approximated the forms of these terms from DNS. The first term, the average curvature $\bar{\kappa}$, was well approximated by a circular arc that varied smoothly from the apparent contact angle at the cell center to the static contact angle θ_S. The viscous shear VS was approximated by a power law in the slip length ratio ϵ. This chapter found the appropriate physical source terms that would allow the angle to evolve naturally (goal 1) and these source terms could be used on meshes much coarser than the slip length λ (goal 2).

All of the numerical methods were brought together in the coarse, efficient simulations in Chap. 6 for a droplet impacting a wall. The relaxation equation reinitialization allowed the angle to change according to inertial effects and the microscale physics of the source terms from Chap. 5. A simple contact angle hysteresis model was included; this model required the viscous approximations from Chap. 5 in order for the viscous resistance to vary with contact angle. Very favorable comparison to an experiment was shown. The predicted slip length was near the substrate roughness and, therefore, realistic. The approximate slip length ratio ϵ was smaller than any currently existing DNS; thus, these techniques have dramatically extended the parameter space that can be simulated.

7.2 Future directions

The next extensions of this work are classified into two categories: experimental comparisons and shear factor definition.

Experimental comparisons:

One of the fundamental difficulties with any contact-line problem is that the theories usually include at least one parameter that cannot be easily measured experimentally, i.e., the slip length λ. If other system simulations also yield realistic slip lengths, the current physical source terms used here may be representative of the contact-line physics. While such agreement is not proof of the average curvature and viscous shear validity, the framework as presented here would be very useful in industrial process optimization. Furthermore, additional experiments may suggest other physical source terms. These terms can be easily incorporated into the current framework.

Shear factor definition:

When the shear factor F was derived, only a small parameter space was explored and some weak dependencies (Ca, ξ) were not included. These parameters should be explored further. In addition, only three large values of the slip length ratio ϵ were used; smaller values should be included for testing purposes and to confirm the power-law behavior. There were two limitations to achieving smaller slip length ratios ϵ: the number of nodes necessary for sufficient grid resolution and the CFL restriction on surface tension (Eq. 2.20, 2.21). To reduce the number of grid nodes, either an AMR approach [141, 142] could be employed to locally refine the mesh at the interface or the boundary integral method could be used to solve the fluid mechanics [64, 111, 158]. The boundary integral method reduces the problem dimensionality. The time step restriction would be reduced if surface tension was formulated in a semi- or fully implicit manner; these approaches, however, are non-trivial because interface curvature introduces high-order, non-linear and non-local terms into the fluid dynamics. Hou et al. [66] developed an implicit time integration for 2D, irrotational fluids using the boundary integral method. Other authors have developed semi-implicit algorithms

[12, 123]. These methods are still an area of active research.

The work of this study is an important first step towards simulating these complicated geometries efficiently.

Appendix A

Matlab code to solve the non-linear, ordinary differential surface equation

The surface solution $\bar{h}(\bar{x})$ to Eq. 4.13 must be solved numerically. The Matlab commands to solve this equilibrium surface $\bar{h}(\bar{x})$ as a function of the Bond number Bo_W and surface constant $\bar{x}_0$ are replicated below. *relT* is a relative solver tolerance for the boundary value problem solver bvp5c.

```
function [x y area]=GravityBalanceST(Bo,x0,relT)

    % Inputs:
    % Bo = Bond number Bo_W.
    % x0 = location of zero curvature between 0 and 1, x̄_0.
    % relT = relative tolerance used in the differential equation solver.
    % Outputs:
    % x = x-coordinates for the equilibrium surface.
    % y = y-coordinates for the equilibrium surface.
    % area = area under the equilibrium surface.
    global a b
    a=Bo;
    b=x0;
```

```
close all
clc
npI = 10; % Number of points in the initial guess
y0 = 1; % Initial guess for y
% Solve the boundary problem
solinit=bvpinit(linspace(0,1,npI),[y0 0]);
options=bvpset('RelTol',relT,'AbsTol',1e-7);
sol=bvp5c(@twoode,@twobc,solinit,options);
sol.stats
% Evaluate the surface
x=linspace(0,1);
y=deval(sol,x);
area=trapz(x,y(1,:));
function dydx = twoode(x,y)
% System of ordinary differential equations
global a b
dydx=[y(2) -(1+y(2)^2)^1.5*a*(x-b)];


function res = twobc(ya,yb)
% Application of the boundary conditions
res=[ ya(1) yb(1)];
```

Appendix B

Simulations in chapter 5

#	Ca	θ_S	ϵ	Figures
1	0.0033	30^o	1/80	5.10a, 5.11
2	0.0033	50^o	1/80	5.10a, 5.11
3	0.0033	70^o	1/80	5.10a, 5.11
4	0.0033	90^o	1/80	5.10a, 5.11
5	0.0033	110^o	1/80	5.10a, 5.11
6	0.0033	130^o	1/80	5.10a, 5.11
7	0.0033	150^o	1/80	5.10a, 5.11
8	0.0033	30^o	1/40	5.10a, 5.11
9	0.0033	50^o	1/40	5.10a, 5.11
10	0.0033	70^o	1/40	5.10a, 5.11
11	0.0033	90^o	1/40	5.10a, 5.11
12	0.0033	110^o	1/40	5.10a, 5.11
13	0.0033	130^o	1/40	5.10a, 5.11
14	0.0033	150^o	1/40	5.10a, 5.11
15	0.0033	30^o	1/20	5.10a, 5.11
16	0.0033	50^o	1/20	5.10a, 5.11
17	0.0033	70^o	1/20	5.10a, 5.11
18	0.0033	90^o	1/20	5.10a, 5.11

19	0.0033	110^o	1/20	5.10a, 5.11
20	0.0033	130^o	1/20	5.10a, 5.11
21	0.0033	150^o	1/20	5.10a, 5.11
22	0.01	50^o	1/320	5.12
23	0.01	50^o	1/160	5.12
24	0.01	30^o	1/80	5.10b, 5.11, 5.13
25	0.01	50^o	1/80	5.8, 5.10b, 5.11, 5.12, 5.13
26	0.01	70^o	1/80	5.10b, 5.11, 5.13
27	0.01	90^o	1/80	5.10b, 5.11, 5.13
28	0.01	110^o	1/80	5.10b, 5.11, 5.13
29	0.01	130^o	1/80	5.10b, 5.11, 5.13
30	0.01	150^o	1/80	5.10b, 5.11, 5.13
31	0.01	30^o	1/40	5.10b, 5.11, 5.13
32	0.01	50^o	1/40	5.5, 5.9, 5.10b, 5.11, 5.12, 5.13
33	0.01	70^o	1/40	5.10b, 5.11, 5.13
34	0.01	90^o	1/40	5.6, 5.10b, 5.11, 5.13
35	0.01	110^o	1/40	5.10b, 5.11, 5.13
36	0.01	130^o	1/40	5.10b, 5.11, 5.13
37	0.01	150^o	1/40	5.10b, 5.11, 5.13
38	0.01	30^o	1/20	5.10b, 5.11, 5.13
39	0.01	50^o	1/20	5.10b, 5.11, 5.12, 5.13
40	0.01	70^o	1/20	5.10b, 5.11, 5.13
41	0.01	90^o	1/20	5.10b, 5.11, 5.13
42	0.01	110^o	1/20	5.10b, 5.11, 5.13
43	0.01	130^o	1/20	5.10b, 5.11, 5.13
44	0.01	150^o	1/20	5.10b, 5.11, 5.13

45	0.03	30^o	1/80	5.10c, 5.11
46	0.03	50^o	1/80	5.10c, 5.11
47	0.03	70^o	1/80	5.10c, 5.11
48	0.03	90^o	1/80	5.10c, 5.11
49	0.03	110^o	1/80	5.10c, 5.11
50	0.03	30^o	1/40	5.10c, 5.11
51	0.03	50^o	1/40	5.7, 5.10c, 5.11
52	0.03	70^o	1/40	5.10c, 5.11
53	0.03	90^o	1/40	5.10c, 5.11
54	0.03	110^o	1/40	5.10c, 5.11
55	0.03	30^o	1/20	5.10c, 5.11
56	0.03	50^o	1/20	5.10c, 5.11
57	0.03	70^o	1/20	5.10c, 5.11
58	0.03	90^o	1/20	5.10c, 5.11
59	0.03	110^o	1/20	5.10c, 5.11

Table B.1: Simulations in Chap. 5 with their capillary numbers Ca, static contact angles θ_S, slip length ratios ϵ, and respective figures.

Appendix C

Calculation of the shear factors F and G from DNS data

The values of F and G for a given combination of Ca, ϵ, and θ_S were evaluated for the DNS in Sec. 5.3 using the following procedure. A simulation's velocity and level set data sets were captured at increments of $\Delta t = 0.05$ for analysis. All numerical commands are for the Matlab programming environment.

Step 1:

The time when steady state is reached (t_{steady}) was approximated. For each data set in time, the interface shape was fit with a circular arc to determine the apparent contact angle θ_{app} at the wall. If C is a column vector of the interface points (Column 1: x-locations, Column 2: y-locations), the fit circle can be found using

```
a=[C(:,2) C(:,1) ones(size(C(:,2)))] \ [-(C(:,2).^ 2+C(:,1).^ 2)];
ycenter = -.5*a(1);
xcenter = -.5*a(2);
R = sqrt((a(1)^ 2+a(2)^ 2)/4-a(3));
```

where *xcenter* is the x-coordinate of the circle center, *ycenter* the y-coordinate, and R the circle radius. The apparent contact angle θ_{app} is approximated by

```
height=0.5+ycenter;
if xcenter>0
thetaapp=90-180/pi*asin(height/R);
else
thetaapp=90+180/pi*asin(height/R);
end
```

The first time at which the slope $\partial\theta_{app}/\partial t < 1$ degree / unit time and $\partial^2\theta_{app}/\partial t^2 < 1$ degree / unit time^2 was taken as steady state. The first condition implies the angle changes were small and the second that the angle is not oscillating much. An example of θ_{app} in time is shown in Fig. C.1 where the predicted steady-state time is $t_{steady} = 0.8$.

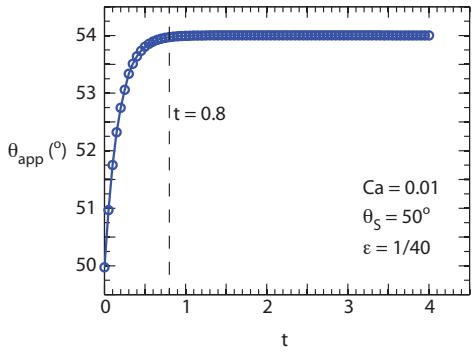

Figure C.1: Evolution of the apparent contact angle θ_{app} in time for $Ca = 0.01$, $\epsilon = 1/40$, and $\theta_S = 50^o$.

Step 2:

For each data set $t > t_{steady}$, u_{wall} as a function of $\bar{x} = (x - x_{contact})/\lambda$ is determined using the Navier-slip boundary condition. Using the velocity $U(x)$ stored immediately above the wall,

```
u_wall(x) = U(x)/(λ+Δy/2)*λ;
```

The extent of the curve is from $\bar{x} = -1/\epsilon$ to $1/\epsilon$; the ends points are very far from the contact line.

Step 3:

These curves of u_{wall} as a function of $\bar{x}$ were averaged in time using only values $t > t_{steady}$. A typical average consisted of more than 20 curves.

Step 4:

The bulk flow u_B was subtracted off by removing the amount of velocity far away at the edges of this truncated domain.

$$u_{wall2}(\bar{x}) = u_{wall}(\bar{x}) - u_B$$

Step 5:

The new values of u_{wall2} was renormalized to have a magnitude of 1 at the contact line.

$$u_{wall3} = u_{wall2}/max(u_{wall2})$$

Step 6:

F and G were found by numerical, trapezoidal integration of u_{wall3}. The numerical integrator trapz was used.

Bibliography

[1] D. Adalsteinsson and J. A. Sethian. A fast level set method for propagating interfaces. *J. Comput. Phys.*, 118:269–277, 1995.

[2] D. Adalsteinsson and J. A. Sethian. The fast construction of extension velocities in level set methods. *J. Comput. Phys.*, 148:2–22, 1999.

[3] S. Afkhami and M. Bussmann. Height functions for applying contact angles to 2D VOF simulations. *Int. J. Numer. Meth. Fluids*, 57:453–472, 2008.

[4] S. Afkhami, S. Zaleski, and M. Bussmann. A mesh-dependent model for applying dynamic contact angles to VOF simulations. *J. Comput. Phys.*, 228:5370–5389, 2009.

[5] International Energy Agency. World energy outlook 2013 factsheet. Technical report, International Energy Agency, 2013.

[6] V. S. Ajaev. *Interfacial Fluid Mechanics*. Springer Science, first edition, 2012.

[7] A. M. Barajas and R. L. Panton. The effects of contact angle on two-phase flow in capillary tubes. *Int. J. Multiphase Flow*, 19:337–346, 1993.

[8] W. Barthlott and C. Neinhuis. Purity of the sacred lotus, or escape from contamination in biological surfaces. *Planta*, 202:1–8, 1997.

[9] S. Basu, K. Nandakumar, and J. H. Masliyah. A study of oil displacement on model surfaces. *J. Colloid Inter. Sci.*, 182:82–94, 1996.

[10] G. K. Batchelor. *An Introduction to Fluid Dynamics*. Cambridge University Press, eleventh edition, 2009.

[11] I. S. Bayer and C. M. Megaridis. Contact angle dynamics in droplets impacting on flat surfaces with different wetting characteristics. *J. Fluid Mech.*, 558:415–449, 2006.

[12] J. T. Beale. Partially implicit motion of a sharp interface in Navier—Stokes flow. *J. Comput. Phys.*, 231:6159–6172, 2012.

[13] J. C. Berg. *Wettability*. Taylor & Francis Group, first edition, 1993.

[14] T. D. Blake. The physics of moving wetting lines. *J. Colloid Interface Sci.*, 299:1–13, 2006.

[15] T. D. Blake, M. Bracke, and Y. D. Shikhmurzaev. Experimental evidence of nonlocal hydrodynamic influence on the dynamic contact angle. *Phys. Fluids*, 11:1995–2007, 1999.

[16] T. D. Blake and J. M. Haynes. Kinetics of liquid/liquid displacement. *J. Colloid Inter. Sci.*, 30:421–423, 1969.

[17] R. Blossey. Self-cleaning surfaces - virtual realities. *Nature Mat.*, 2:301–306, 2003.

[18] D. Bonn, J. Eggers, J. Indekeu, J. Meunier, and E. Rolley. Wetting and spreading. *Rev. Mod. Phys.*, 81:739–805, 2009.

[19] J. U. Brackbill, D. B. Kothe, and C. Zemach. A continuum method for modeling surface tension. *J. Comput. Phys.*, 100:335–354, 1992.

[20] F. Brochard-Wyart and P. G. de Gennes. Dynamics of partial wetting. *Adv. Colloid Inter. Sci.*, 39:1–11, 1992.

[21] R. Burley and B. S. Kennedy. An experimental study of air entrainment at a solid/liquid/gas interface. *Chem. Eng. Sci.*, 31:901–911, 1976.

[22] A. Carlson, G. Bellani, and G. Amberg. Universality in dynamic wetting dominated by contact-line friction. *Phys. Rev. E*, 85:045302, 2012.

[23] A. B. D. Cassie and S. Baxter. Wettability of porous surfaces. *Trans. Faraday Soc.*, 40:546–551, 1944.

[24] Y. C. Chang, T. Y. Hou, B. Merriman, and S. J. Osher. A level set formulation of Eulerian interface capturing methods for incompressible fluid flows. *J. Comput. Phys.*, 124:449–464, 1996.

[25] H. Choi and P. Moin. Effects of the computational time step on numerical solutions of turbulent flow. *J. Comput. Phys.*, 113:1–4, 1994.

[26] D. L. Chopp. Computing minimal surfaces via level set curvature flow. *J. Comput. Phys.*, 106:77–91, 1993.

[27] A. Clarke and E. Stattersfield. Direct evidence supporting nonlocal hydrodynamic influence on the dynamic contact angle. *Phys. Fluids*, 18:048106, 2006.

[28] R. G. Cox. The dynamics of the spreading of liquids on a solid surface. Part 1. Viscous flow. *J. Fluid Mech.*, 168:169–194, 1986.

[29] P. G. de Gennes. Wetting: statics and dynamics. *Rev. Mod. Phys.*, 57:827–863, 1985.

[30] P. G. de Gennes, F. Brochard-Wyart, and D. Quéré. *Capillarity and Wetting Phenomenon.* Springer Science, first edition, 2004.

[31] D. Deganello, T. N. Croft, A. J. Williams, A. S. Lubansky, D. T. Gethin, and T. C. Claypole. Numerical simulation of dynamic contact angle using a force based formulation. *J. Nonnewton. Fluid Mech.*, 166:900–907, 2011.

[32] G. Della Rocca and G. Blanquart. Level set reinitialization at a contact line. *J. Comput. Phys.*, 265:34–49, 2014.

[33] O. Desjardins, G. Blanquart, G. Balarac, and H. Pitsch. High order conservative finite difference scheme for variable density low Mach number turbulent flows. *J. Comput. Phys.*, 227:7125–7159, 2008.

[34] O. Desjardins, V. Moureau, and H. Pitsch. An accurate conservative level set / ghost fluid method for simulating turbulent atomization. *J. Comput. Phys.*, 227:8395–8416, 2008.

[35] H. Ding, E. Q. Li, F. H. Zhang, Y. Sui, P. D. M. Spelt, and S. T. Thoroddsen. Propagation of capillary waves and ejection of small droplets in rapid droplet spreading. *J. Fluid Mech.*, 697:92–114, 2012.

[36] H. Ding and P. D. M. Sp2003Blossey:NatMatelt. Inertial effects in droplet spreading: a comparison between diffuse-interface and level-set simulations. *J. Fluid Mech.*, 576:287–296, 2007.

[37] J. B. Dupont and D. Legendre. Numerical simulation of static and sliding drop with contact angle hysteresis. *J. Comput. Phys.*, 229:2453–2478, 2010.

[38] E. B. Dussan V. The moving contact line: the slip boundary condition. *J. Fluid Mech.*, 77:665–684, 1976.

[39] J. Eggers and H. A. Stone. Characteristic lengths at moving contact lines for a perfectly wetting fluid: the influence of speed on dynamic contact angle. *J. Fluid Mech.*, 505:309–321, 2004.

[40] D. Enright, R. Fedkiw, J. Ferziger, and I. Mitchell. A hybrid particle level set method for improved interface capturing. *J. Comput. Phys.*, 183:83–116, 2002.

[41] R. E. Ewing and H. Wang. A summary of numerical methods for time-dependent advection-dominated partial differential equations. *J. Comput. Appl. Math.*, 128:423–445, 2001.

[42] M. Falcone and R. Ferretti. Convergence analysis for a class of high-order semi-Lagrangian advection schemes. *SIAM J. Numer. Anal.*, 35:909–940, 1998.

[43] R. Fedkiw, T. Aslam, B. Merriman, and S. Osher. A non-oscillatory Eulerian approach to interfaces in multimaterial flows (the ghost fluid method). *J. Comput. Phys.*, 152:457–492, 1999.

[44] M. Fermigier and P. Jenffer. An experimental investigation of the dynamic contact angle in liquid-liquid systems. *J. Colloid Inter. Sci.*, 146:226–241, 1991.

[45] J. H. Ferziger and M. Perić. *Computational Methods for Fluid Dynamics*. Springer Science, third edition, 2002.

[46] D. E. Finlow, P. R. Kota, and A. Bose. Investigation of wetting hydrodynamics using numerical simulations. *Phys. Fluids*, 8:302–309, 1996.

[47] R. T. Foister. The kinetics of displacement wetting in liquid / liquid / solid systems. *J. Colloid Inter. Sci.*, 136:266–282, 1990.

[48] M. M. Francois, S. J. Cummins, E. D. Dendy, D. B. Kothe, J. M. Sicilian, and M. W. Williams. A balanced-force algorithm for continuous and sharp interfacial surface tension models with a volume tracking framework. *J. Comput. Phys.*, 213:141–173, 2006.

[49] J. Fukai, Y. Shiiba, T. Yamamoto, O. Miyatake, D. Poulikakos, C. M. Megaridis, and Z. Zhao. Wetting effects on the spreading of a liquid droplet colliding with a flat surface: experiment and modeling. *Phys. Fluids*, 7:236–247, 1995.

[50] A. L. Garcia, J. B. Bell, W. Y. Crutchfield, and B. J. Alder. Adaptive mesh and algorithm refinement using direct simulation Monte Carlo. *J. Comput. Phys.*, 154:134–155, 1999.

[51] T. C. Germann and K. Kadau. Trillion-atom molecular dynamics becomes a reality. *Int. J. Mod. Phys. C*, 19:1315–1319, 2008.

[52] S. Gross and A. Reusken. Numerical simulation of continuum models for fluid-fluid interface dynamics. *Eur. Phys. J. Special Topics*, 222:211–239, 2013.

[53] N. G. Hadjiconstantinou. Combining atomistic and continuum simulations of contact-line motion. *Phys. Rev. E*, 59:2475–2478, 1999.

[54] N. G. Hadjiconstantinou. Hybrid atomistic-continuum formulations and the moving contact-line problem. *J. Comput. Phys.*, 154:245–265, 1999.

[55] W. J. Hamilton and M. K. Seely. Fog basking by the Namib Desert beetle, Onymacris unguicularis. *Nature*, 262:284–285, 1976.

[56] R. W. Hamming. *Numerical Methods for Scientists and Engineers*. Dover Publications, 1973.

[57] F. H. Harlow and J. E. Welch. Numerical calculation of time-dependent viscous incompressible flow of fluid with free surface. *Phys. Fluids*, 8:2182–2189, 1965.

[58] D. Hartmann, M. Meinke, and W. Schröer. Differential equation based constrained reinitialization for level set methods. *J. Comput. Phys.*, 227:6821–6845, 2008.

[59] D. Hartmann, M. Meinke, and W. Schröer. The constrained reinitialization equation for level set methods. *J. Comput. Phys.*, 229:1514–1535, 2010.

[60] V. E. Hensen and U. M. Yang. Boomeramg: A parallel algebraic multigrid solver and preconditioner. *Appl. Numer. Math.*, 41:155–177, 2002.

[61] S. E. Hieber and P. Koumoutsakos. A Lagrangian particle level set method. *J. Comput. Phys.*, 210:342–367, 2005.

[62] C. W. Hirt and B. D. Nichols. Volume of fluid (VOF) method for dynamics of free boundaries. *J. Comput. Phys.*, 39:201–225, 1981.

[63] L. M. Hocking and A. D. Rivers. The spreading of a drop by capillary action. *J. Fluid Mech.*, 121:425–442, 1982.

[64] N. Hoda and S. Kumar. Boundary integral simulations of liquid emptying from a model gravure cell. *Phys. Fluids*, 20:092106, 2008.

[65] R. L. Hoffman. A study of the advancing interface I. Interface shape in liquid-gas systems. *J. Colloid Inter. Sci.*, 50:228–241, 1975.

[66] T. Y. Hou, J. S. Lowengrub, and M. J. Shelley. Removing the stiffness from interfacial flows with surface tension. *J. Comput. Phys.*, 114:312–338, 1994.

[67] C. Huh and L. E. Scriven. Hydrodynamic model of steady movement of a solid / liquid / fluid contact line. *J. Colloid Inter. Sci.*, 35:85–101, 1971.

[68] M. Iguchi and Y. Terauchi. Boundaries among bubbly and slug flow regimes in air-water two-phase flows in vertical pipes of poor wettability. *Int. J. Multiphase Flow*, 27:729–735, 2001.

[69] D. Jacqmin. Calculation of two-phase Navier—Stokes flows using phase-field modeling. *J. Comput. Phys.*, 155:96–127, 1999.

[70] D. Jacqmin. Contact-line dynamics of a diffuse fluid interface. *J. Fluid Mech.*, 402:57–88, 2000.

[71] G. Jiang and D. Peng. Weighted ENO schemes for Hamilton—Jacobi equations. *SIAM J. Sci. Comput.*, 21:2126–2143, 1997.

[72] K. Kadau, J. L. Barber, T. C. Germann, B. L. Holian, and B. J. Alder. Atomistic methods in fluid simulation. *Phil. Trans. R. Soc. A*, 368:1547–1560, 2010.

[73] M. Kang, R. P. Fedkiw, and X. Liu. A boundary condition capturing method for multiphase incompressible flow. *J. Sci. Comput.*, 15:323–360, 2000.

[74] K. H. Karlsen, K. A. Lie, and N. H. Risebro. A fast marching method for reservoir simulation. *Comput. Geo.*, 4:185–206, 2000.

[75] M. N. Kashid and L. Kiwi-Minsker. Microstructured reactors for multiphase reactions: state of the art. *Ind. Eng. Chem. Res.*, 48:6465–6485, 2009.

[76] H. Kim, S. Jeon, M. Song, and K. Kim. Numerical simulations of water droplet dynamics in hydrogen fuel cell gas channel. *J. Power Sources*, 246:679–695, 2014.

[77] E. Kirkinis and S. H. Davis. Hydrodynamic theory of liquid slippage on a solid substrate near a moving contact line. *Phys. Rev. Lett.*, 110:234503, 2013.

[78] J. M. Kolinski, S. M. Rubinstein, S. Mandre, M. P. Brenner, D. A. Weitz, and L. Mahadevan. Skating on a film of air: Drops impacting on a surface. *Phys. Rev. Lett.*, 108:074503, 2012.

[79] J. Koplik, J. R. Banavar, and J. F. Willemsen. Molecular dynamics of Poiseuille flow and moving contact lines. *Phys. Rev. Lett.*, 60:1282–1285, 1988.

[80] Lawrence Livermore National Laboratory. HYPRE. Available at http://computation.llnl.gov/casc/hypre/software.html.

[81] B. Lafaurie, C. Nardone, R. Scardovelli, S. Zaleski, and G. Zanetti. Modelling merging and fragmentation in multiphase flows with SURFER*. *J. Comput. Phys.*, 113:134–147, 1994.

[82] L. D. Landau and E. M. Lifshitz. *Fluid Mechanics*. Pergamon Press, sixth edition, 1982.

[83] E. Lauga and H. A. Stone. Effective slip in pressure-driven stokes flow. *J. Fluid Mech.*, 489:55–77, 2003.

[84] C. Y. Lee and S. Y. Lee. Pressure drop of two-phase dry-plug flow in round mini-channels: effect of moving contact line. *Exp. Therm. Fluid Sci.*, 34:1–9, 2010.

[85] J. E. Lennard-Jones. On the determination of molecular fields. *Proc. R. Soc. Lond. A*, 106:463–477, 1924.

[86] B. P. Leonard. A stable and accurate convective modelling procedure based on quadratic upstream interpolation. *Comput. Meth. Appl. Mech. Eng.*, 19:59–98, 1979.

[87] H. Liu, S. Krishnan, S. Marella, and H. S. Udaykumar. Sharp interface Cartesian grid method II: A technique for simulating droplet interactions with surfaces of arbitrary shape. *J. Comput. Phys.*, 210:32–54, 2005.

[88] J. Lowengrub and L. Truskinovsky. Quasi-incompressible Cahn-Hilliard fluids and topological transitions. *Proc. R. Soc. Lond. A*, 454:2617–2654, 1998.

[89] S. Mandre and M. P. Brenner. The mechanism of a splash on a dry solid surface. *J. Fluid Mech.*, 690:148–172, 2012.

[90] S. Mandre, M. Mani, and M. P. Brenner. Precursors to splashing of liquid drops on a solid surface. *Phys. Rev. Lett.*, 102:134502, 2009.

[91] E. Marchandise, P. Geuzaine, N. Chevaugeon, and J. F. Remacle. A stabilized finite element method using a discontinuous level set approach for the computation of bubble dynamics. *J. Comput. Phys.*, 225:949–974, 2007.

[92] J. A. Marsh, S. Garoff, and E. B. Dussan V. Dynamic contact angles and hydrodynamics near a moving contact line. *Phys. Rev. Lett.*, 70:2778–2781, 1993.

[93] A. McDonald. Accuracy of multiply-upstream, semi-Lagrangian advective schemes. *Mon. Wea. Rev.*, 112:1267–1275, 1984.

[94] T. Ménard, S. Tanguy, and A. Berlemont. Coupling level set / VOF / ghost fluid methods: Validation and application to 3D simulation of the primary break-up of a liquid jet. *Int. J. Multiphase Flow*, 33:510–524, 2007.

[95] A. J. B. Milne and A. Amirfazli. Drop shedding by shear flow for hydrophilic to superhydrophobic surfaces. *Langmuir*, 25:14155–14164, 2009.

[96] J. A. Moriarty and L. W. Schwartz. Effective slip in numerical calculations of moving-contact-line problems. *J. Eng. Math.*, 26:81–86, 1992.

[97] W. Mulder, S. Osher, and J. A. Sethian. Computing interface motion in compressible gas dynamics. *J. Comput. Phys.*, 100:209–228, 1992.

[98] C. L. Navier. Mémoire sur les lois du mouvement des fluides. *Mem. Acad. Sci. Inst. Fr.*, 6:389–440, 1823.

[99] R. Nourgaliev, S. Kadioglu, and V. Mousseau. Marker redistancing / level set method for high-fidelity implicit interface tracking. *SIAM J. Sci. Comput.*, 32:320–348, 2010.

[100] E. Olsson and G. Kreiss. A conservative level set method for two phase flow. *J. Comput. Phys.*, 210:225–246, 2005.

[101] M. E. Orme, C. Z. Huang, and J. Courter. Precision droplet-based manufacturing and material synthesis: Fluid dynamics and thermal control issues. *Atomization and Sprays*, 6:305–329, 1996.

[102] S. Osher and R. Fedkiw. *Level Set Methods and Dynamic Implicit Surfaces*. Springer Science, first edition, 2003.

[103] S. Osher and J. A. Sethian. Fronts propagating with curvature-dependent speed: Algorithms based on Hamilton—Jacobi formulations. *J. Comput. Phys.*, 79:12–49, 1988.

[104] A. Otten and S. Herminghaus. How plants keep dry: a physicist's point of view. *Langmuir*, 20:2405–2408, 2004.

[105] J. K. Park and K. H. Kang. Numerical analysis of moving contact line with contact angle hysteresis using feedback deceleration technique. *Phys. Fluids*, 24:042105, 2012.

[106] A. R. Parker and C. R. Lawrence. Water capture by a desert beetle. *Nature*, 414:33–34, 2001.

[107] P. G. Petrov and J. G. Petrov. A combined-molecular hydrodynamic approach to wetting kinetics. *Langmuir*, 8:1762–1767, 1992.

[108] C. D. Pierce and P. Moin. Progress-variable approach for large eddy simulation of turbulent combustion. Technical Report Rep. TF80, Flow Physics and Computation Division, Dept. Mech. Eng., Stanford Univ., 2001.

[109] L. M. Pismen and Y. Pomeau. Disjoining potential and spreading of thin liquid layers in the diffuse-interface model coupled to hydrodynamics. *Phys. Rev. E*, 62:2480–2492, 2000.

[110] S. Popinet and S. Zaleski. A front-tracking algorithm for accurate representation of surface tension. *Int. J. Numer. Meth. Fluids*, 30:775–793, 1999.

[111] C. Pozrikidis. *Boundary Integral and Singularity Methods for Linearized Viscous Flow*. Cambridge University Press, first edition, 1992.

[112] T. Qian, X. P. Wang, and P. Sheng. Power-law slip profile of the moving contact line in two-phase immiscible flows. *Phys. Rev. Lett.*, 93:094501, 2004.

[113] D. Quéré. Rough ideas on wetting. *Physica A*, 313:32–46, 2002.

[114] J. Ralston, M. Popescu, and R. Sedev. Dynamics of wetting from an experimental point of view. *Annu. Rev. Mater. Res.*, 38:23–43, 2008.

[115] W. Ren and W. E. Boundary conditions for the moving contact line problem. *Phys. Fluids*, 19:022101, 2007.

[116] M. Renardy, Y. Renardy, and J. Li. Numerical simulation of moving contact line problems using a volume-of-fluid method. *J. Comput. Phys.*, 171:243–263, 2001.

[117] G. Russo and P. Smereka. A remark on computing distance functions. *J. Comput. Phys.*, 163:51–67, 2000.

[118] P. Sagaut. *Large Eddy Simulation for Incompressible Flows.* Springer Science, third edition, 2006.

[119] Y. Sato and G. Ničeno. A new contact line treatment for a conservative level set method. *J. Comput. Phys.*, 231:3887–3895, 2012.

[120] N. Savva and S. Kalliadasis. Dynamics of moving contact lines: A comparison between slip and precursor film models. *EPL*, 94:64004, 2011.

[121] R. Scardovelli and S. Zaleski. Direct numerical simulation of free-surface and interfacial flow. *Ann. Rev. Fluid Mech.*, 31:567–603, 1999.

[122] R. Scardovelli and S. Zaleski. Analytical relations connecting linear interfaces and volume fractions in rectangular grids. *J. Comput. Phys.*, 164:228–237, 2000.

[123] C. Schroeder, W. Zheng, and R. Fedkiw. Semi-implicit surface tension formulation with a Lagrangian surface mesh on an Eulerian simulation grid. *J. Comput. Phys.*, 231:2092–2115, 2012.

[124] J. A. Sethian. Fast marching methods. *SIAM Review*, 41:199–235, 1999.

[125] J. A. Sethian. *Level Set Methods and Fast Marching Methods: Evolving Interfaces in Computational Geometry, Fluid Mechanics, Computer Vision, and Materials Science.* Cambridge University Press, ninth edition, 2008.

[126] M. E. R. Shanahan. Condensation transport in dynamic wetting. *Langmuir*, 17:3997–4002, 2001.

[127] M. E. R. Shanahan. Spreading of water: condensation effects. *Langmuir*, 17:8229–8235, 2001.

[128] P. Sheng and M. Zhao. Immiscible-fluid displacement: Contact-line dynamics and the velocity-dependent capillary pressure. *Phys. Rev. A*, 45:5694–5708, 1992.

[129] Y. D. Shikhmurzaev. The moving contact line on a smooth solid surface. *Int. J. Multiphase Flow*, 19:589–610, 1993.

[130] Y. D. Shikhmurzaev. Moving contact lines in liquid/liquid/solid systems. *J. Fluid Mech.*, 334:211–249, 1997.

[131] Y. D. Shikhmurzaev. *Capillary Flows with Forming Interfaces.* Chapman & Hall / CRC, first edition, 2008.

[132] Y. D. Shikhmurzaev. Some dry facts about dynamic wetting. *Euro. Phys. J. Special Topics*, 197:47–60, 2011.

[133] S. Shin and D. Juric. A hybrid interface method for three-dimensional multiphase flows based on front tracking and level set techniques. *Int. J. Numer. Meth. Fluids*, 60:753–778, 2009.

[134] D. N. Sibley, N. Savva, and S. Kalliadasis. Slip or not slip? A methodical examination of the interface formation model using two-dimensional droplet spreading on a horizontal planar substrate as a prototype system. *Phys. Fluids*, 24:082105, 2012.

[135] J. H. Snoeijer and B. Andreotti. Moving contact lines: Scales, regimes, and dynamical transitions. *Ann. Rev. Fluid Mech.*, 45:269–292, 2013.

[136] Y. Son, C. Kim, D. H. Yang, and D. J. Ahn. Spreading of an inkjet droplet on a solid surface with a controlled contact angle at low Weber and Reynolds numbers. *Langmuir*, 24:2900–2907, 2008.

[137] P. D. M. Spelt. A level-set approach for simulations of flows with multiple moving contact lines with hysteresis. *J. Comput. Phys.*, 207:389–404, 2005.

[138] J. Stoer and R. Bulirsch. *Introduction to Numerical Analysis*. Springer Science, third edition, 2002.

[139] H. A. Stone, A. D. Stroock, and A. Ajdari. Engineering flows in small devices: Microfluidics toward a lab-on-a-chip. *Annu. Rev. Fluid Mech.*, 36:381–411, 2004.

[140] Y. Sui, H. Ding, and P. D. M. Spelt. Numerical simulations of flows with moving contact lines. *Annu. Rev. Fluid Mech.*, 46:97–119, 2014.

[141] Y. Sui and P. D. M. Spelt. An efficient computational model for macroscale simulations of moving contact lines. *J. Comput. Phys.*, 242:37–52, 2013.

[142] Y. Sui and P. D. M. Spelt. Validation and modification of asymptotic analysis of slow and rapid droplet spreading by numerical simulation. *J. Fluid Mech.*, 715:283–313, 2013.

[143] M. Sussman. An adaptive mesh algorithm for free surface flows in general geometries. In A. Vande Wouwer, Ph. Saucez, and W. E. Schiesser, editors, *Adaptive Method of Lines*, chapter 7. Chapman & Hall, 2001.

[144] M. Sussman and D. Dommermuth. The numerical simulation of ship waves using Cartesian grid methods. In *Proceedings of the 23rd Symposium on Naval Hydrodynamics*. 2000.

[145] M. Sussman, P. Smereka, and S. Osher. A level set approach for computing solutions to incompressible two-phase flow. *J. Comput. Phys.*, 114:146–159, 1994.

[146] M. Sussman, K. M. Smith, M. Y. Hussaini, M. Ohta, and R. Zhi-Wei. A sharp interface method for incompressible two-phase flows. *J. Comput. Phys.*, 221:469–505, 2007.

[147] M. Sussman and S. Uto. A computational study of the spreading of oil underneath a sheet of ice. *CAM Report 98–32*, 1998.

[148] J. C. Tannehill, D. A. Anderson, and R. H. Pletcher. *Computational Fluid Mechanics and Heat Transfer*. Taylor & Francis, second edition, 1997.

[149] L. H. Tanner. The spreading of silicon oil drops on horizontal surfaces. *J. Phys. D: Appl. Phys.*, 12:1473–1484, 1979.

[150] A. Theodorakakos, T. Ous, M. Gavaises, J. M. Nouri, N. Nikolopoulos, and H. Yanagihara. Dynamics of water droplets detached from porous surfaces of relevance to PEM fuel cells. *J. Colloid Inter. Sci.*, 300:673–687, 2006.

[151] P. A. Thompson and M. O. Robbins. Simulations of contact-line motion: Slip and the dynamic contact angle. *Phys. Rev. Lett.*, 63:766–769, 1989.

[152] P. A. Thompson and S. M. Troian. A general boundary condition for liquid flow at solid surfaces. *Nature*, 389:360–362, 1997.

[153] G. Tryggvason, R. Scardovelli, and S. Zaleski. *Direct Numerical Simulations of Gas-Liquid Multiphase Flows*. Cambridge University Press, first edition, 2011.

[154] S. O. Unverdi and G. Tryggvason. A front-tracking method for viscous, incompressible, multi-fluid flows. *J. Comput. Phys.*, 100:25–37, 1992.

[155] D. Vadillo. *Characterization of hydrodynamics phenomena during drop impact onto different types of substrates*. PhD thesis, University Joseph Fourier, 2006.

[156] D. C. Vadillo, A. Soucemarianadin, C. Delattre, and D. C. D. Roux. Dynamic contact angle effects onto the maximum drop impact spreading on solid surfaces. *Phys. Fluids*, 21:122002, 2009.

[157] H. A. van der Vorst. *Iterative Krylov Methods for Large Linear Systems*. Cambridge University Press, 2003.

[158] H. B. van Lengerich and P. H. Steen. Energy dissipation and the contact-line region of a spreading bridge. *J. Fluid Mech.*, 703:111–114, 2012.

[159] S. Verma, Y. Xuan, and G. Blanquart. An improved bounded semi-Lagrangian scheme for turbulent transport of passive scalars. *J. Comput. Phys.*, 2014.

[160] C. Walker and B. Müller. Contact line treatment with sharp interface method. *Computers and Fluids*, 84:255–261, 2013.

[161] M. M. Weislogel, J. A. Baker, and R. M. Jenson. Quasi-steady capillarity-driven flows in slender containers with interior edges. *J. Fluid Mech.*, 685:271–305, 2011.

[162] M. Wörner. Numerical modeling of multiphase flows in microfluidics and micro process engineering: A review of methods and applications. *Microfluid Nanofluidics*, 12:841–886, 2012.

[163] D. Xiu and G. E. Karniadakis. A semi-Lagrangian high-order method for Navier—Stokes equations. *J. Comput. Phys.*, 172:658–684, 2001.

[164] G. Yarnold and B. Mason. A theory of the angle of contact. *Proc. Phys. Soc.*, 62:121–125, 1949.

[165] T. Yi and H. Wong. Theory of slope-dependent disjoining pressure with application to Lennard—Jones liquid films. *J. Colloid Inter. Sci.*, 313:579–591, 2007.

[166] K. Yokoi, D. Vadillo, J. Hinch, and I. Hutchings. Numerical studies of the influence of the dynamic contact angle on a droplet impacting on a dry surface. *Phys. Fluids*, 21, 2009.

[167] T. Young. An essay on the cohesion of fluids. *Philos. Trans. R. Soc. London*, 95:65–87, 1805.

[168] J. Yu, S. Sakai, and J. A. Sethian. A coupled level set projection method applied to ink jet simulation. *Interfaces and Free Boundaries*, 5:459–482, 2003.

[169] P. Yue, J. J. Feng, C. Liu, and J. Shen. A diffuse-interface method for simulating two-phase flows of complex fluids. *J. Fluid Mech.*, 515:293–317, 2004.

[170] S. Zahedi, K. Gustavsson, and G. Kreiss. A conservative level set method for contact line dynamics. *J. Comput. Phys.*, 228:6361–6375, 2009.

[171] H. Zhao, T. Chan, B. Merriman, and S. Osher. A variational level set approach to multiphase motion. *J. Comput. Phys.*, 127:179–195, 1996.

Index